Ph.D. Dissertation

International Doctoral School in Information

and Communication Technology

DISI - University of Trento

Sparse Processing Methodologies Based on Compressive Sensing for Directions-of-Arrival Estimation

Mohammad Abdul Hannan

Advisor:
Paolo Rocca, Associate Professor
University of Trento

October 2020

Acknowledgement

First and foremost, I would like to thank ***Almighty Allah*** *for giving me strength, knowledge and the opportunity to undertake this research study and to complete it satisfactorily.*

It is with immense gratitude that I acknowledge the support and the help recieved from the ***ELEDIA Research Center*** *which provided me with a learning-friendly environment, training me with the advanced tools, and making sure to expand my research skills for both industry and accademia.*

I am indebted to my honourable Professor ***Paolo Rocca****, associate professor at the University of Trento, for mentoring me at his best. He helped me to choose the research field and guided me accordingly with the knowledge and ideas.*

I am overwhelmed to acknowledge my **colleagues** *in ELEDIA Research Center for the their amiable personalities. They have always been a source of inspiration, showing me immense amount of kindness.*

Thanks to all of my well wishers, to whom I am very grateful for making my life happier here in Trento. Thank you Tasnim Rahman ***Niti*** *(my very personal chef) for sharing and caring. Thank you Shamin Rahman (the Philosopher) for sharing your knowledge from eastern to western philosophy and for the dinners(sss). Thank you Ali Hasan (human google) for being the most informative person I have ever met.*

I am grateful to my family, especially my mother, ***Saleha Begum****, who has been my support.*

Finally, I wish to dedicate this thesis to my late father ***Mohammad Jalal Ahmad****, a man with a golden heart, who dedicated most of his life for the well being of our village, donating most of his wealth to the schools, mosques, and madrashas.*

Abstract

In this dissertation, sparse processing of signals for directions-of-arrival ($DoAs$) estimation is addressed in the framework of Compressive Sensing (CS). In particular, $DoAs$ estimation problem for different types of sources, systems, and applications are formulated in the CS paradigm. In addition, the fundamental conditions related to the "Sparsity" and "Linearity" are carefully exploited in order to apply confidently the $CS-$based methodologies. Moreover, innovative strategies for various systems and applications are developed, validated numerically, and analyzed extensively for different scenarios including signal to noise ratio (SNR), mutual coupling, and polarization loss. The more realistic data from electromagnetic (EM) simulators are often considered for various analysis to validate the potentialities of the proposed approaches. The performances of the proposed estimators are analyzed in terms of standard root-mean-square error ($RMSE$) with respect to different degrees-of-freedom ($DoFs$) of $DoAs$ estimation problem including number of elements, number of signals, and signal properties. The outcomes reported in this thesis suggest that the proposed estimators are computationally efficient (i.e., appropriate for real time estimations), robust (i.e., appropriate for different heterogeneous scenarios), and versatile (i.e., easily adaptable for different systems).

Keywords
Direction of arrival (DoA) estimation, real-time DoA estimation, narrowband DoA, wideband DoA, closely spaced DoA, widely spaced DoA, clutter estimation, linear array, planar array, clustered arrays, sub-array, Compressive Sensing (CS), Bayesian Compressive Sensing (BCS), single-task BCS (ST-BCS), iterative multi-scaling (IMSA-BCS), multi-task BCS (MT-BCS), multi-frequency BCS (MF-BCS), total-variation CS (TV-CS).

Published Journals Papers

[R1] N. Anselmi, A. Polo, M. A. Hannan, M. Salucci, and P. Rocca, “Maximum BCE synthesis of domino-tiled planar arrays for far-field wireless power transmission,” *J. Electromagn. Waves Appl.*, September 2020. doi: https://doi.org/10.1080/09205071.2020.1814166.

[R2] L. Poli, D. Masotti, M. Hannan, A. Costanzo and P. Rocca, “Codesign of switching sequence and diode parameters for multiple pattern optimization in time-modulated arrays," *IEEE Antennas Wirel. Propag. Lett.,* July 2020. doi: 10.1109/LAWP.2020.3010824.

[R3] A. Massa, N. Anselmi, L. Dall’Asta, G. Gottardi, S. Goudos, A. Hannan, J. Huang, M. Li, G. Oliveri, L. Poli, A. Polo, P. Rocca, A. Salas, M. Salucci, and S. Yang, “Teaching electromagnetics to next-generation engineers - The ELEDIA recipe, *IEEE Antennas Propag. Mag. - Special Issue on ’From Engineering Electromagnetics to Electromagnetic Engineering: Teaching/Training Next Generations,’* vol. 62, no. 2, pp. 50-61, April 2020. doi: 10.1109/MAP.2020.2970307.

[R4] G. Mansutti, P. De Carlo, M. A. Hannan, F. Boulos, P. Rocca, A. D. Capobianco, M. Mangarotto, and A. Tuozzi, “Modeling and design of a plasma-based transmit-array with beam scanning capabilities,” *Results in Physics*, vol. 16, pp. 102923, 2020. doi: https://doi.org/10.1016/j.rinp.2019.102923.

[R5] P. Rocca, M. A. Hannan, L. Poli, N. Anselmi, and A. Massa, “Optimal phase-matching strategy for beam scanning of sub-arrayed phased arrays” *IEEE Trans. Antennas Propag.*, vol. 67, no. 2, pp. 951-959, Feb. 2019.

[R6] G. Oliveri, G. Gottardi, M. A. Hannan, N. Anselmi, and L. Poli, “Autocorrelation-driven synthesis of antenna arrays - The case of DS-based planar isophoric thinned arrays,” *IEEE Trans. Antennas Propag.*, vol. 68, no. 4, pp. 2895-2910, Apr. 2020.

[R7] M. Salucci, L. Tenuti, G. Gotterdi, M. A. Hannan, and A. Massa, “A System-by-design method for efficient linear array miniaturisation through low-complexity isotropic lenses” *Electronics Letters*, vol. 55, no. 8, pp. 433-434, May 2019.

[R8] J. Guo, L. Poli, M. A. Hannan, P. Rocca, S. Yang and A. Massa, "Time-modulated arrays for physical layer secure communications: optimization-based synthesis and experimental assessment," IEEE Transactions on Antennas and Propagation, vol. 66, no. 12, pp. 6939-6949, Dec. 2018.

[R9] M. Bertolli, M. Donelli, A. Massa, G. Oliveri, A. Polo, F. Robol, L. Poli, A. Gelmini, G. Gottardi, M. A. Hannan, L. T. P. Bui, P. Rocca, C. Sacchi, F. Viani, T. Moriyama, T. Takenaka, and M. Salucci, "Computational methods for wireless structural health monitoring of cultural heritages," *Journal of Physics: Conference Series*, vol. 1131, pp. 1-7, 2018.

[R10] M. Salucci, F. Robol, N. Anselmi, M.A. Hannan, P. Rocca, G. Olivery, M. Donelli, and A. Massa, "S-band spline-shaped aperture-stacked patch antenna for air traffic control applications," *IEEE Trans. Antennas Propag.*, vol. 66, no. 8, pp. 4292-4297, Aug. 2018.

[R11] N. Anselmi, G. Oliveri, M. A. Hannan, M. Salucci, and A. Massa, "Color compressive sensing imaging of arbitrary-shaped scatterers," *IEEE Trans. Microw. Theory Techn.*, vol. 65, no. 6, pp. 1986-1999, June 2017.

[R12] P. Rocca, M. A. Hannan, M. Salucci, and A. Massa, “Single-snapshot DoA estimation in array antennas with mutual coupling through a multi-Scaling bayesian compressive sensing Strategy,” *IEEE Trans. Antennas Propag.*, vol. 65, no. 6, pp. 3203-3213, June 2017.

Published Conference Papers

[C1] M. A. Hannan and P. Rocca, "Directions-of-Arrival estimation in linear sub-arrayed array through Compressive Sensing," 2019 *IEEE AP-S International Symposium on Antennas and Propagation & USNC/URSI National Radio Science Meeting*, Atlanta, Georgia, 7-12 July 2019.

[C2] P. Rocca, M. A. Hannan, and G. Oliveri, "Advanced real-time strategies for direction finding in rapidly changing scenario," *2019 IEEE International Conference on Microwaves, Communications, Antennas and Electronic Systems (COMCAS)*, Tel-Aviv, 2019.

[C3] M. A. Hannan, L. Poli, G. Oliveri, and A. Massa, "Array Synthesis in the Autocorrelation Domain - Proof and Research Tracks," *2019 IEEE AP-S International Symposium on Antennas and Propagation & USNC/URSI National Radio Science Meeting*, Atlanta, Georgia, 7-12 July 2019.

[C4] P. Rocca, L. Poli, M. A. Hannan, S. Yang and A. Massa, "Cybersecurity in New Communications Systems through 4D Array Architectures," *13th European Conference on Antennas and Propagation (EuCAP)*, Krakow, Poland, 2019, pp. 1-4.

[C5] G. Mansutti, M. A. Hannan, P. Rocca, F. Boulos, A. D. Capobianco, P. D. Carlo, A. Tuozzi, "Design of a reconfigurable metal-plasma L-band transmit-array antenna," *2019 IEEE AP-S International Symposium on Antennas and Propagation & USNC/URSI National Radio Science Meeting*, Atlanta, Georgia, 7-12 July 2019.

[C6] N. Anselmi, M. A. Hannan, and P. Rocca, “Optimal synthesis of maximally robust antenna arrays by means of circular interval arithmetics” *2019 IEEE AP-S International Symposium on Antennas and Propagation & USNC/URSI National Radio Science Meeting*, Atlanta, Georgia, 7-12 July 2019.

[C7] G. Gottardi, M. A. Hannan, and A. Polo, "A multi-focusing contrast source Bayesian compressive method for solving inverse scattering problems," *9th International Workshop on New Computational Methods for Inverse Problems (NCMIP 2019),* Cachan, France, May 24, 2019.

[C8] G. Gottardi, M. A. Hannan, and A. Polo, "NDT/NDE by means of a probabilistic differential compressive sensing method," *9th International Workshop on New Computational Methods for Inverse Problems (NCMIP 2019)*, Cachan, France, May 24, 2019.

[C9] A. Polo, M. A. Hannan, G. Gottardi, and F. Viani, "A learning-based inversion strategy for passive wireless detection of crowds," 9th International Workshop on New Computational Methods for Inverse Problems (NCMIP 2019), Cachan, France, May 24, 2019.

[C10] G. Gottardi, M. A. Hannan, B. Li, A. Polo, M. Salucci, and F. Viani, "PCA-Based inversion of WiFi signal for robust device-free indoor target detection," *9th International Workshop on New Computational Methods for Inverse Problems (NCMIP 2019)*, Cachan, France, May 24, 2019.

[C11] G. Gottardi, M. A. Hannan, and A. Polo, "Compressive sensing computational methods for inverse scattering problems," *9th International Workshop on New Computational Methods for Inverse Problems (NCMIP 2019)*, Cachan, France, May 24, 2019.

[C12] F. Boulos, L. Dall'Asta, G. Gottardi, M. A. Hannan, A. Polo, and A. Salas-Sanchez, "A convex optimization-based inversion method for the Synthesis of monopulse linear arrays," *9th International Workshop on New Computational Methods for Inverse Problems (NCMIP 2019)*,Cachan, France, May 24, 2019.

[C13] F. Boulos, L. Dall'Asta, G. Gottardi, M. A. Hannan, A. Polo, A. Salas-Sanchez, and M. Salucci, "A computational inversion method for interference suppression in reconfigurable thinned ring arrays," *9th International Workshop on New Computational Methods for Inverse Problems (NCMIP 2019)*, Cachan, France, May 24, 2019.

[C14] G. Gottardi, M. A. Hannan, A. Polo, M. Salucci, and F. Viani, "Frequency-based inversion of a single wireless link for indoor passive target detection," *9th International Workshop on New Computational Methods for Inverse Problems (NCMIP 2019)*, Cachan, France, May 24, 2019.

[C15] N. Anselmi, M. A. Hannan, L. T. P. Bui, L. Dall'Asta, G. Gottardi, P. Rocca, and A. Massa, "Sparse wideband linear arrays synthesis via compressive processing methods," *2018 International Applied Computational Electromagnetics Society Symposium*, ACES 2018, Beijing, China, July 29 - August 1, 2018.

[C16] M. A. Hannan, N. Anselmi, G. Oliveri and P. Rocca, "Robust BCS-based direction-of-arrival and bandwidth estimation of unknown signals for cognitive radar," *2018 IEEE AP-S International Symposium on Antennas and Propagation & USNC/URSI National Radio Science Meeting*, Boston, Massachusetts, 8-13 July 2018.

[C17] A. Massa, M. Bertolli, G. Gottardi, A. Hannan, D. Marcantonio, G. Oliveri, A. Polo, F. Robol, P. Rocca, and F. Viani, “Compressive sensing as applied to antenna arrays: synthesis, diagnosis, and processing,“ *2018 IEEE International Symposium on Circuits & Systems (ISCAS 2018)*, Firenze, Italy, pp. 1-5, May 27-30, 2018.

[C18] M. Bertolli, M. Donelli, A. Massa, G. Oliveri, A. Polo, F. Robol, L. Poli, A. Gelmini, G. Gottardi, M. A. Hannan, L. T. P. Bui, P. Rocca, C. Sacchi, F. Viani, T. Moriyama, T. Takenaka, and M. Salucci, "Computational methods for wireless structural health monitoring of cultural heritages," *8th International Conference on New Computational Methods for Inverse Problems (NCMIP 2018)*, Cachan, France, May 25, 2018.

[C29] L. T. P. Bui, M. A. Hannan, N. Anselmi, L. Poli, and P. Rocca, “Optimal synthesis of wideband planar phased arrays with maximum bandwidth,” *2018 12th European Conference on Antennas and Propagation (EUCAP 2018)*, London, United Kingdom, April 9-13, 2018.

[C20] M. A. Hannan, N. Anselmi, G. Oliveri and P. Rocca, "Joint DoA and bandwidth estimation of unknown signals through single snapshot data and MT-BCS approach," *2017 IEEE AP-S International Symposium on Antennas and Propagation & USNC/URSI National Radio Science Meeting*, San Diego, CA, July 9-14, 2017.

[C21] M. A. Hannan, M. Salucci, G. Gottardi, L. Poli, and P. Rocca, “Advanced time-modulated array synthesis for directional modulation optimization,“ *2017 IEEE AP-S International Symposium and USNC-URSI Radio Science Meeting*, San Diego, California, USA, pp. 2027-2028, July 9-15, 2017.

[C22] G. Gottardi, L. Poli, M. A. Hannan, and P. Rocca, "Wideband phased arrays optimal design through convex programming," *2016 IEEE AP-S International Symposium and USNC-URSI Radio Science Meeting*, Fajardo, Puerto Rico, pp. 767-768, June 26 - July 1, 2016.

[C23] L. Poli, G. Oliveri, M. A. Hannan, and A. Massa, “DS-based thinned planar arrays with arbitrary non-square lattice,” *10th European Conference on Antennas and Propagation (EUCAP 2016)* (DOI: 10.1109/EuCAP.2016.7481579), Davos, Switzerland, pp. 1-3, April 11-15, 2016.

[C24] N. Anselmi, M. Donelli, M. A. Hannan, G. Oliveri, L. Poli, P. Rocca, M. Salucci, L. Tenuti, and A. Massa, “Inverse scattering methodologies and applications @ ELEDIA Research Center,” Atti XXI Riunione Nazionale di Elettromagnetismo (XXI RiNEm), Parma, pp. 152-155, 12-14 Settembre 2016.

[C25] M. A. Hannan, L. Poli, P. Rocca, and A. Massa, "Pulse sequence optimization in time-modulated arrays for secure communications," *2016 IEEE AP-S International Symposium and USNC-URSI Radio Science Meeting*, Fajardo, Puerto Rico, pp. 695-696, June 26 - July 1, 2016.

Contents

List of Tables

List of Figures

List of Abbreviation

DoA **D**irection-of-**A**rrivals

SNR **S**ignal-to-**N**oise **R**atio

RMSE **R**oot **M**ean **S**quare **E**rror

OCV **O**pen **C**ircuit **V**oltage

CS **C**ompressive **S**ensing

TVCS **T**otal **V**ariation **C**ompressive **S**ensing

ST-BCS **S**ingle-**T**ask **B**ayesian **C**ompressive **S**ensing

MT-BCS **M**ulti-**T**ask **B**ayesian **C**ompressive **S**ensing

IMSA **I**terative **M**ulti-**S**caling g

MFBCS **M**ulti-**F**requency **B**ayesian **C**ompressive **S**ensing

MFSS **M**ulti-**F**requency **S**ingle-**S**napshot

MFMS **M**ulti-**F**requency **M**ulti-**S**napshot

RIP **R**estricted **I**sometry **P**roperty

ARoI **A**ngular **R**egion of **I**nterest

MC **M**utual **C**oupling

PLF **P**olarization **L**oss **F**actor

MUSIC **Mu**ltiple **S**ignal **C**lassification

ESPRIT Signal **E**stimation **P**arameter via **R**otational **I**nvariance **T**echnique

ML **M**aximum **L**ikelihood

SVM **S**upport **V**ector **M**achine

RVM **R**elavance **V**ector **M**achine

SoA **S**tate-**o**f-the-**A**rt

BW **B**and**w**idth

List of Symbols

$\mathbf{a}$	Steering vector
A	Steering matrix
A_t	Sub-array transformation matrix
A_{sub}	Sub-array transformation matrix
B	Piecewise sinusoidal basis function
C	Number of different sub-array configurations
d	Inter-element spacing
E^{inc}	Magnitude of incoming signal
f	Working frequency
G	Number of basis function
h	Height of dipole
$\boldsymbol{\mathcal{H}}$	Antenna effective length
K	Number of angular samples
L	Number of incoming signals
M	Number of elements
N	Number of frequency samples
p	BCS hyper-parameter vector
$\mathbf{p}$	BCS hyper-parameter vector
P	Number of elements in each sub-arrays
Q	Number of sub-arrays
R	Number of multi-resolution steps
$\mathbf{s}$	Vector of incoming signals
S	Number of DoA sets
T	Number of noise realizations/trials
$\mathbf{V}$	Vector of open circuit voltages

v	Open circuit voltage
W	Number of snapshots
λ	Wavelength
β	Wave number
θ	Angular directions
η	Additive white noise
$\boldsymbol{\theta}$	Vector of angular directions
$\boldsymbol{\eta}$	Vector of additive white noise
σ^2	Noise variance
μ	TV-CS penalty parameter
ρ, γ	Lagrangian multifier vectors
ς	Radius of dipole
τ	Threshold
ξ	Confidence level
Ω	Maximum angular range extension
Ψ	Clutter directions
δ	Clutter width
$\widehat{\mathbf{s}}$	Bare BCS solutions
$\widetilde{\mathbf{s}}$	Thresholded BCS solutions
$\widehat{L}$	Number of estimated signal before thresholding
$\widetilde{L}$	Number of estimated signal after thresholding

Chapter 1

Introduction

In this Chapter, the main motivations of choosing this topic are briefly described. Moreover, the main objectives and contributions of this thesis are also listed.

1.1 Motivations

The proliferation of wireless services, the Internet of things, and the next-generation cellular networks are boosting the diffusion of wireless devices. In this regard, the estimation of the directions-of- arrivals (*DoAs*) of signals impinging on a direction finding system is a key problem for the evolution of future wireless systems. Moreover, the knowledge of the *DoAs* enhances the capability to reconfigure the transmitting/receiving systems and to process the signals despite impairments in the communication systems.

Recently, the sparse processing of signals for *DoAs* estimation in the framework of Compressive Sensing (*CS*) has received great attention as it provides accurate and real time estimation with no a-prior knowledge of number of incoming signals. In addition, the voltages collected at the sensors are directly used to estimate the DoA without the need to compute the complex correlation matrix.

1.2 Objectives

The main objectives of this thesis are listed as follows:

1. study and development of CS-based innovative strategies for $DoAs$ estimation purpose;

2. adapt and apply the developed approaches to:

   - different specific applications: real-time applications, cognitive radars, and $5G$;
   - different characteristics of the sources: narrow band, wide band, and clutters;
   - different systems: linear array, planar array, and sub-arrayed array;

3. extensive analysis of the performances of the developed methods for different $DoFs$, EM scenarios, and conditions:

   - varying the number of elements of the array;
   - varying number of signals;
   - varying noise levels;
   - real antenna element with mutual coupling and polarization loss.

1.3 Contributions

The main contributions of this thesis are listed as follows:

1. theoretical - formulations of $DoAs$ estimation problem for different signals and systems;
2. methodological - development of different $CS-$based strategies for $DoAs$ estimation;
3. resource - implementation of the developed strategies;
4. analytical - extensive numerical analysis of the behaviour of the proposed approaches.

1.4 Outline

The outline of this thesis is listed as follows:

- *Chapter 2* - the state-of-the-art $DoAs$ estimation problem is reviewed in details;
- *Chapter 3* - the general $DoAs$ estimation problem is formulated mathematically and reformulated in the state-of-the-art CS framework;
- *Chapter 4* - an improved version of the state-of-the-art $ST-BCS$ method called $IMSA-BCS$ is proposed, validated, and analyzed extensively;
- *Chapter 5* - an improved version of the state-of-the-art $MT-BCS$ method called $MF-BCS$ is proposed, validated, and analyzed extensively;
- *Chapter 6* - the state-of-the-art $ST-BCS$ and $MT-BCS$ methods are analyzed for the different linear and planar sub-array geometries;
- *Chapter 7* - the state-of-the-art $TV-CS$ approach is vigorously adapted and applied for estimating closely spaced sources or clutters;
- *Chapter 8* - some concluding remarks are summarized and some scopes of future research are listed.

Chapter 2

A Brief Literature Review

In this Chapter, the state-of-the-art literature of directions-of-arrival (*DoAs*) estimation is reviewed focusing on the methodological advancement in the context of different innovative systems and applications.

Directions-of-arrival (*DoAs*) estimation has been a known area of research for long time. It has been studied extensively in various disciplines and applied fruitfully in many fields of engineering including radar, sonar, navigation, smart antennas, geophysical and seismic sensing. A plethora of methods for finding *DoAs* have been proposed in the state-of-the-art literature of *DoAs* estimation. Many dedicated books [1]-[7] addressing only *DoAs* estimation problem are published by well known researcher all over the world.

Although it is a matured topic, it becomes a research of great interest nowadays which is evident from the increased number of publications and the number of PhD [8]-[16] from renowned institutions. The recent highly increasing development of the wireless technologies and the advancements of the various classical and modern estimation algorithms are opening doors of huge potentialities for many innovative applications in next generation cellular/wireless communications, internet-of-things (IoTs), vehicular technology, unmanned aerial vehicles (UAVs) and so on.

The knowledge of the *DoAs* of signals arriving on an antenna system is considered as an advantage in many fields of engineering. For example, in wireless communication, it allows to enable adaptive beam-forming, which enhances the sensitivity of the system towards desired directions suppressing at the same time the undesired interference. In acoustic, it is often required to find the directions where the sound sources are located or the direction of reflected sound signals (e.g., *SONAR*). In radar, *DoAs* estimation is useful for target acquisition and for air traffic control. In space exploration, the knowledge of *DoAs* helps astronomer to look at the certain location in the sky. In surveillance, *DoAs* could help the system to focus along the desired regions of interest. Therefore, many attractive applications are possible for the recent technological race of wireless devices. As a matter of fact, the dramatically increased wireless services are boosting the development of an efficient and robust advances*DoA* estimation technique for the future evolution of wireless systems. The immense interest in both academic and industrial communities for reliable and effective methods are evident from the recently published number of books, journals, proceedings, and seminars. As a matter of fact, the advances on *DoAs* estimation have been reviewed almost every year since last decade [17]-[29]. Methodology based review is covered by most of the review papers while only few reviews based on the specific applications and systems.

The classical *DoAs* estimators are essentially based on the sub-space based estimation approaches. In this category of estimator, the common and widely used estimators are multiple signal classification (*MUSIC*) [30] and its different improved versions[31]-[37], the signal estimation parameters via rotational in-variance technique (*ESPRIT*) [38] and its different versions [39]-[43], and the maximum likelihood (*ML*) DoA estimator [44]-[46] and others [47, 49, 50]. However, the two main drawbacks of the sub-space based estimator are - (I) they often need to know a-priory number of incoming signals, which is quite prohibitive nowadays and (II) they need to compute complex co-variance matrix which slows the *DoAs* estimation and requires an hardware implementation of the receiver too complex for most mobile systems and devices.

On the other hand, the aforementioned constraints of classical *DoAs* estimators are not a limiting factor for the modern estimators based on machine learning theories. For instance, learning-by-example (*LBE*) approaches based on radial-basis functions (*RBF*s) [51], neural networks (*NN*s) [52], or support vector machines (*SVM*s) [53]-[55] have been also proposed where the *DoA* estimation problem has been recast to a probabilistic framework. Although efficient for some applications, they need to be trained by means of a pre-defined set of the known input-output examples for all possible combination of prospective incoming DoAs. Therefore, machine learning based modern estimators are application specific and can not be used as a general purpose.

However, all the aforesaid classical and modern estimators also need adequate number of snapshots data in order to have a reliable estimation. As a result, the are not suitable for the applications where the estimation must be in real time although *LBE*-based methods have proved to be promising solutions also for real-time localizations [52][53][54].

Sparse processing [56]-[62] for signal reconstructions has recieved great attention since last two decades. In this framework, strategies based on the compressive sensing (*CS*) theory [59]-[61] have recently been introduces thanks to their effectiveness, flexibility, and computional efficiency to deal with complex engineering problems in electromagnetics [63]-[68] including antenna array synthesis [69]-[70] and imaging [71]-[75].

Exploiting the key observation that the impinging *DoAs* on the antenna array are intrinsically *sparse* in the spatial domain, *CS* based deterministic solvers have been proposed for *DoAs* estimations where the sparsity constraints have been imposed through a l_p-norm minimization [57],[76]-[77]. However, the condition of restricted isometry property (*RIP*) must be satisfied by the 'sampling matrix' in order to guarantee reliable estimations. Unfortunately, because of the computational burden *RIP* cannot be easily verified [59]. As an alternative, methods based on the Bayesian compressive sensing (*BCS*) [61] have been proposed where the original deterministic problem is reformulated in the probabilistic framework and then efficiently solved with the relevance vector machine (*RVM*) [56].

The *BCS*-based strategies have been effectively applied for *DoAs* estimation for different purposes [78]-[84]. In [78], the *DoA* estimation problem is formulated within the *BCS* framework thus avoiding constraints on the sampling (or observation) matrix, which directly links the measurements (i.e., voltages/currents) at the output of the array elements to the unknown signal directions. Two *BCS*-based *DoAs*estimation strategies named single-task *BCS* ($ST-BCS$) and multi-task *BCS* ($MT-BCS$) have been proposed in [78]. The former is concerned with single time-instant measurements (i.e., single snapshot) to enable the real-time estimation, while the latter is aimed at giving high-resolution estimations, thanks to the processing over multiple snapshots, still avoiding any *a-priori* information on the number and the intensity of the unknown impinging signals.

This thesis work aims at addressing the following issues of $DoAs$ estimation in CS framework:

1. developing innovative strategies in order to improve the performance of the $ST-BCS$ approach;

2. developing innovative strategies in order to improve the performance of the $MT-BCS$ approach;

3. extensive analysis of state-of-the-art $ST-BCS$ and $MT-BCS$ methods for sub-arrayed geometries;

4. develop CS based strategies for innovative applications.

All the aforementioned issues are addressed successfully in this thesis. The outcomes have already been published [29],[81]-[84] in the state-of-the-art literature and some are in under review process.

Chapter 3

Mathematical Formulations

In this Chapter, the general DoA estimation problem is defined mathematically including the polarization loss and mutual coupling. Then the problem in hand is reformulated in Compressive Sensing (CS) framework. After satisfying the fundamental requirements of CS, the state-of-the-art CS strategies for $DoAs$ estimation are described in details. In addition, the DoA estimation problem is addressed through Bayesian Compressive Sensing (BCS) based approaches like single-task BCS ($ST - BCS$) and multi-task BCS ($MT - BCS$).

3.1 Definition of Signal Model

Based on the sources positions (e.g., distance) relative to the reference point of the sensors, the *DoA* estimation problem can be broadly categorized into:

1. Far-field *DoA* estimation.

2. Near-field *DoA* estimation.

Although the general idea of estimating far-field and near-field *DoA* are same, their signal model is different. The fundamental difference between two signals models are the assumption of the incoming signals characteristics. For instance, in far-field condition (i.e., the distance between source and sensors reference point, $r > 2D^2/\lambda$, D being antenna aperture and λ being wavelength at working frequency), the incoming signals impinging on the sensors are assumed to be a plane wave. However, in near-field condition (i.e., sources are close to the sensors, $r < 2D^2/\lambda$), the assumption of the plane wavefront can no longer hold [15]. Instead, the incoming signals impinging on the sensors in the case of near-field condition are spherical waves. Therefore, the estimation problem in near-field case becomes the estimation *DoAs* and also ranges (i.e., distances of the sources). The details of the near-field *DoA* estimation problem is beyond the scope of this thesis. In order to know more in details about the near-field *DoA* estimation problem, formulation of signal model, and the potential applications, interested readers may go through the references [15, 125, 126].

The far-field *DoA* estimation problem is addressed in this thesis. Therefore, all the discussions hereinafter are based on the far-field approximation of the signal model. As a matter of fact, the incoming signals on the sensors array are assumed to be a plane wave. The mathematical formulation of the plane wave in the context of *DoA* estimation is described in details in Sect. 3.2. The interested readers may find out the details of the properties of the plane wave in [127]. Plane wave is the simplest solution of the Maxwell equation in vacuum. Therefore, it plays an important role in the development of electromagnetic. Moreover, a representative example of the plane wave is shown in Fig. 3.1 and some of its characteristics are short-listed as follows:

- it defines a plane along its direction of propagation where the field strength is uniform everywhere of that plane at any instant of time;

- it is a constant frequency wave whose wavefronts (surfaces of constant phase) are infinite parallel plane of constant amplitude normal to the phase velocity vector;

- its wavefronts are equally spaced by one wavelength λ;

- its wavefront propagate at speed of light;

- no electric and magnetic field are in the direction of propagation (direction of the poynting vector), where the electric and magnetic field are perpendicular to each other;
- the value of the magnetic field is equal to the value of the electric field divided by impedance of the medium (i.e., in free space, the impedance is ~ 377 [ohm]);
- any operator applied to the plane wave yields a plane;
- any linear combinations of the plane waves yields a plane wave.

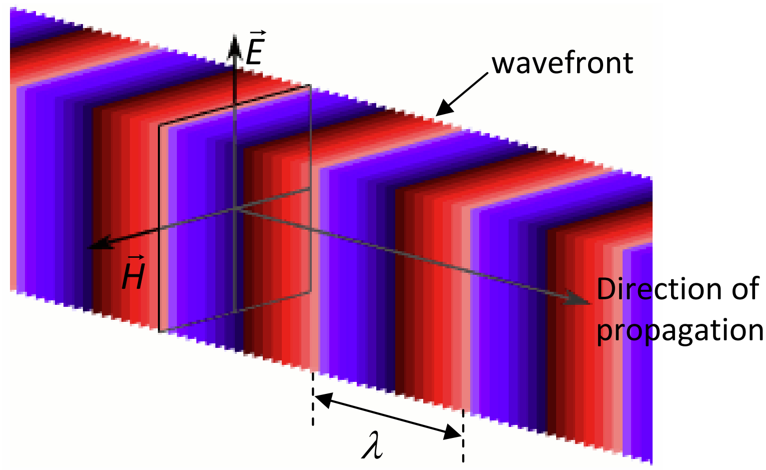

Figure 3.1: *Plane Wave* - The wavefronts of the plane wave.

3.2 Definition of DoA Estimation Problem

Consider a set of L narrow-band electromagnetic plane waves, $\mathbf{s}_l(\mathbf{r})$, $l = 1, ..., L$, impinging on a linear array of M parallel dipoles from directions (θ_l, ϕ_l), $l = 1, ..., L$ and with arbitrary linear polarization $\widehat{\mathbf{u}}_l$, $l = 1, ..., L$ [Fig. 3.2]. The l-th plane wave is expressed as $\mathbf{s}_l(\mathbf{r}) = E_l^{inc} e^{-j\beta \hat{\mathbf{r}}_l \cdot \mathbf{r}} \widehat{\mathbf{u}}_l$ where $\beta = \frac{2\pi}{\lambda}$ is the wave number with λ the free-space wavelength of the carrier frequency, E_l^{inc} the amplitude of the l-th wave and the $\hat{\mathbf{r}}_l \cdot \mathbf{r}$ is defined as

$$\hat{\mathbf{r}}_l \cdot \mathbf{r} = (x \sin\theta_l \cos\phi_l + y \sin\theta_l \sin\phi_l + z \cos\theta_l) \ . \tag{3.1}$$

The dipoles are y-directed, of length h and radius ς (being $\varsigma \ll h$), connected at the center, and separated by a distance $d = \Delta x$ along the x-axis.

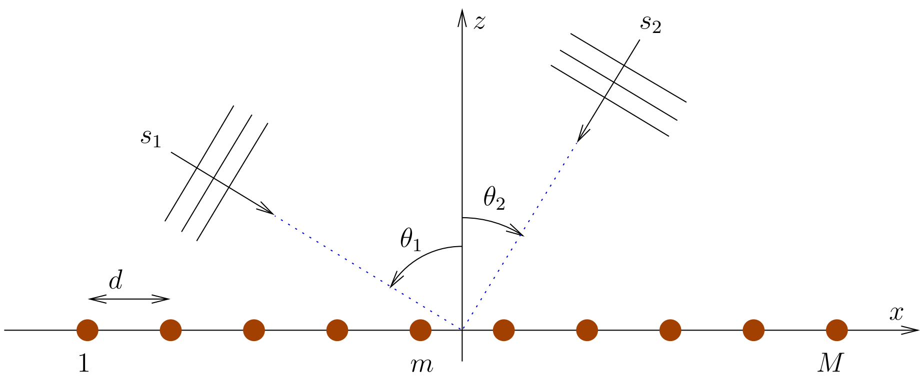

Figure 3.2: *Sketch of the reference scenario* - impinging plane waves on the linear adaptive antenna array.

The current $I_m(y)$ induced on the m-th dipole, supposed thin (i.e., $\varsigma \ll \lambda$), from the incident waves is computed by inverting the following integral equation [86], [87]

$$\frac{j}{\omega\epsilon_0}\left(\beta^2 + \frac{\partial^2}{\partial y}\right)\int_{-\frac{h}{2}}^{\frac{h}{2}} \frac{e^{-j\beta d}}{4\pi d} I_m(y')\, dy' = E_y^{inc}(y) \tag{3.2}$$

through the Method of Moments (MoM) [88] and using the Galerkin approach [89]. In (3.2), the distance $d = \sqrt{(y+y')^2 + \varsigma^2}$ is never zero, $y \in \left[-\frac{h}{2}; \frac{h}{2}\right]$, $\omega = \frac{2\pi c}{\lambda}$ is the angular frequency with c the speed of light in vacuum, and ϵ_0 the dielectric permittivity. Moreover,

$$E_y^{inc}(\mathbf{r}) = \sum_{l=1}^{L} \mathbf{s}_l(\mathbf{r}) \cdot \widehat{\mathbf{y}} \tag{3.3}$$

the y-component of the total incident field, being $\widehat{\mathbf{y}}$ the unit vector along the y-direction. In the MoM, G piecewise sinusoidal basis functions $B_g(y)$, $g = 1, ..., G$ (with G odd) [90] are used for representing the current on the m-th dipole as

$$I_m(y) = \sum_{g=1}^{G} I_{m,g} B_g(y) \ . \tag{3.4}$$

The voltages, including the self and mutual coupling effects, are then computed as

$$v_m = v_{m,g}\big|_{g=\frac{N+1}{2}} = \sum_{p=1}^{M}\sum_{q=1}^{G} Y_{m,g;p,q} I_{m,g} \ , \ m = 1, ..., M \tag{3.5}$$

where $Y_{m,g;p,q}$ is the impedance term that defines the voltage at the g-th segment of the m-th dipole due to a unitary current in the q-th segment of the p-th dipole when the current in all other segments is zero [88]. For interested reader, the voltage equation without mutual coupling can defined as[78]:

$$v_m = \sum_{l=1}^{L} E_l^{inc} \hat{\mathbf{y}} \cdot \boldsymbol{\mathcal{H}} e^{j\beta x_m \sin\theta_l \cos\phi_l} \ , \ m = 1, ..., M \tag{3.6}$$

where $\boldsymbol{\mathcal{H}}$ is the antenna effective length supposed identical for all elements.[1] Finally, the open-circuit voltage (OCV) at the output of the m-th array element in a single time-instant (*single snapshot*) and used for the DoA estimation is equal to

$$V_m = v_m + \eta_m \ , \ \ m = 1, ..., M \tag{3.7}$$

where $\boldsymbol{\eta} = \{\eta_m : m = 1, ..., M\}$ is the additive noise data vector whose entries are samples of a statistically-distributed Gaussian function with zero mean and variance equal to the noise power. Because of the linear arrangement of the array elements, the DoA estimation is limited to the θ angle (i.e., $\phi = 0\,[deg]$). The DoA estimation problem is defined as the estimation of unknown directions θ_l, $l = 1, ..., L$, from the OCV of V_m, $l = 1, ..., L$. In matrix form, eq. (3.7) can be rewritten as follows

$$\mathbf{V} = A(\boldsymbol{\theta})\,\mathbf{s} + \boldsymbol{\eta} \tag{3.8}$$

where $\mathbf{V} = [V_1, \ldots, V_M]^T$ is a column vector of M complex entries ($\mathbf{V} \in \mathbb{C}^{M\times 1}$), T indicates the transpose, $\boldsymbol{\theta} = [\theta_1, ..., \theta_L]$, $A(\boldsymbol{\theta}) = [\mathbf{a}(\theta_1), \ldots, \mathbf{a}(\theta_L)] \in \mathbb{C}^{M\times L}$ is the matrix of the steering vectors whose l-th column is given by $\mathbf{a}(\theta_l) = \left[e^{j\beta x_1 sin\theta_l}, \ldots, e^{j\beta x_M sin\theta_l}\right]^T \in \mathbb{C}^{M\times 1}$, $l = 1, \ldots, L$, $\mathbf{s} = [E_1^{inc}, \ldots, E_L^{inc}]^T \in \mathbb{C}^{L\times 1}$, and $\boldsymbol{\eta} = [\eta_1, \ldots, \eta_M]^T \in \mathbb{C}^{M\times 1}$. It is worth noticing that the problem at hand is non-linear with respect to the unknowns, θ_l, $l = 1, \ldots, L$, which are present in the exponential terms of the elements of the matrix A.

[1] Without loss of generality, isotropic elements are assumed (i.e., $\boldsymbol{\mathcal{H}} = \mathbf{1}$).

3.3 Problem Formulation in CS Framework

The two fundamental conditions that must be satisfied in order to apply Compressive Sensing (CS) are (I) the signals to be recovered must be sparse, and (II) the problem to be solved must be linear. First of all, clearly the unknown is not sparse in the original scenario. Secondly, the problem at hand is non-linear with respect to the unknowns, θ_l, $l = 1, \ldots, L$, which are present in the exponential terms of the elements of the matrix A. In order to address the first condition, the following hypothesis is adopted:

A signal $\mathcal{F}(\mathbf{r}) = \sum_{n=1}^{N} x_n \psi_n(\mathbf{r})$ is $S-sparse$ with respect to ψ if $x = [x_1, ..., x_N]$ has at-most $S \ll N$ non-nul coefficient:

$$\mathcal{F}(\mathbf{r}_i) = \sum_{n=1}^{N} x_n \psi_n(\mathbf{r}_i) \tag{3.9}$$

where $x \in C^N$, $x = \{x_n; n = 1, ..., N\}$ are the signal coefficients and $\psi \in C^{N \times N}$, $\psi = \{\psi_{ni} = \psi_n(\mathbf{r}_i); n = 1, ..., N; i = 1, ..., I\}$ are the signal basis.

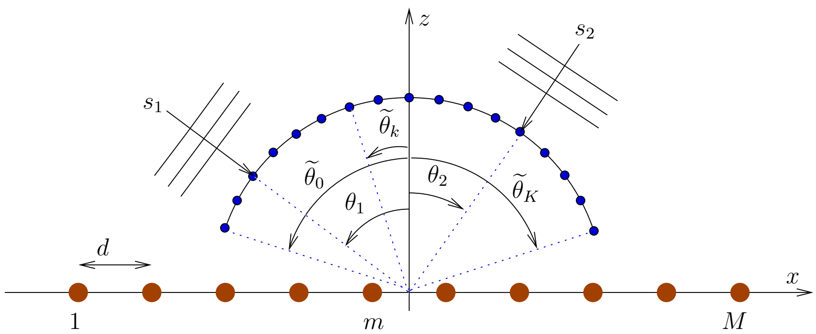

Figure 3.3: *Sketch of the sparse scenario* - angular domain discretization.

Therefore, sparsity is not an absolute concept but a relative one. Here the sparsity is exploited in the angular domain by discretizing the incidence field of view $\theta \in [-90 : 90]$ $[deg]$ into $K \gg L$ angular samples (Fig. 3.3) such that $A\left(\widetilde{\boldsymbol{\theta}}\right) \in \mathbb{C}^{M \times K}$ in (3.8) and the DoAs of the incoming signals are assumed to belong to the set of the K directions $\mathbf{\Gamma} = \left\{\hat{\theta}_k;\ k = 1, ..., K\right\}$. Therefore, the candidate scenario is sparse in spatial domain and the candidate directions $\hat{\theta}_k$ are directly asociated with the candidate signal vectors $\tilde{\mathbf{s}}_k$, $k = 1, ..., K$. As a result, the problem becomes linear with respect to the unknown signal vector $\tilde{\mathbf{s}}$.

3.4 CS-Based Methods

In order to have a reliable estimation, a necessary condition to be addressed when applying CS is the fact that the so-called 'sampling matrix' must satisfies the restricted isometry property (RIP). This property essentially deals with the ill-posedness of the CS problems. Unfortunately, such a condition cannot easily verified since it needs to evaluate the determinant of hugenumber of sub-matrices depending on number of elements and sparsity levels. As a matter of fact, verifying RIP condition are computationally demanding [59]. Therefore, the performances of the deterministic CS methods are greatly compromised as most of the cases the RIP condition can not be verified.

Alternatively, approaches based on the Bayesian Compressive Sensing (BCS) [61] have been proposed where verifying the RIP condition is no more the limiting factor of the solutions stability.

3.4.1 Single-Task Bayesian Compressive Sensing ($ST-BCS$)

In order to deal with the complex data, the guidelines in [69],[81] is adopted. First of all, eq. (3.8) is rewritten to yield a real-valued problem suitable for BCS as

$$\begin{bmatrix} \Re\{\mathbf{V}\} \\ \Im\{\mathbf{V}\} \end{bmatrix} = \begin{bmatrix} \Re\left\{A\left(\widetilde{\boldsymbol{\theta}}\right)\right\} & -\Im\left\{A\left(\widetilde{\boldsymbol{\theta}}\right)\right\} \\ \Im\left\{A\left(\widetilde{\boldsymbol{\theta}}\right)\right\} & \Re\left\{A\left(\widetilde{\boldsymbol{\theta}}\right)\right\} \end{bmatrix} \begin{bmatrix} \Re\{\widetilde{\mathbf{s}}\} \\ \Im\{\widetilde{\mathbf{s}}\} \end{bmatrix} + \\ + \begin{bmatrix} \Re\{\boldsymbol{\eta}\} \\ \Im\{\boldsymbol{\eta}\} \end{bmatrix}, \tag{3.10}$$

where $\mathbf{V} = \{V_m;\, m = 1, ..., M\}$, $\hat{\mathbf{A}} = \{\hat{\mathbf{a}}_k;\, k = 1, ..., K\}$ is the steering matrix whose k-th entry is $\hat{\mathbf{a}}_k = \left\{e^{j\beta x_m \sin\hat{\theta}_k};\, m = 1, ..., M\right\}$, and $\hat{\mathbf{s}} = \{\hat{s}_k;\, k = 1, ..., K\}$ is the signal vector on $\mathbf{\Gamma}$ with entries $\hat{s}_k = E_k^{inc}\delta_{kl}$, $k = 1, ..., K$, being $\delta_{kl} = 1$ if $\hat{\theta}_k = \theta_l$ and $\delta_{kl} = 0$ otherwise. Moreover, $\Re\{\cdot\}$ and $\Im\{\cdot\}$ are the real and the imaginary part respectively.
The sparse signal vector $\widehat{\mathbf{s}}_{ST-BCS}$ is retrieved [78] by looking for the maximum of the *a-posteriori* probability function

$$\mathcal{P}r\left(\left[\widehat{\mathbf{s}},\, \boldsymbol{\sigma}^2,\, \mathbf{p}\right] \mid \mathbf{V}\right) \tag{3.11}$$

given by its mean value

$$\widehat{\mathbf{s}}_{ST-BCS} = \frac{1}{\boldsymbol{\sigma}^2}\left(\frac{\hat{\mathbf{A}}\,\hat{\mathbf{A}}^T}{\boldsymbol{\sigma}^2} + diag\left(\mathbf{p}\right)\right)^{-1}\hat{\mathbf{A}}^T\mathbf{V} \tag{3.12}$$

because of the multi-dimensional Gaussian nature [61] of (3.11). In (3.12), the variance $\boldsymbol{\sigma}^2$ and the hyper-parameter vector $\mathbf{p}$, which forces the sparseness of the signal vector $\widehat{\mathbf{s}}$ [56], are determined through the maximization of the likelihood function

$$\mathcal{L}\left(\boldsymbol{\sigma}^2, \mathbf{p}\right) = -\frac{1}{2}\left[(2K)\log 2\pi + \log|\Xi| + \mathbf{y}^T\Xi^{-1}\mathbf{V}\right] \tag{3.13}$$

by means of the relevance vector machine (RVM) [69]. In (3.13), $\Xi \triangleq \boldsymbol{\sigma}^2\mathbf{I} + \hat{\mathbf{A}}\, diag\,(\mathbf{p})^{-1}\,\hat{\mathbf{A}}^T$, T being the transpose operation.

3.4.2 Multiple-Task Bayesian Compressive Sensing ($MT-BCS$)

The $MT-BCS$ approach [61] correlates the DoAs estimation over multiple snapshots in order to avoid the strong dependence of the estimation performance on the noise level of the measured voltages. The multiple-snapshots version of (3.8) can be written as

$$\mathbf{V}_w = A\left(\boldsymbol{\theta}\right)\mathbf{s}_w + \boldsymbol{\eta}_w,\ \ w = 1, ..., W, \tag{3.14}$$

where W is the number of snapshots. The sparse signal vector $\widehat{\mathbf{s}}_{MT-BCS}$ is determined as follows

$$\widehat{\mathbf{s}}_{MT-BCS} = \frac{1}{W}\sum_{w=1}^{W}\left\{\arg\left[\max_{\widehat{\mathbf{s}}_w}\mathcal{P}r\left(\left[\widehat{\mathbf{s}}_w,\, \mathbf{p}\right]\middle|\, \mathbf{V}_w\right)\right]\right\} \tag{3.15}$$

where $\widehat{\mathbf{s}}_w$, $w = 1, ..., W$, are statistically-correlated through a hyperparameter vector which correlates the different snapshots. The optimal value of $\mathbf{p}$, $\mathbf{p}_{MT-BCS}$, is computed as $\mathbf{p}_{MT-BCS} = \arg\max_{\mathbf{p}}\left\{\mathcal{L}^{MT-BCS}\left(\mathbf{p}\right)\right\}$ through the RVM according to the guidelines in [69], being

$$\begin{aligned}\mathcal{L}^{MT-BCS}\left(\mathbf{p}\right) = -\tfrac{1}{2}\textstyle\sum_{w=1}^{W}\{\log\left(|C_{MT-BCS}|\right) + \\ (K+2\varphi_1)\log\left[\mathbf{V}_w^T\left(C_{MT-BCS}\right)\mathbf{V}_w + 2\varphi_2\right]\}\end{aligned} \tag{3.16}$$

where $C_{MT-BCS} \triangleq I + \widehat{A}\left(\widetilde{\boldsymbol{\theta}}\right) diag\,(\mathbf{p})^{-1}\,\widehat{A}\left(\widetilde{\boldsymbol{\theta}}\right)^T$ and φ_1, φ_2 are user-defined parameters [61]. The knowledge/estimation of the variance σ^2 of the noise samples is not required in the $MT-BCS$ based method [69], unlike the $ST-BCS$ approach. The $MT-BCS$ solution turns out equal to

$$\widehat{\mathbf{s}}_{MT-BCS} = \frac{\sum_{w=1}^{W}\left\{\left[\widehat{A}\left(\widetilde{\boldsymbol{\theta}}\right)^T\widehat{A}\left(\widetilde{\boldsymbol{\theta}}\right) + diag\,(\mathbf{p})\right]^{-1}\widehat{A}\left(\widetilde{\boldsymbol{\theta}}\right)^T\mathbf{V}_w\right\}}{W}. \tag{3.17}$$

3.4.3 Estimation of DoA from BCS Solutions

As we have seen, the *BCS* methods are not applied directly to estimate the directions $\widetilde{\boldsymbol{\theta}}$ but the signals vector $\widehat{\mathbf{s}}$. Once the signals vector are estimated by *STBCS* e.g., $\widehat{\mathbf{s}}_{ST-BCS}$ or by *MTBCS* e.g., $\widehat{\mathbf{s}}_{MT-BCS}$, an energetic thresholding [78] is applied in order to remove the low-energy "artifacts" caused by the environmental noise and/or the measurement uncertainties. More specifically, the values $\hat{s}_k$, $k = 1, ..., K$ are firstly ranked according to their energy content (i.e., $\hat{s}_1 = \arg\left\{\max_{k=1,...,K} |\hat{s}_k|^2\right\}$ and $\hat{s}_K = \arg\left\{\min_{k=1,...,K} |\hat{s}_k|^2\right\}$). Successively, the last $\left(K - \widetilde{L} + 1\right)$ ones are filtered out [i.e., $\hat{s}_k^{BCS} = 0$, $k = \left(K - \widetilde{L} + 1\right), ..., K$], $\widetilde{L}$ being the *BCS*-estimated number of signals satisfying the following condition

$$\sum_{l=1}^{\widetilde{L}} |\hat{s}_l|^2 \;\leq\; \tau \times \left(\sum_{k=1}^{K} |\hat{s}_k|^2\right) \tag{3.18}$$

where μ is a user-defined threshold [78]. Finally, the estimated *DoA* vector, $\hat{\boldsymbol{\theta}}_{BCS} = \left\{\hat{\theta}_l : l = 1, ..., \hat{L}\right\}$ is determined by selecting the angles $\hat{\boldsymbol{\theta}}_{BCS}$ of the steering vectors $\hat{\mathbf{a}}_k$, $k = 1, ..., K$ associated to the non-trivial terms of the thresholded $\widehat{\mathbf{s}}_{BCS}$ vector.

Chapter 4

Performance Improvement of ST-BCS

In this Chapter, an improved version of $ST-BCS$ estimation method called $IMSA-BCS$ is proposed. It exploits the information on the *degree of reliability* obtained by $ST-BCS$ to improve the efficiency of the estimation. Moreover, the proposed method can be applied in real time applications. In addition, the estimation is not confined to any predefined grid as it refines grid at each $IMSA$ step. Therefore, it is essentially a grid-less $DoAs$ estimator. Finally, the main outcomes of this work are essentially summarized in [29],[81].

4.1 Introduction

A system is usually designed to estimate direction as a final objective (e.g., dedicated system for DoA estimation) or as a primary objective (i.e., estimate DoA as a prior knowledge to be utilized for other purposes). In both cases, most of the applications demand accurate and real-time estimation, although accuracy and time are considered as trade-off in reality. Therefore, the study of DoA estimation problem is focused nowadays on finding optimal accuracy of estimation in any instant of time. However, the research addressing the aforementioned problem can hardly be seen in the literature because most of the classical and modern estimators are based upon the computationally intensive strategies i.e., needed multiple snapshots data and eigen-decomposition of complex co-variances and so on. For example, the real-time $DoAs$ estimator proposed in [43] is essentially based on the widely used subspace based strategy named the signal estimation parameter via rotational in-variance technique ($ESPRIT$) [38]. The accuracy of the estimation in [43] is highly compromised although it considered multiple snapshot data. Kim et. al. [48] developed a fast DoA estimation algorithm called the pseudo-covariance matrix technique, which estimated fast varying signals in two steps (i.e., the rough estimation using bearing response and then exact estimation by combing the bearing response and the directional spectrum). As a matter of fact, it requires the solution of a nonlinear-generalized- eigenvalue equation of a pseudo-covariance matrix, resulting a high computational burden even for the single snapshot data. Huang in [49] proposed a fast estimation method based on [48] where the nonlinear-generalized-eigenvalue equation is rewritten as a linear-matrix equation formed by forward- backward data matrix. This is done by converting of received data vector into overlapping sub-arrays of much higher data samples than the original received data. Again, this is subject to post-processing of received data vector which becomes computationally expensive with the increase of number of elements. In order to avoid inherent complexity of the estimator based on classical methods, Lin et. al. [50] proposed a real-time DoA estimation technique by simply comparing the received signal strength among the different ports of the Rotman lens. Although it is fast, the performance is affected severely by different noisy scenario. Recently, sparse processing thanks to their computational efficiency has received great attention in electromagnetic [67, 78] and antenna array synthesis, analysis, and processing [26]. In this framework, Compressive Sensing (CS) based orthogonal matching pursuit (OMP) and sparse Bayesian learning (SBL) approaches have been proposed in [116]. However, although it is fast, it used multi-temporal data to build covariance matrix which is not appropriate for real-time estimation. In order to avoid computing covariance matrix, Bayesian Compressive Sensing (BCS) [78] is proposed which can be applied directly on the received data vectors without computing complex covariance matrix. However, although [78] outperforms with respect to classical [30, 38, 44] and modern estimator [55], it also needs multi-snapshot data in order

to have robust estimation. In this Chapter, the methods in [78] is extended by exploiting the inherent properties of the BCS in order to address the problem of finding optimal accuracy of estimation in real-time (with single snapshot data and with insignificant computational burden). In particular, the $ST-BCS$ [78] is extended as $IMSA-BCS$ [81] to retrieve narrowband DoAs.
This chapter deals with the recovery of the signal DoA from data collected at a single time instant (*single-snapshot*) through a dipole antenna array, when considering mutual coupling effects and polarization losses. The estimation method, preliminary presented in [80] for the ideal array case (i.e., isotropic elements without mutual coupling) and avoiding the computation of the covariance matrix, is based on the integration of the DoA-based BCS with a grid refinement strategy. The BCS, successfully applied in a wide number of electromagnetic applications [69]-[67], provides not only an estimation of the DoA [78], [79] but also of the *degree of reliability* of the estimates [70]. The multi-resolution angular grid refinement is instead exploited to effectively cope with the problem of the off-grid signals (i.e., signals whose actual DoA do not belong to the discretization of the spatial-angular domain) and to iteratively improve the angular resolution accuracy and reliability of the DoA estimation, while using the same data [55], [57].
As compared to the existing state-of-the-art literature, the following methodological advances are here present:

1. the exploitation, for the first time to best of the authors' knowledge, of the information on the *degree of reliability* obtained by the BCS to improve the efficacy of the bearing estimation;

2. the introduction of a "confidence level index", defined as a function of the reliability values, used to compute the angular regions in which to perform the DoA estimation at the next zooming step;

3. the implementation of a multi-scaling strategy aimed at quickly/slowly increasing the discretization resolution of the angular regions in case high/low confidence level values are obtained at the previous step.

4.2 The *BCS* Multi-Scaling Strategy

In Sect. 3.4.1, the problem in hand (3.8) is solved by $ST-BCS$ by maximizing the *a-posteriori* probability function of (3.11) in order to retrieve the sparsest solution of signal vector $\widehat{\mathbf{s}}_{ST-BCS}$ using the mean value as defined in (3.12). As $ST-BCS$ uses only a single snapshot data for reconstruction, the performance is not reliable and robust [78]. In order to improve the performance of $ST-BCS$, the noise variance $\boldsymbol{\sigma}^2_{BCS}$ of (3.12) is exploited as an extra degree of freedom.

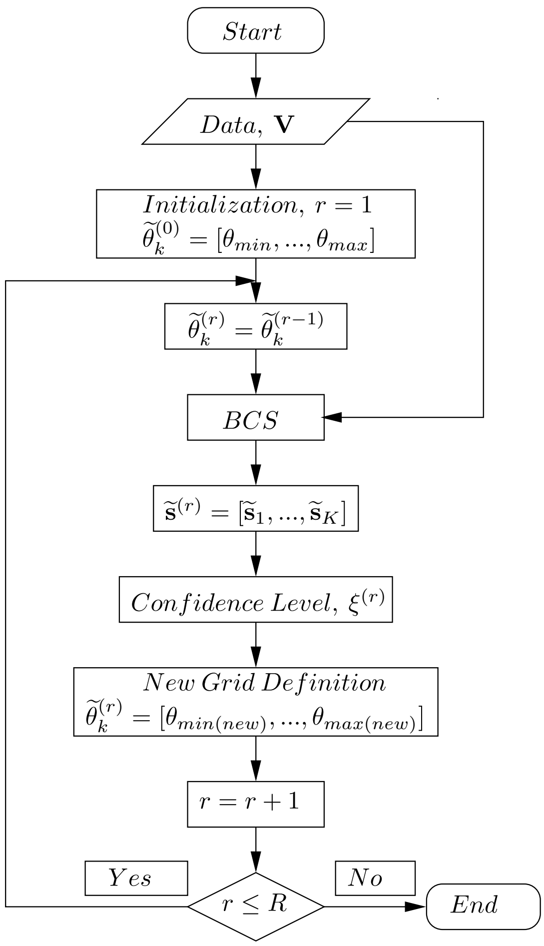

Figure 4.1: *Working Principle* - $IMSA-BCS$ flow chart.

The variance $\boldsymbol{\sigma}^2_{BCS}$ of the posterior probability function (3.11) is an index inversely proportional to the *degree-of-reliability* of the BCS-estimate of the actual signal vector $\widehat{\mathbf{s}}$ [70] (i.e., a small variance value $\sigma^2_{k,BCS}$ means a high probability of correct estimation of the corresponding signal coefficient $\hat{s}_k$, while larger values correspond to low probabilities/high-uncertainties of faithful signal detections). This information is exploited to improve the accuracy and the certainty of the

DoA retrieval process. Towards this end and for the first time to the best of the authors' knowledge, the BCS-based estimator is integrated with an iterative multi-scaling ($IMSA$) scheme. The flow chart of $IMSA-BCS$ method is shown in Fig. 4.1. More specifically, the $IMSA-BCS$ method works as follows (Fig. 4.2):

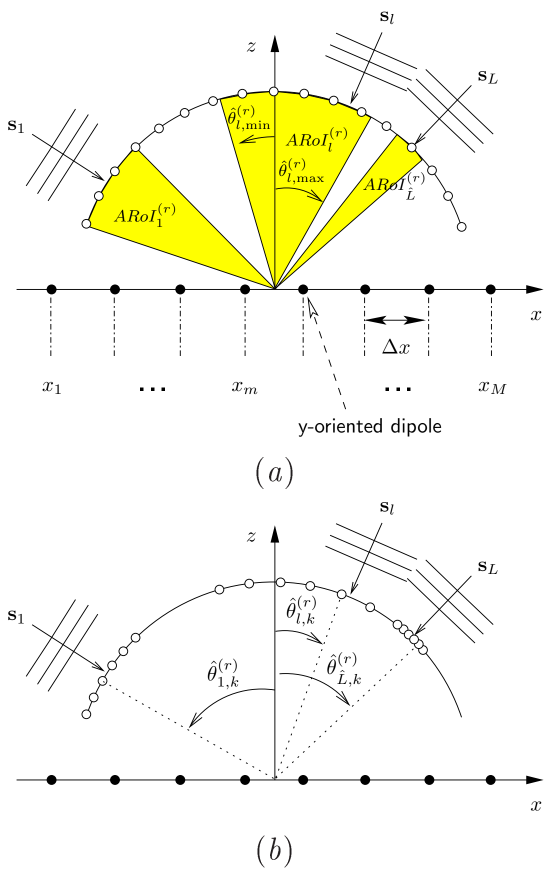

Figure 4.2: *BCS-based Approach* - Graphical sketches illustrating the $IMSA-BCS$ retrieval process: (a) discretization of the angular domain and $ARoI$s definition and (b) sampling grid refinement.

- **Step 0 - Angular Grid Initialization** $(r = 1)$**.** Discretize the angular region of interest ($ARoI$), $\theta \in \left[-\frac{\pi}{2}, \frac{\pi}{2}\right]$, in a uniform sampling grid, $\boldsymbol{\Gamma}^{(r)} = \left\{\hat{\theta}^{(r)}_k = -\frac{\pi}{2} + (k-1)\,\delta\theta^{(r)};\, k = 1, ..., K\right\}$, $\delta\theta^{(r)} = \frac{\pi}{K-1}$ being the angular step [Fig. 4.2(a)];
- **Step 1 - Bare** *BCS DoA* **Estimation** $(r = 1)$**.** Apply the BCS-estimator and estimate at the $r = 1$ resolution level the DoA, $\hat{\boldsymbol{\theta}}^{(r)}_{BCS} = \left\{\hat{\theta}^{(r)}_l : l = 1, ..., \hat{L}^{(r)}\right\}$, according to the "bare" BCS technique described above. Then, update the resolution index r $(r \leftarrow r + 1)$ and go to Step 2;

- **Step 2 -** $IMSA-BCS$ **Loop** ($r = 2, ..., R$)**.** Select the maximum number of zooming steps, R, and apply the following iterative zooming strategy:

  – **Step 2.1 - Confidence Level Computation.** Given the variances $\sigma^2_{l,BCS}\big|^{(r-1)}$, $l = 1, ..., \hat{L}^{(r-1)}$ associated to $\hat{\theta}_l^{(r-1)}$, $l = 1, ..., \hat{L}^{(r-1)}$, the normalized "confidence level index" of the estimated DoA is computed as

  $$\xi_l^{(r-1)} = \frac{\left(\sigma^2_{l,BCS}\big|^{(r-1)}\right)^{-1}}{\sum_{i=1}^{\hat{L}^{(r-1)}}\left(\sigma^2_{i,BCS}\big|^{(r-1)}\right)^{-1}},\ l = 1, ..., \hat{L}^{(r-1)}; \tag{4.1}$$

  – **Step 2.2 -** *ARoI***s Definition.** Set $\Omega^{(r)} = \frac{\pi}{2^{r-1}}$ as the maximum angular extension of the angular regions-of-interest (*ARoI*s), where the signals are supposed to impinge, at the r-th zooming step. For each l-th ($l = 1, ..., \hat{L}^{(r-1)}$) DoA estimated at the $(r-1)$-th step, associate an *ARoI* [Fig. 4.2(a)] of angular width

  $$ARoI_l^{(r)} = \left\{\theta\ :\ \hat{\theta}_l^{(r-1)} - \frac{\Omega_l^{(r)}}{2} \le \theta \le \hat{\theta}_l^{(r-1)} + \frac{\Omega_l^{(r)}}{2}\right\} \tag{4.2}$$

  where $\Omega_l^{(r)} = \frac{\Omega^{(r)}}{\xi_l^{(r-1)}}$;

  – **Step 2.3 - Sampling Grid Update.** Set $K^{(r)} = \left\lceil \frac{K}{\hat{L}^{(r-1)}} \right\rceil$, $\lceil\cdot\rceil$ being the ceiling function, and discretize each $ARoI_l^{(r)}$, $l = 1, ..., \hat{L}^{(r-1)}$ with a uniform grid of step $\delta\theta_l^{(r)} = \frac{\left(\hat{\theta}^{(r)}_{l,\max} - \hat{\theta}^{(r)}_{l,\min}\right)}{K^{(r)}-1}$ [Fig. 1(b)] such that the new angular samples are

  $$\hat{\theta}_{l,k}^{(r)} = \hat{\theta}_{l,\min}^{(r)} + (k-1)\,\delta\theta_l^{(r)},\ \ k = 1, ..., K^{(r)}. \tag{4.3}$$

  Accordingly, the updated sampling grid is composed by the union of the discretized *ARoI*s, i.e., $\mathbf{\Gamma}^{(r)} = \left\{\hat{\theta}_{l,k}^{(r)}\ :\ l = 1, .., \hat{L}^{(r-1)};\ k = 1, .., K^{(r)}\right\}$;

  – **Step 2.4 -** $IMSA-BCS$ DoA **Estimation.** Discretize $\hat{\mathbf{A}}^{(r)}$ and $\hat{\mathbf{s}}^{(r)}$ with reference to the sampling grid $\mathbf{\Gamma}^{(r)}$. Then, apply the *BCS*-estimator through (3.12) and the successive energy thresholding to give the r-th level estimate of the DoA, $\hat{\boldsymbol{\theta}}_{BCS}^{(r)} = \left\{\hat{\theta}_l^{(r)}\ :\ l = 1, ..., \hat{L}^{(r)}\right\}$. Successively, if $r < R$ then go Step 2.1, else go to Step 3;

- **Step 3 -** $IMSA-BCS$ **Output.** The DoA estimated at the end ($r = R$) of the multi-zooming process are assumed as the *IMSA-BCS* output: $\hat{\boldsymbol{\theta}}_{BCS}^{(R)} = \hat{\boldsymbol{\theta}}_{BCS} = \left\{\hat{\theta}_{l,BCS}\ :\ l = 1, ..., \hat{L}_{BCS}\right\}$.

It is worth noticing that, since the number of angular samples $K^{(r)}$ is kept fixed for each *ARoI*, the $IMSA-BCS$ enables a finer discretization (i.e., a faster zooming) in the *ARoI*s in which the *DoA* have been estimated at the previous step with higher probability, while a coarse grid (i.e., a slower zooming) is applied otherwise. This key-feature allows one to enhance the robustness of the *DoA*-estimation process and to avoid premature converge to angular regions where the presence of impinging signals is more uncertain.

4.3 Numerical Analysis

This section is devoted to the numerical analysis and validation of the $IMSA-BCS$ method. First, the behavior of the proposed approach is step-by-step illustrated with a representative example. Then, the performance of the $IMSA-BCS$ is extensively assessed versus the number and DoA of the signals, the signal-to-noise ratio (SNR) defined as

$$SNR = 10 \log \left[\frac{\sum_{m=1}^{M} |v_m|^2}{N\sigma_N^2} \right] \tag{4.4}$$

where σ_N^2 is the variance of the additive Gaussian noise, as well as the polarization mismatch between the incident waves and the receiving dipoles. In (4.4), the voltages V_m, $m = 1, ..., M$ are computed by assuming perfect polarization match (i.e., polarization loss factor $PLF = |\widehat{\mathbf{u}}_l \cdot \widehat{\mathbf{y}}|^2 = 1.0$ [90]) in order to maintain the same noise conditions whatever the PLF.

Finally, comparisons with state-of-the-art methods on representative benchmark examples are carried out. In all tests, the DoA estimation accuracy is evaluated in terms of the root-mean-square-error ($RMSE$), computed in degrees as [78]

$$RMSE^{(r)} = \begin{cases} \sqrt{\frac{\left\{\sum_{l=1}^{\hat{L}^{(r)}} \left|\theta_l - \hat{\theta}_l^{(r)}\right|^2 + \left|L - \hat{L}^{(r)}\right| (\Delta\theta_{max})^2\right\}}{L}} \\ if \;\; \hat{L}^{(r)} \leq L \\ \sqrt{\frac{\left\{\sum_{l=1}^{L} \left|\theta_l - \hat{\theta}_l^{(r)}\right|^2 + \sum_{j=L+1}^{\hat{L}^{(r)}} \left|\hat{\theta}_l^{(r)} - \overline{\theta}_j^{(r)}\right|^2\right\}}{L}} \\ if \;\; \hat{L}^{(r)} > L \end{cases} \tag{4.5}$$

$r = 1, ..., R$, $\Delta\theta_{max}$ being a penalty term equal to the maximum localization error (i.e., $\Delta\theta_{max} = 180\,[deg]$) when the number of impinging signals is underestimated, while $\overline{\theta}_j^{(r)} = \arg\left\{\min_{\phi_l,\, l\in[1,L]} \left| \theta_l - \hat{\theta}_l^{(r)} \right|\right\}$. In (5.15), the value $\hat{\theta}_l^{(r)}$ ($l = 1, ..., L$; $r = 1, ..., R$) corresponds to the DoA estimated at the r-th zooming step which is closest to the l-th ($l = 1, ..., L$) actual DoA. Moreover, the artifacts-filtering threshold (3.18) has been set to $\tau = 0.95$ as suggested in [78] and $G = 7$ basis functions are used for discretizing the currents of the dipoles in the MoM.

4.3.1 Method Validation

Let us consider a set of $L = 3$ binary phase-shift keying ($BPSK$) signals ($E_l^{inc} = \pm 1$) impinging on a linear array of $M = 10$ equally-spaced ($d = \frac{\lambda}{2}$) half-wavelength dipoles ($h = \frac{\lambda}{2}$). The measured voltages y_m, $m = 1, ..., M$ are corrupted by a noise level equivalent to a $SNR = 10\,dB$. When applying the *IMSA-BCS*, the angular range $\theta \in [-90; 90]$ $[deg]$ has been partitioned at the beginning ($r = 1$) with a uniform grid of $K = 37$ samples such that $\Delta\theta^{(1)} = 5\,[deg]$. For validation purposes, the more complex case of an off-grid configuration of the $L = 3$ signals has been considered. Accordingly, the DoA have been set to $\boldsymbol{\theta} = \{-22, -3, 8\}$ $[deg]$. Moreover, $PLF = 1.0$ is assumed.

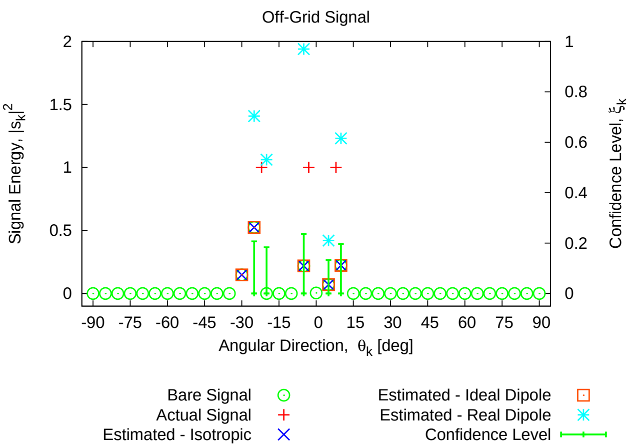

Figure 4.3: *Method Validation* ($M = 10$, $d = 0.5\lambda$; $L = 3$, $SNR = 10\,dB$; $K = 37$, $R = 1$) - Actual and estimated DoA and values of the confidence level for the case of off-grid signals impinging from the directions $\boldsymbol{\theta} = \{-22, -3, 8\}$ $[deg]$.

Figure 4.3 shows the *IMSA-BCS* estimates at the first step ($r = 1$) before (*Bare* - 4.3) and after (*Estimated - Real Dipole* - 4.3) the energy threshold (3.18). As it can be observed, the number of impinging signals is not correctly predicted, also after energy thresholding, and it turns out to be $\hat{L}^{(1)} = 5$. The signal localization error amounts to $RMSE^{(1)} = 3.16$ (Tab. 4.1 - $r = 1$). The results of the DoA estimation obtained by means of the same approach when considering an array of dipoles not affected by mutual coupling (*Estimated - Ideal Dipole* - 4.3) and an array of ideal isotropic sensors (*Estimated - Isotropic* - 4.3) are reported, as well. Although the ideality of these arrays, it is possible to observe that there is still an over-estimation of the number of signals and that the actual directions are not accurately retrieved.

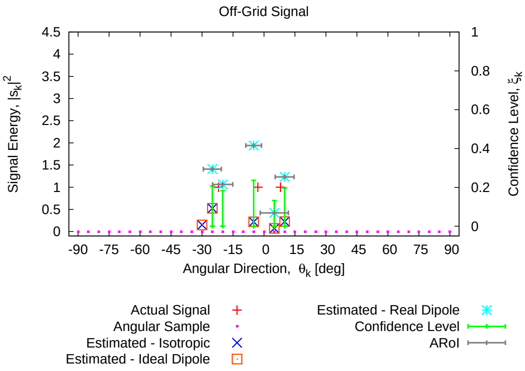

(a)

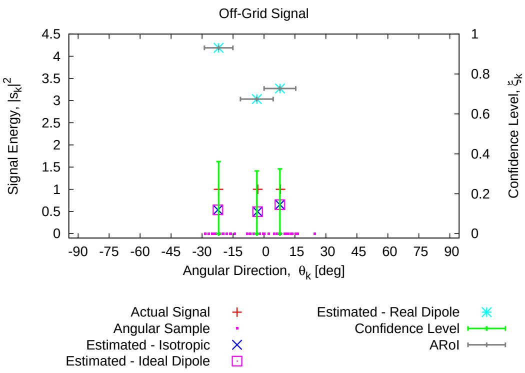

(b)

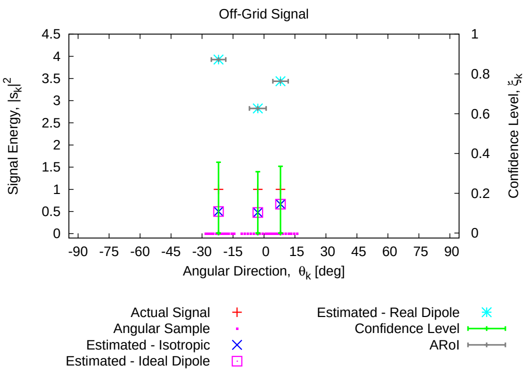

(c)

Figure 4.4: *Method Validation* ($M = 10$, $d = 0.5\lambda$; $L = 3$, $SNR = 10\,dB$; $K = 37$, $R = 3$) - Actual and estimated *DoA*, values of the confidence level, and *ARoI*s for the case of off-grid signals impinging from the directions ($\boldsymbol{\theta} = \{-22, -3, 8\}$ [deg]) at the (a) first $r = 1$, (b) second $r = 2$, and (c) third $r = R = 3$ multi-resolution step.

When applying the *IMSA* strategy, the angular resolution has been increased taking into account the degree of reliability (i.e., the confidence level, $\hat{\xi}_l^{(1)}$, $l =$

Table 4.1: *Method Validation* ($M = 10$, $d = 0.5\lambda$; $L = 3$, $SNR = 10\,dB$; $K = 37$, $R = 3$) - Actual and estimated DoA, total $ARoI$, and $RMSE$ value for the case of off-grid signals impinging from the directions $\boldsymbol{\theta} = \{-22,\ -3,\ 8\}$ $[deg]$.

r	*Angular Range*	*Estimated DoAs* : $\hat{\boldsymbol{\theta}}_{BCS}$
1	$180\,[deg]$	$\{-25,\ -20,\ -5,\ 5, 10\}$
2	$52.49\,[deg]$	$\{-21.97,\ -3.47,\ 7.72\}$
3	$40.92\,[deg]$	$\{-22,\ -3,\ 8\}$
r	*Confidence Level*	*RMSE*
1	$\{0.21,\ 0.18,\ 0.24,\ 0.13,\ 0.19\}$	3.16
2	$\{0.36,\ 0.31,\ 0.32\}$	0.32
3	$\{0.19,\ 0.08,\ 0.14\}$	0.00

$1, ..., \hat{L}^{(1)}$) of the estimates at the previous step, $r = 1$ (Tab. 4.1). The $ARoI_l^{(2)}$, $l = 1, ..., \hat{L}^{(1)}$ [Fig. 4.4(a)] and the sampling grid $\boldsymbol{\Gamma}^{(2)}$ [Fig. 4.4(b)] have been set according to (4.2) and (4.3). The result of the successive application of the BCS-based estimator, as shown in Fig. 4.4(b), corresponds to a significant reduction of the $RMSE$ from $RMSE^{(1)} = 3.16$ down to $RMSE^{(2)} = 0.32$ (Tab. 4.1). After another step, that is at the last step of the $IMSA$ process ($r = R = 3$), the unknown DoA of the impinging signals are faithfully predicted [Fig. 4.4(c); $RMSE^{(3)} = 0.0$ - Tab. 4.1]. The solutions achieved for the ideal array configurations are analogous and reported in Fig. 4.4, as well.

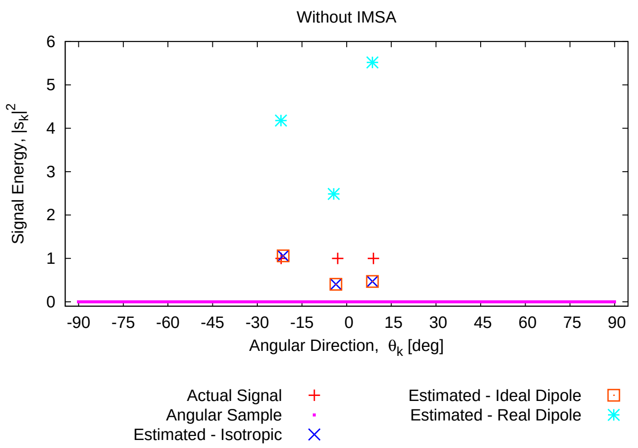

Figure 4.5: *Method Validation* ($M = 10$, $d = 0.5\lambda$; $L = 3$, $SNR = 10\,dB$; $R = 1$) - Actual and estimated DoA with single-snapshot approach of [78] with $K = 499$ equally-spaced angular samples ($\Delta\theta = \Delta\theta_{min} = 0.42\,[deg]$).

As a further comparative test, the solution in Fig. 4.4(c) has been compared with the one yielded by the single-resolution BCS-based approach when uniformly partitioning the angular domain with the finest resolution, $\Delta\theta_{min} \simeq 0.42\,[deg]$ ($K = 428$), of the *IMSA*-BCS at the convergence (i.e., $\Delta\phi_{min} \triangleq \min_{l=1,\ldots,\hat{L}^{(R)}} \Delta\phi_l^{(R)}$). The result in Fig. 4.5 presents a higher $RMSE$ value ($RMSE = 0.64$ vs. $RMSE^{(3)} = 0.0$) despite the denser angular grid ($K = 428$ vs. $K^{(3)} = 37$). Concerning the computational time, the DoA prediction in Fig. 4.5 has been carried out in $0.62\,[sec]$, while the $R = 3$ *IMSA* steps have been performed in $0.47\,[sec]$. In all cases, a standard laptop with $2.4\,GHz$ CPU and $2\,GB$ of RAM has been used.

4.3.2 Performance Analysis

In the next example, the performance of the $IMSA-BCS$ is assessed versus the number of impinging $BPSK$ signals. With reference to an $M = 20$ dipole array with $d = \frac{\lambda}{2}$ and $h = \frac{\lambda}{2}$, three different signal configurations with $L = \{2, 4, 6\}$ have been considered. More in detail, the actual DoA have been chosen as follows: $\boldsymbol{\theta} = \{2.5, 22.5\}$ $[deg]$ $(L = 2)$, $\boldsymbol{\theta} = \{-32.5, 2.5, 22.5, 47.5\}$ $[deg]$ $(L = 4)$, and $\boldsymbol{\theta} = \{-57.5, -32.5, 2.5, 22.5, 47.5, 62.5\}$ $[deg]$ $(L = 6)$.
A set of $T = 100$ simulations, with a different noise realization with $SNR = 20\,dB$ for each trial, has been run to draw statistically reliable outcomes. Concerning the *IMSA-BCS* parameters, the *ARoI*s have been discretized at each r-th step in $K = 37$ samples and the zooming process has been stopped after $R = 5$ iterations. The behaviours of the $RMSE$ values for $PLF = 1.0$ are shown in Fig. 4.6 (first collumn) and the corresponding statistics are reported in Tab. 4.2. As expected, the advantages of the multi-zooming strategy are non-negligible. Indeed, the $RMSE^{(r)}$ monotonically decreases with the iteration index r whatever L (Fig. 4.6) and its average value (Tab. 4.2) reduces - also in the most complex case $(L = 6)$ - of at least 13 times between the first $(r = 1)$ and the last $(r = R = 5)$ zooming step (Tab. 4.2) with a final error equal to $RMSE_{avg}^{(5)}\Big|_{L=6} = 0.23$. Moreover, the worst result at the convergence step corresponds to $RMSE_{max}^{(5)}\Big|_{L=6} = 0.32$.

Table 4.2: *Performance Analysis* $(M = 20,\ d = 0.5\lambda;\ L = \{2, 4, 6\},\ SNR = 20\,dB;\ K = 37,\ R = 5)$ - Statistics of the $RMSE$ values among a set of $T = 100$ realizations of the random noise generation process.

L	2				4				6			
r	min	max	avg	$s-dev$	min	max	avg	$s-dev$	min	max	avg	$s-dev$
1	3.54	3.56	3.54	0.05	3.31	3.54	3.49	0.09	2.89	3.39	3.16	0.13
2	0.16	2.46	0.63	0.66	0.41	1.73	1.16	0.47	0.39	1.20	0.83	0.23
3	0.16	0.54	0.36	0.13	0.13	0.63	0.36	0.13	0.32	0.69	0.47	0.13
4	0.10	0.44	0.28	0.13	0.12	0.33	0.22	0.07	0.19	0.43	0.29	0.07
5	0.09	0.22	0.16	0.04	0.12	0.24	0.18	0.04	0.16	0.32	0.23	0.04

As a representative result, the DoA estimated at each step of the $IMSA-BCS$ for the worst solution among the $T = 100$ simulations with $L = 6$ signals are shown in Fig. 4.7. Thanks to the zooming of the $ARoIs$ around the actual DoA, as shown by the samples of the angular grid in Fig. 4.7, the number of signals, over-estimated at the first step $(\hat{L}^{(1)} = 10)$, is correctly retrieved at the last step $(\hat{L}^{(5)} = \hat{L}_{BCS} = 6)$. Moreover, the proposed approach provides a precise prediction of the DoA $(RMSE_{max}^{(5)}\Big|_{L=6} = 0.32)$.

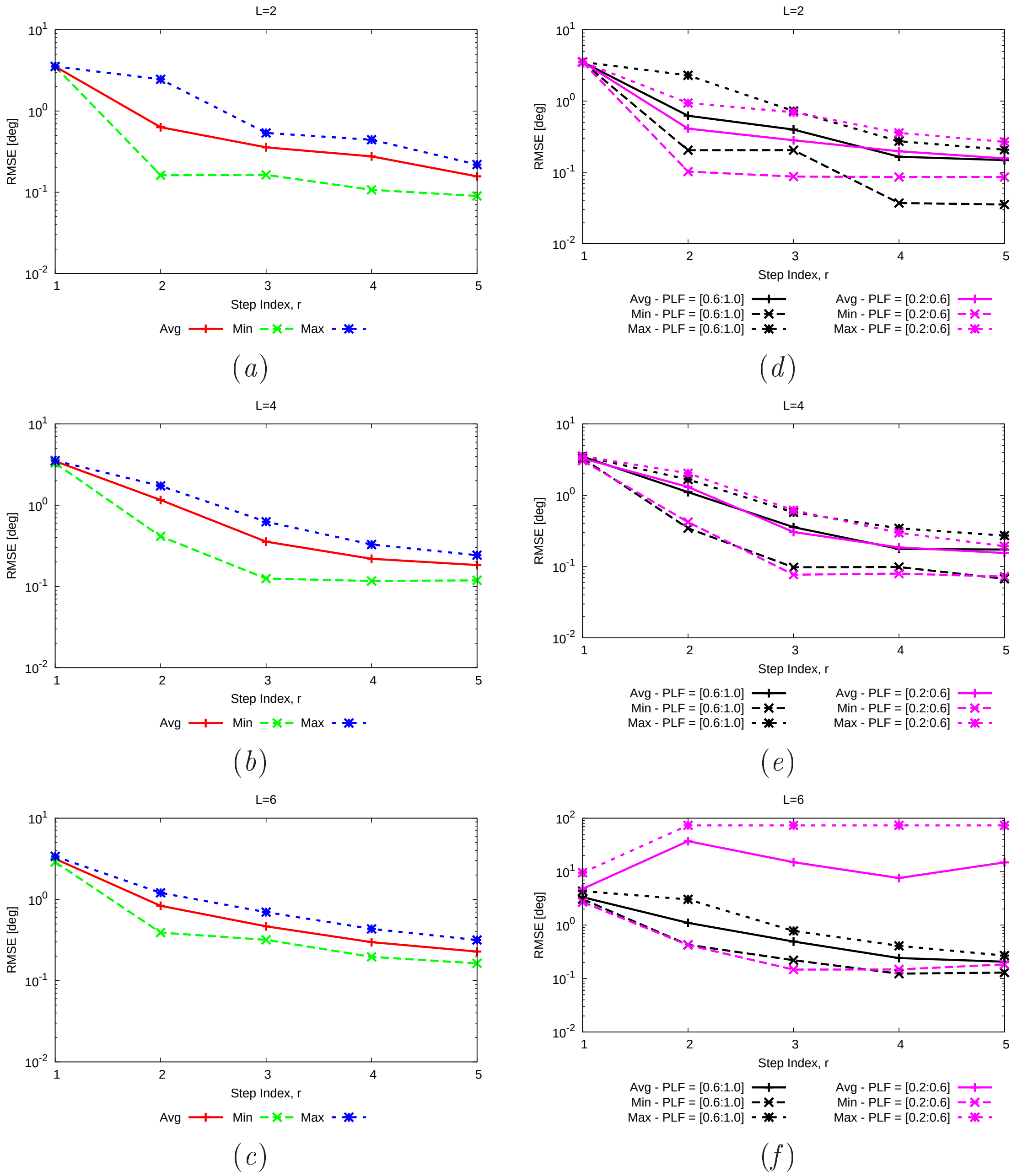

Figure 4.6: *Performance Analysis* ($M = 20$, $d = 0.5\lambda$; $L = \{2, 4, 6\}$, $SNR = 20\,dB$; $K = 37$, $R = 5$) - Best, worst, and average $RMSE$ values among $T = 100$ simulations with $(a)(d)$ $L = 2$, $(b)(e)$ $L = 4$, and $(c)(f)$ $L = 6$ signals, $(a)(b)(c)$ without and $(d)(e)(f)$ with polarization loss.

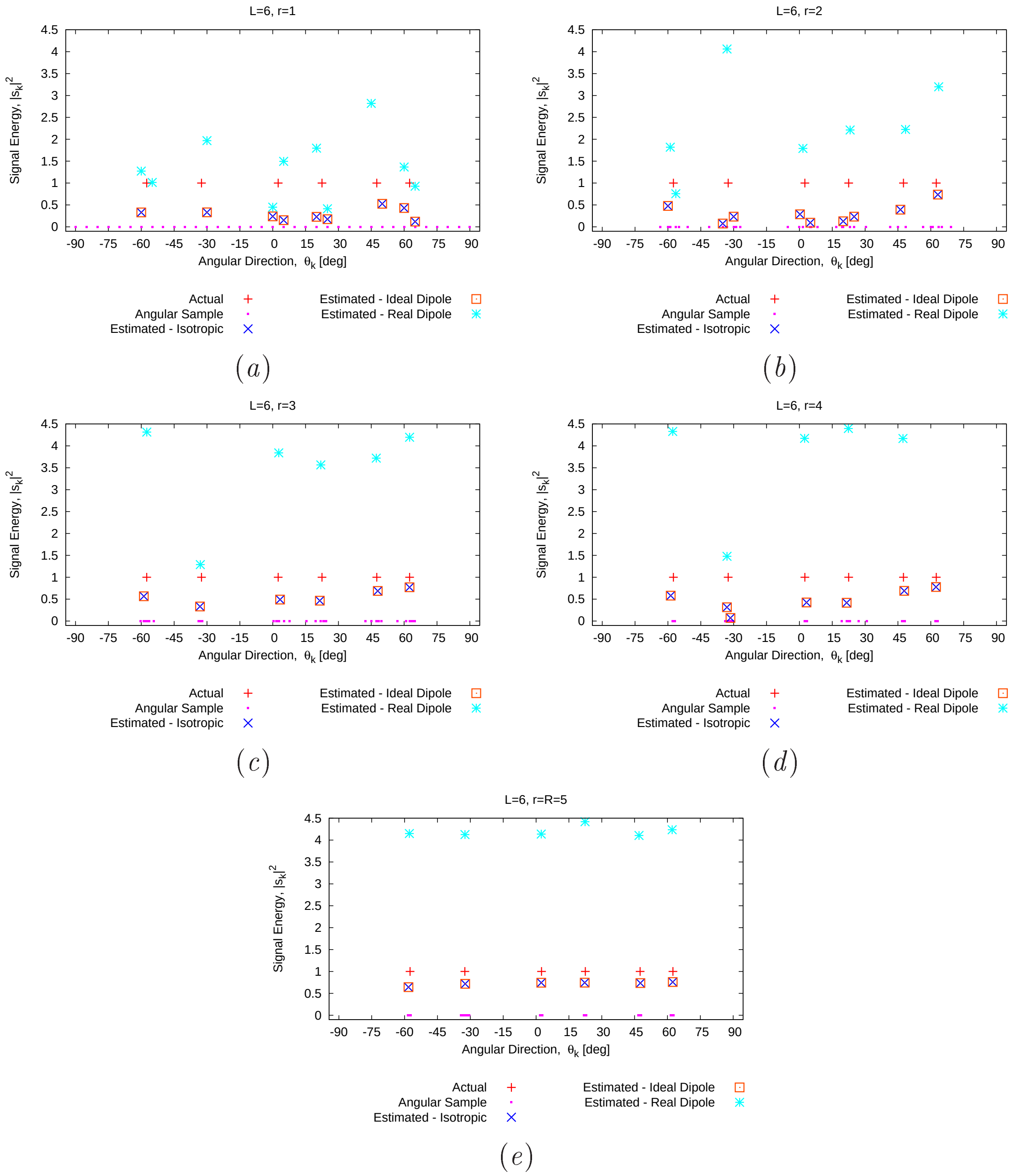

Figure 4.7: *Performance Analysis* ($M = 20$, $d = 0.5\lambda$; $L = 6$, $SNR = 20\,dB$; $K = 37$, $R = 5$) - Actual/estimated *DoA* at the multi-resolution step: (a) $r = 1$, (b) $r = 2$, (c) $r = 3$, (d) $r = 4$, and (e) $r = R = 5$ when $\boldsymbol{\theta} = \{-57.5, -32.5, 2.5, 22.5, 47.5, 62.5\}$ $[deg]$.

Further analyses are aimed at evaluating the impact of the polarization mismatch between the incident waves and the receiving dipoles. Accordingly, two statistical analyses have been carried out when considering $PLF \in [0.6 : 1.0]$

and $PLF \in [0.2 : 0.6]$. The same signal and noise configurations of the previous example have been taken into account. Again, the behavior of the maximum, minimum, and average $RMSE$ values are shown in Fig. 4.6 (second line). Accurate estimations ($RMSE_{max}^{(5)}\Big|_{L=6} < 0.37$) have been achieved for limited polarization loss (i.e., $PLF \geq 0.6$). The proposed $IMSA - BCS$ also allows to obtain reliable results for $PLF \in [0.2 : 0.6]$ and $L = 2$ ($RMSE_{max}^{(5)}\Big|_{L=2} < 0.27$) and $L = 4$ ($RMSE_{max}^{(5)}\Big|_{L=4} < 0.39$). Differently, higher average $RMSE$ values have been achieved for $L = 6$ as shown in Fig. 4.6(f).

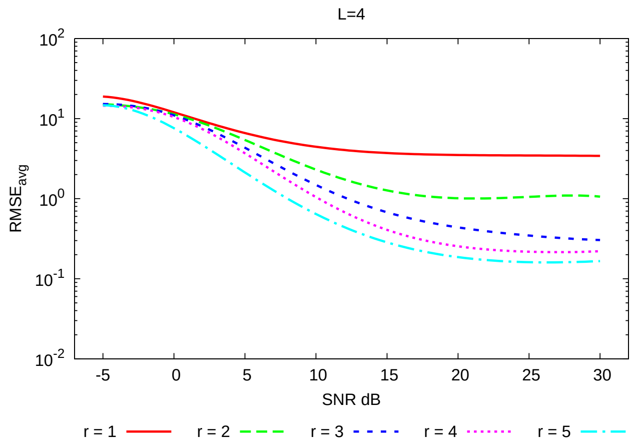

Figure 4.8: *Performance Analysis* ($M = 20$, $d = 0.5\lambda$; $L = 4$, $SNR \in [-5 : 30]\ dB$; $K = 37$, $R \in [1 : 5]$) - Average $RMSE$ values among $T = 100$ simulations versus SNR for different values of R.

The analysis of the impact of the measurement noise (i.e., SNR levels) and the number of zooming steps, R, has been carried out, as well. Figure 4.8 gives the average $RMSE$ when considering $L = 4$ $BPSK$ signals and $PLF \in [0.6 : 1.0]$ versus R and for different values of the SNR. As it can be observed, the multi-resolution process does not provide significant advantages in heavy noisy conditions ($SNR \leq 0\,dB$) because of the low reliability of the single-snapshot data. Differently, the average $RMSE$ quickly decreases with the zooming steps for higher SNRs.

4.3.3 Comparative Assessment

In order to demonstrate the validity of the *IMSA-BCS* approach, two recently proposed methods [78], [94], not requiring any data pre-processing before the DoA prediction, and two well-established state-of-the-art approaches, namely the $ROOT-MUSIC$ [31] and $ESPRIT$ [39] that need as input the covariance matrix, have been taken into account for a final comparative assessment. Towards this aim, the same hypotheses considered in [78], [94] (i.e., use of linear arrays of ideal isotropic sensors without mutual-coupling) have been taken into account. More specifically, the first benchmark [78] considers an $M = 20$-element $d = 0.5\lambda$-spaced array in an electromagnetic scenario characterized by a noise level of $SNR = 10\,dB$ and $L = 4$ signals impinging from the angular directions $\boldsymbol{\phi} = \{-89, -71, -50, -41\}$ $[deg]$. The following setup has been used when running the $IMSA-BCS$ code: $K = 37$ and $R = 5$. In [78], $K = 181$ samples has been chosen that implies an on-grid case (i.e., the actual DoA belong to the set of angular grid samples).

Table 4.3: *Comparative Assessment* (Benchmarks [78], $ROOT-MUSIC$ [31], $ESPRIT$ [39], and [94]) - $RMSE$ values.

Methods	r	*Test Case 1* [78]	*Test Case 2* [94]
IMSA-BCS	1	67.20	73.50
	2	4.78	73.49
	3	3.66	1.26
	4	2.65	1.13
	5	2.44	0.82
ST-BCS	1	58.87	73.53
*ST-BCS**	1	4.02	28.28
[31]	1	3.00	8.04
[39]	1	3.69	7.54
[94]	1	-	5.67
MT-BCS	1	0.50	0.41
*MT-BCS**	1	0.08	0.24

Figure 4.9 shows the DoA estimated by the proposed approach and by the $ST-BCS$ (a single-snapshot technique) and the $MT-BCS$ (a multiple-snapshots technique) methods presented in [78]. For completeness, the corresponding $RMSE$ values are given in Tab. 4.3. As it can be observed from the plots in Fig. 4.9 as well as inferred from the error values in Tab. 4.3, the $ST-BCS$ and the first step ($r = 1$) of the $IMSA-BCS$ do not provide accurate predictions. Thanks to the zooming, the $IMSA-BCS$ is instead able to drastically reduce the estimation error by more than 14 times after one step

($r = 2$) and to yield a final error at $r = R = 5$ equal to $RMSE^{(5)} = 2.44$. This result is more than 24 times better than the $ST-BCS$ one. Moreover, it is better than the estimations of the $ROOT-MUSIC$ ($RMSE_{ROOT-MUSIC} = 3.00$) and $ESPRIT$ ($RMSE_{ESPRIT} = 3.69$) and much closer to the $MT-BCS$ prediction ($RMSE = 0.50$) albeit these latter approaches exploit 25 consecutive acquisitions. It is also important to point out that the DoA obtained with $ROOT-MUSIC$ and $ESPRIT$ are plotted in Fig. 4.9 with vertical lines since these methods do not provide any estimation of the signals amplitude and/or phase unlike CS-based approaches.

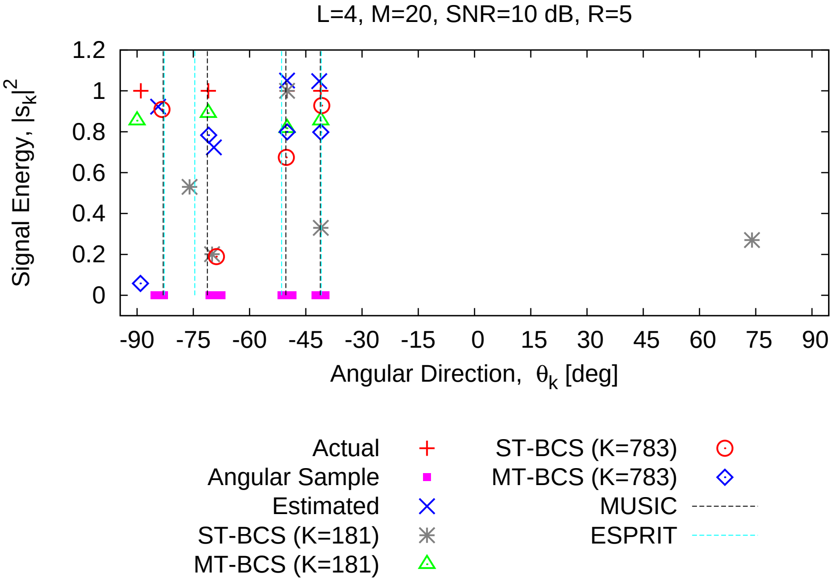

Figure 4.9: *Comparative Assessment* ($M = 20$, $d = 0.5\lambda$; $L = 4$, $SNR = 10\,dB$; $K = 37$, $R = 5$) - Actual and estimated DoA predicted by single ($IMSA-BCS$ and $ST-BCS$ [78]) and multiple snapshots ($MT-BCS$ [78], $ROOT-MUSIC$ [31], and $ESPRIT$ [39]) methods when $\boldsymbol{\theta} = \{-89, -71, -50, -41\}$ $[deg]$.

For completeness, the performance of the $ST-BCS$ (i.e., the single-snapshot single-step BCS method) has been also evaluated when adopting a uniform grid ($K = 783$) with an angular resolution equal to that reached by the $IMSA-BCS$ at the last zoom (i.e., $\delta\phi_{min} \simeq 0.23\,[deg]$). Despite the accuracy improvement of this oversampled version (denoted by $ST-BCS*$ in the following) as compared to the original one with $K = 181$ ($\frac{RMSE_{ST-BCS}}{RMSE_{ST-BCS*}} \approx 14.6$) at the cost of a greater computational cost ($K = 783$ vs. $K = 181$), its accuracy ($RMSE_{ST-BCS*} = 4.02$) is still worse than that of the $IMSA-BCS$ method ($RMSE^{(5)} = 2.44$) as indicated in Tab. 4.3 and pictorially highlighted in Fig. . 4.9. On the other hand and as expected, the exploitation of the multi-snapshots information of the $MT-BCS$ together with the angular overgridding ($MT-BCS*$) guarantees

a close-to-ideal result ($RMSE = 0.08$).
The second comparison is concerned with the test case reported in [94] and characterized by the following descriptive parameters: $M = 10$, $d = 0.5\lambda$, $L = 6$ ($\boldsymbol{\theta} = \{-78, -17, 7, 18, 32, 65\}$ $[deg]$), $SNR = 10\,dB$, and $K = 23$. Analogously to the $MT-BCS$ [78], the method in [94] used multiple snapshots and the data were acquired at 10 consecutive time instants.
Figure 4.10 shows the results predicted by the single and multiple-snapshots methods and the values of the localization index are given in Tab. 4.3. As it can be noticed and also expected, the $RMSE$ at the first zooming steps of the $IMSA-BCS$ is not satisfactory. Then, the estimation accuracy highly improves through the focusing process until the convergence value of $RMSE^{(5)} = 0.82$, that is almost 7 times better than that from the multi-snapshots technique in [94]. To complete the comparative analysis, the unknown DoA have been also predicted with the $ST-BCS$ and the $MT-BCS$ [78] when considering the same number of angular samples of ($K = 181$) or the uniform oversampling with the angular step $\delta\phi_{min} \simeq 0.27\,[deg]$ ($K = 671$) obtained at the convergence iteration of the $IMSA-BCS$. Moreover, the $ROOT-MUSIC$ and $ESPRIT$ estimators have been used, as well.

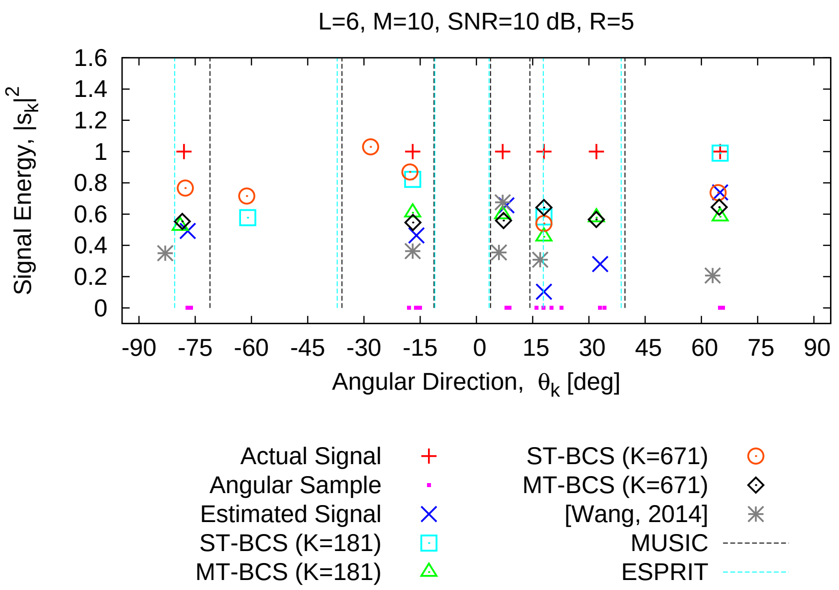

Figure 4.10: *Comparative Assessment* ($M = 10$, $d = 0.5\lambda$; $L = 6$, $SNR = 10\,dB$; $K = 23$, $R = 5$) - Actual and estimated DoA retrieved by single ($IMSA-BCS$ and $ST-BCS$ [78]) and multiple snapshots ($MT-BCS$ [78], $ROOT-MUSIC$ [31], $ESPRIT$ [39], and [94]-method) methods when $\boldsymbol{\theta} = \{-78, -17, 7, 18, 32, 65\}$ $[deg]$.

The $RMSE$ values in Tab. 4.3 indicate that, in both cases, the $ST-BCS$

method provides unsatisfactory results ($RMSE > 28.28$) and worse ($\frac{RMSE_{ST-BCS}}{RMSE_{IMSA-BCS}} \approx 90$ and $\frac{RMSE_{ST-BCS*}}{RMSE_{IMSA-BCS}} \approx 34$) than the $MT-BCS$ ($RMSE_{MT-BCS} = 0.41$ and $RMSE_{MT-BCS*} = 0.24$) that turns out to be the most accurate predictor (Tab. 4.3 - Fig. 4.10). As for the $MT-BCS$, it is worth reminding that it needs 10 snapshots, while the $IMSA-BCS$ provides similar accuracies ($\frac{RMSE_{MT-BCS}}{RMSE_{IMSA-BCS}} \approx 0.5$ and $\frac{RMSE_{MT-BCS*}}{RMSE_{IMSA-BCS}} \approx 0.3$) but with a single time acquisition. Differently, the performances of $ROOT-MUSIC$ ($RMSE_{ROOT-MUSIC} = 8.04$) and $ESPRIT$ ($RMSE_{ESPRIT} = 7.54$) are not satisfactory and worse than that achieved in the previous example because of the smaller number of available snapshots for computing the covariance matrix and the larger number of signals. Concerning the computational time of the BCS-based DoA estimations once the data are available for processing (i.e., after waiting 10 time instants for the $MT-BCS$), the $ST-BCS$ and $MT-BCS$ [78] required $0.38\,[sec]$ ($K = 181$), $0.69\,[sec]$ ($K = 671$) and $0.48\,[sec]$ ($K = 181$), $0.86\,[sec]$ ($K = 671$), respectively. Differently, the $IMSA-BCS$ ended in $0.59\,[sec]$.

Chapter 5

Performance Improvement of MT-BCS

In this Chapter, the performance of state-of-the-art $MT-BCS$ method has been improved significantly with the proposed multi-frequency BCS ($MF-BCS$) strategy, where the inherent properties (e.g., frequencies) of signals have been exploited in order to correlate the BCS solutions over different frequency samples. By exploiting frequencies as extra degrees-of-freedom, two methods have been proposed namely $MFSS-BCS$ (multi-frequency single-snapshot BCS) and $MFMS-BCS$ (multi-frequency multi-snapshots BCS). The $MFSS-BCS$ is developed for real-time DoA estimator while $MFMS-BCS$ is for improve the robustness of the estimation. In addition, the main outcome of this work is published in [29, 82, 83]

5.1 Introduction

Several methods for wide band $DoAs$ estimation have been proposed in the state-of-the-art literature. Notably, most of them are the customized version extended from the narrow band estimators, exploiting the decomposition of a wide band signal into multiple frequency components (i.e., frequency bins) and then apply aforementioned narrow band DoAs estimator either separately or jointly. Based on the separate or joint processing of frequency bins, the wide band DoA estimation techniques are broadly classified into two groups, namely incoherent and coherent estimation.

In incoherent method, the frequency bins are processed independently and then average the estimated $DoAs$ over all the bins [95, 96]. The implementation of incoherent processing is simple and provides good estimation in case of high $SNRs$ and widely spaced $DoAs$. The averaging over all independent solutions worsens the performance of estimation for closely spaced $DoAs$. The performance of incoherent method is significantly improved with $TOPS$ [97] by integrating the information for all frequency bins before estimating the $DoAs$. Although it does not process the bins independently, it is essentially an incoherent method despite disagreements among researchers.

On the other hand, the coherent processing aligns signal subspaces among all frequency bins by a transformation of the co-variance matrices that are associated with each bin. Therefore, the signal and noise subspaces becomes coherent and then one can apply subspace based estimators in the composite co-variance matrix. Based on the choice of alignment strategies, many coherent estimators have been proposed in the literature. Some of them are the coherent signal subspace method $CSSM$ [98], focusing matrices for $CSSM$ [98, 99, 100], robust auto-focusing [101], extended $ESPRIT$ [102], maximum-likelihood (ML) [104], and weighted average of signal subspaces $WAVES$ [105]. The overall performance of the coherence estimators is strongly depend on the focusing matrices. Although $TOPS$ [97], robust auto-focusing [101], and interpolated virtual array [103] are claimed to be the superior, they all share the same bottleneck.

Sparse processing [56]-[62] for signal reconstructions has received great attention since last two decades. In this framework, strategies based on the compressive sensing (CS) theory [59]-[61] have recently been introduces thanks to their effectiveness, flexibility, and computational efficiency to deal with complex engineering problems in electromagnetic [63]-[68] including antenna array synthesis [69]-[70] and imaging [71]-[75].

The BCS-based strategies have been effectively applied for $DoAs$ estimation for different purposes [78]-[84]. In this chapter, frequencies of the signal has been considered as an extra degree-of-freedom and two strategies are proposed namely $MFSS-BCS$ [82] and $MFMS-BCS$ [83].

5.2 Wideband DoA Model

Let us assume a receiving antenna system consists of a linear antenna array of M elements oriented along x-axis with the inter-element spacing of d and operates in the frequency range of $[f_{min} : f_{max}]$. The system is assumed to collect the data with respect to N samples at frequencies, $f_n = f_{min} + \nabla f \left(2n - 1\right)/N$, $n = 1, ..., N$, where $\nabla f = (f_{max} - f_{min})/2$. According to [2], the measured voltages at the terminal of the array at any instant of time t are generally expressed as

$$v\left(t\right) = \int_{f_{min}}^{f_{max}} V_m\left(f_n\right) e^{j2\pi(f_n - f_c)} df_n, \quad m = 1, ..., M, \quad n = 1, ..., N \tag{5.1}$$

where f_n and f_c are the $n-$th frequency and the center frequency respectively, and $V_m\left(f_n\right)$ is the received voltages as a function of frequencies and the locations of the array elements. In addition, the strength of the received voltages $V_m\left(f_n\right)$ are subject to the noise, polarization mismatch and array effective length as well.

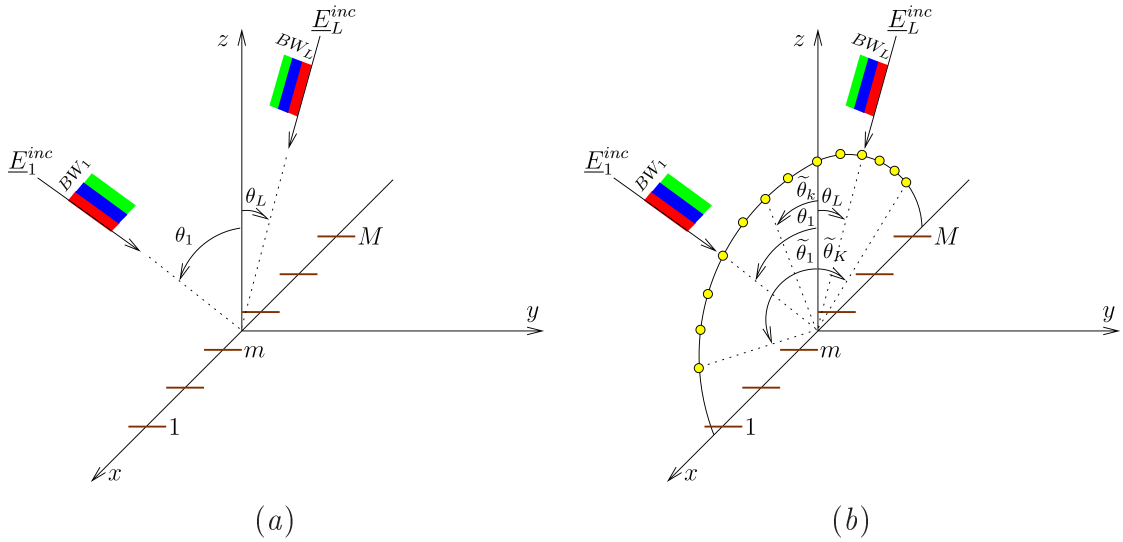

Figure 5.1: *MF−BCS-based Approach* - (a) reference scenario (b) discretization of the angular domain.

Therefore, for a set of $L\left(f_n\right)$ electromagnetic plane waves characterized by the bandwidth of $\mathbf{BW}_l$, $l = 1, ..., L$ (Fig. 5.1) coming from unknown bearings θ_l , $l = 1, ..., L\left(f_n\right)$, the well accepted model for the received voltages at time t_w is as follows

$$V_m\left(f_n, t_w\right) = \sum_{l=1}^{L} s_l\left(f_n\right) \hat{\boldsymbol{y}}.\boldsymbol{\mathcal{H}} e^{j\frac{2\pi f_n}{c} x_m \sin\theta_l} + \eta_m\left(f_n, t_w\right), \quad m = 1, ..., M, \quad n = 1, ..., N \tag{5.2}$$

where $\boldsymbol{\mathcal{H}}$ is the antenna effective length, $\eta_m(f_n, t_w)$ is the additive white Gaussian noise having zero mean and variance equal to the noise power, x_m is the sensors positions, and $s(f_n)$ is magnitude of the signal which creates the electromagnetic plane wave.
The $y - polarized$ electromagnetic plane wave is modeled as

$$\mathbf{s}(\boldsymbol{r}) = s(f_n)\, e^{j2\frac{2\pi f_n}{c}(x\sin\theta + z\cos\theta)}\hat{\boldsymbol{y}}. \tag{5.3}$$

For simplicity, equation (5.2) can be written as matrix form as follows

$$\mathbf{V}(f_n, t_w) \; = \mathbf{A}(f_n)\,\mathbf{s}(f_n) + \boldsymbol{\eta}(f_n, t_w), \quad n = 1, ..., N \tag{5.4}$$

where for each snapshot t_w, $\mathbf{V}(f_n, t_w) \in \mathbb{C}^{M\times 1}$ is the open circuit voltages measured at f_n and $\boldsymbol{\eta}(f_n, t_w) \in \mathbb{C}^{M\times 1}$ are the additive white Gaussian noises generated at f_n. In addition, $\mathbf{s}(f_n) \in \mathbb{C}^{L\times 1}$ are the original incoming signals considered at f_n and $\mathbf{A}(f_n) \in \mathbb{C}^{M\times L}$ is the time independent steering matrix at f_n. For M elements and L signals, the steering matrix at frequency f_n is defined as

$$\mathbf{A}(f_n) = \begin{bmatrix} e^{j\frac{2\pi f_n}{c}x_1\sin\theta_1} & \cdots & e^{j\frac{2\pi f_n}{c}x_1\sin\theta_L} \\ \vdots & \ddots & \vdots \\ e^{j\frac{2\pi f_n}{c}x_M\sin\theta_1} & \cdots & e^{j\frac{2\pi f_n}{c}x_M\sin\theta_L} \end{bmatrix}. \tag{5.5}$$

The objective is to find out the angular directions θ_l, $l = 1, ..., L$ from the measured voltages in (5.2) which is clearly a non-linear function.

5.3 Problem Formulation in BCS Framework

In order to determine the actual directions θ_l, $l = 1, ..., L$, the angular domain $\theta \in [-90 : 90]$deg is discretized into a large set of $K \gg L$ (Fig. 5.1) candidate angular directions. Accordingly, the steering matrix in (5.5) becomes a matrix of complex $[M \times K]$ entries (i.e., $\boldsymbol{A}(f_n) \in \mathbb{C}^{M\times K}$) at f_n as

$$\boldsymbol{A}(f_n) = \begin{bmatrix} e^{j\frac{2\pi f_n}{c}x_1\sin\theta_1} & \cdots & e^{j\frac{2\pi f_n}{c}x_1\sin\theta_k} & \cdots & e^{j\frac{2\pi f_n}{c}x_1\sin\theta_K} \\ \vdots & & \vdots & & \vdots \\ e^{j\frac{2\pi f_n}{c}x_m\sin\theta_1} & \cdots & e^{j\frac{2\pi f_n}{c}x_m\sin\theta_k} & \cdots & e^{j\frac{2\pi f_n}{c}x_m\sin\theta_K} \\ \vdots & & \vdots & & \vdots \\ e^{j\frac{2\pi f_n}{c}x_M\sin\theta_1} & \cdots & e^{j\frac{2\pi f_n}{c}x_M\sin\theta_k} & \cdots & e^{j\frac{2\pi f_n}{c}x_M\sin\theta_K} \end{bmatrix}. \tag{5.6}$$

Therefore, the problem in hand is now linear with respect to unknown candidate signal vector $\hat{\mathbf{s}}(f_n) \in \mathbb{C}^{K\times 1}$ which is also sparse as $K \gg L$.

According to [78], the BCS looks for the solution of the sparse signal vector $\hat{\mathbf{s}}\left(f_n\right)$ instead of directly estimating the directions. The $MT-BCS$ approach is proposed in the state-of-art literature in order to increase robustness against noise. In general, for example in [78], $MT-BCS$ is used to correlate the solutions among different snapshots. Differently, the $MT-BCS$ used in this approach to correlate among different time and frequency samples. Based on this time-frequency configuration, the BCS for wideband DoAs estimation is categorized into two methods: (I) multi-frequency single-snapshot BCS ($MFSS-BCS$) and (II) multi-frequency multi-snapshots BCS ($MFMS-BCS$).

5.3.1 Multi-Frequency Single-Snapshots BCS ($MFSS-BCS$)

This technique considers single snapshot ($W = 1$) data. Therefore, it only correlates the solutions among different frequencies. Following the guideline of [78], the unknown signal vector $\hat{\mathbf{s}}_{MFSS-BCS}$ is determined as follows

$$\hat{\mathbf{s}}_{MFSS-BCS} = \frac{1}{N}\sum_{n=1}^{N} \arg\left\{\max_{\hat{\mathbf{s}}(f_n)} \Pr\left[\left(\hat{\mathbf{s}}\left(f_n\right), \mathbf{p}\right) \mid \mathbf{V}\left(f_n\right)\right]\right\}, \quad n = 1, ..., N \tag{5.7}$$

where $\hat{\mathbf{s}}\left(f_n\right)$, $n = 1, ..., N$, is statistically correlated among different frequency samples through a proper optimization of hyper parameter vector $\mathbf{p}$ which is shared among solutions. The optimal value of $\mathbf{p}$ is obtained through RVM [56]

$$\boldsymbol{\mathcal{L}}_{MFSS-BCS}\left(\mathbf{p}\right) = -\frac{1}{2}\sum_{n=1}^{N}\left\{\log\left(\left|\mathbf{C}\right|\right) + \left(K + 2\varphi_1\right)\log\left[\mathbf{V}\left(f_n\right)^{\mathbf{T}}\mathbf{C}\mathbf{V}\left(f_n\right) + 2\varphi_2\right]\right\}, \tag{5.8}$$

where $\mathbf{C} = I + \hat{\mathbf{A}}\left(f_n\right) diag\left(\mathbf{p}\right)^{-1}\hat{\mathbf{A}}\left(f_n\right)^T$ and φ_1 and φ_2 are user-defined parameters [61]. Finally, the $MFSS - BCS$ solution turns out to be

$$\hat{\mathbf{s}} = \frac{1}{N}\sum_{n=1}^{N}\left\{\left[\hat{\mathbf{A}}\left(f_n\right)^T\hat{\mathbf{A}}\left(f_n\right) + diag\left(\mathbf{p}\right)\right]^{-1}\hat{\mathbf{A}}\left(f_n\right)\mathbf{V}\left(f_n\right)\right\}, \quad n = 1, ..., N \ . \tag{5.9}$$

In order to estimate the bandwidth of the impinging signals, the (5.9) can also be written over the N independent frequency samples. The solution at f_n is obtained as follows :

$$\hat{\mathbf{s}}_{MFSS-BCS}\ \left(f_n\right) = \left[\hat{\mathbf{A}}\left(f_n\right)^T\hat{\mathbf{A}}\left(f_n\right) + diag\left(\mathbf{p}\right)\right]^{-1}\hat{\mathbf{A}}\left(f_n\right)\mathbf{V}\left(f_n\right), \quad n = 1, ..., N \ . \tag{5.10}$$

5.3.2 Multi-Frequency Multi-Snapshots BCS ($MFMS{-}BCS$)

This technique considers multiple snapshot ($w = 1, ..., W$) data. Therefore, it correlates the solutions among different time and frequency samples as shown in Fig 5.2.

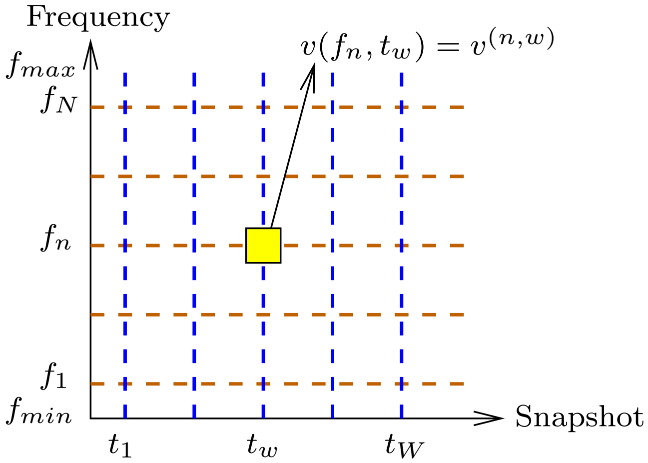

Figure 5.2: *$MFMS - BCS$-based Approach* - representation of time-frequency data.

Similar to the Sect. 5.3.1, the unknown signal vector $\hat{\mathbf{s}}_{MFMS-BCS}$ is determined by:

$$\widehat{\mathbf{s}}_{MFMS-BCS} = \frac{1}{WN}\sum_{w=1}^{W}\sum_{n=1}^{N}\left\{\arg\left[\max_{\widehat{\mathbf{s}}^{(n,w)}}\mathcal{P}r\left(\left[\widehat{\mathbf{s}}^{(n,w)},\,\mathbf{p}\right]\middle|\,\mathbf{V}^{(n,w)}\right)\right]\right\} \tag{5.11}$$

$$\mathcal{L}\left(\mathbf{p}\right) = -\frac{1}{2}\sum_{w=1}^{W}\sum_{n=1}^{N}\left\{\log\left(\left|\mathbf{C}\right|\right) + \left(K + 2\varphi_1\right)\log\left[\mathbf{V}^{(n,w)T}\mathbf{C}\mathbf{V}^{(n,w)} + 2\varphi_2\right]\right\} \tag{5.12}$$

$$\widehat{\mathbf{s}}_{MFMS-BCS} = \sum_{w=1}^{W}\sum_{n=1}^{N}\frac{\left\{\left[\hat{\mathbf{A}}^{(n)T}\hat{\mathbf{A}}^{(n)} + diag\left(\mathbf{p}\right)\right]^{-1}\hat{\mathbf{A}}^{(n)T}\mathbf{V}^{(n,w)}\right\}}{WN} \tag{5.13}$$

$$\widehat{\mathbf{s}}^{(n)}_{MFMS-BCS} = \sum_{w=1}^{W}\frac{\left\{\left[\hat{\mathbf{A}}^{(n)T}\hat{\mathbf{A}}^{(n)} + diag\left(\mathbf{p}\right)\right]^{-1}\hat{\mathbf{A}}^{(n)T}\mathbf{V}^{(n,w)}\right\}}{W} \tag{5.14}$$

5.3.3 DoA and BW Estimation Procedure

Once $\hat{\mathbf{s}}$ is estimated by (5.9), the number of estimated signals $\hat{L}$ are determined by counting number of non-zero entries in the retrieved signal vector $\hat{\mathbf{s}}$ by (5.9). In practice, many elements of $\hat{\mathbf{s}}$ are close but not equal to zero. This low energy signals called artifacts are due to the noise and must be filtered out as they do not correspond to any actual signals. Therefore, the energetic thresholding technique introduced in [78] has been applied to filter out the artifacts ($\hat{\mathbf{s}}_k \approx 0$) from the solution. Finally, the non-zero thresholded signals are considered as the actual impinging signals. The directions-of-arrivals (DoAs) are then estimated by associating each non-zero thresholded signal with respect to the candidate angles [78]. The estimation procedure is described as follows

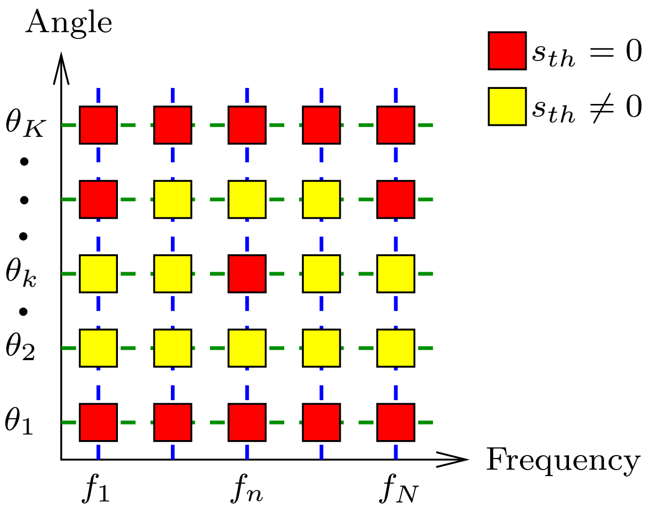

Figure 5.3: *MFMS−BCS-based Approach* - representation of thresholded signal vector with respect to candidate angular directions.

Step 0 - the estimated signal vectors $\widehat{\mathbf{s}}^{(n)}_{MFSS-BCS}$ or $\widehat{\mathbf{s}}^{(n)}_{MFMS-BCS}$ are thresholded as $s^{(n)}_{th} = \begin{cases} \widehat{\mathbf{s}}^{(n)}_{MFSS-BCS} \\ 0 \end{cases}$ or $s^{(n)}_{th} = \begin{cases} \widehat{\mathbf{s}}^{(n)}_{MFMS-BCS} \\ 0 \end{cases}$ by applying energetic thresholding described in [78];

Step 1- after thresholding, the thresholded values $s^{(n)}_{th}$ associated with each candidate angles θ_k, $k = 1, ..., K$ are lined-up with respect to each frequency samples f_n, $n = 1, ..., N$ as sketched in Fig. 5.3;

Step 2 - for each frequency, the number of non-zero thresholded value is the number of estimated DoAs $\hat{L}$ (e.g., $\hat{L} = 2$ for f_1 in Fig. 5.3) and the candidate angles having the non-zero thresholded values are considered as the estimated direction-of-arrivals (e.g., the estimated directions for f_1 are θ_2 and θ_k);

Step 3 - the minimum and maximum frequency of each estimated DoAs (computed in step 2) are computed by $f_{min}^{(\hat{\theta}_l)} = min\left\{f_n^{(\hat{\theta}_l)}\right\}$ and $f_{max}^{(\hat{\theta}_l)} = max\left\{f_n^{(\hat{\theta}_l)}\right\}$ respectively (e.g., $f_{min} = f_1$ and $f_{max} = f_N$ for θ_2 in Fig. 5.3);

Step 4 - then the bandwidth is computed for each estimated angles as $BW^{(\hat{\theta}_l)} = [f_{min}^{(\hat{\theta}_l)} : f_{max}^{(\hat{\theta}_l)}]$, $l = 1, ..., \hat{L}$. If computed BW includes any frequency that is not estimated at step 2, will be considered an estimation error and then added in the RMSE definition in 5.15. For example, the estimated BW for both θ_2 and θ_k in Fig. 5.3 are $BW = [f_1 : f_N]$ even there is no estimation of θ_k at f_n. In such case, $RMSE$ for each frequency will be summed up.

5.4 Performance of $MFSS - BCS$

In order to assess the performance of $MFSS - BCS$, an extensive analysis has been done by varying the number of frequency samples, number of signals, number of sensors, and different signal-to-noise ratio (SNR). The SNR is defined in (4.4). The performance is measured in terms of the root-mean-square-error ($RMSE$) [78], which is defined for each frequency of solution as follows

$$RMSE\left(f_n\right)=\begin{cases}\sqrt{\frac{\left\{\sum_{l=1}^{\hat{L}(f_n)}\left|\theta_l(f_n)-\hat{\theta}_l(f_n)\right|^2+\left|L(f_n)-\hat{L}(f_n)\right|(\Delta\theta_{max})^2\right\}}{L(f_n)}} & if\ \ \hat{L}\left(f_n\right)\leq L\left(f_n\right)\\ \sqrt{\frac{\left\{\sum_{l=1}^{L(f_n)}\left|\theta_l(f_n)-\hat{\theta}_l(f_n)\right|^2+\sum_{j=L+1}^{\hat{L}(f_n)}\left|\hat{\theta}_l(f_n)-\overline{\theta}_j(f_n)\right|^2\right\}}{L(f_n)}} & if\ \ \hat{L}\left(f_n\right)>L\left(f_n\right)\end{cases} \tag{5.15}$$

where, $L\left(f_n\right)$ and $\hat{L}\left(f_n\right)$ are the number of actual and estimated signals respectively at f_n, $n=1,...,N$, $\Delta\theta_{max}$ being maximum localization error (i.e., $\Delta\theta_{max}=180\,[deg]$) applied when the estimated number of signals $\hat{L}\left(f_n\right)$ are less than actual number of the signals $L\left(f_n\right)$ and $\overline{\theta}_j\left(f_n\right)=\arg\left\{\min_{\theta_l,\,l\in[1,L]}\left|\ \theta_l\left(f_n\right)-\hat{\theta}_l\left(f_n\right)\right|\right\}$. In (5.15), the value $\hat{\theta}_l\left(f_n\right)$ ($l=1,...,\hat{L}\left(f_n\right)$; $n=1,...,N$) corresponds to the DoA estimated at the n-th frequency which is closest to the l-th ($l=1,...,L\left(f_n\right)$) actual DoA. The average $RMSE$ at each noise realization $t=1,...,T$ is then computed as follows

$$RMSE^{(t)}=\frac{1}{N}\sum_{n=1}^{N}RMSE^{(t)}\qquad t=1,...,T;\ \ n=1,...,N\ . \tag{5.16}$$

First of all, the behaviour of the proposed method $MFSS - BCS$ is analyzed by comparing it with $MT - BCS$ for single snapshot data. This is because to understand the effect of replacing the multiple snapshots concept with the multiple frequency components. As it is obvious in [78], with the increase of number of snapshots the performance increases. Therefore, the objective is to verify the improvement of the estimation performance as a function of the number of frequency samples. In order to do that, consider a test scenario from [78] (reported in [78](Fig.5)) where $L=4$ binary phase-shift keying ($BPSK$) signals ($s_l=\pm1$) are impinging on a linear array of $M=20$ equally-spaced ($d=\frac{\lambda}{2}$ at $f=0.5$ [GHz]) isotropic sensors and the voltages V_m, $m=1,...,M$ collected at single snapshot ($W=1$) are corrupted by a noise level equivalent to a $SNR=10\,dB$. Among the 5 different sets of $DoAs$ in [78] (Fig. 5), the two sets namely the best set ([78] in Fig. 5(a), $\boldsymbol{\theta}=\{-79,\,-59,\,-41,\,10\}$ $[deg]$), and worst set ([78] in Fig. 5(e), $\boldsymbol{\theta}=\{-77,\,-31,\,16,\,87\}$ $[deg]$), are selected to show the behaviour of the proposed approach for both best and worst set. Similar to [78], the angular range $\theta\in[-90;\,90]$ $[deg]$ has been partitioned with a uniform grid of $K=181$ samples such that $\Delta\theta=1\,[deg]$. In order to apply $MFSS - BCS$, all $L=4$ $DoAs$ are considered as a wideband signals having equal bandwidth of $BW=0.5$

[GHz] in the range $f = [0.25 : 0.75]$ [GHz] and the voltages are collected at different uniformly spaced frequency samples (i.e., $f = 0.5$ [GHz] when $N = 1$, $f_n = \{f_1, f_2, f_3\} = \{0.3, 0.5, 0.7\}$ [GHz] when $N = 3$, $f_n = \{f_1, f_2, f_3, f_4, f_5\} = \{0.3, 0.4, 0.5, 0.6, 0.7\}$ [GHz] when $N = 5$, and $f_n = \{f_1, f_2, ..., f_{10}, f_{11}\} = \{0.3, 0.34, ..., 0.66, 0.7\}$ [GHz] when $N = 11$).

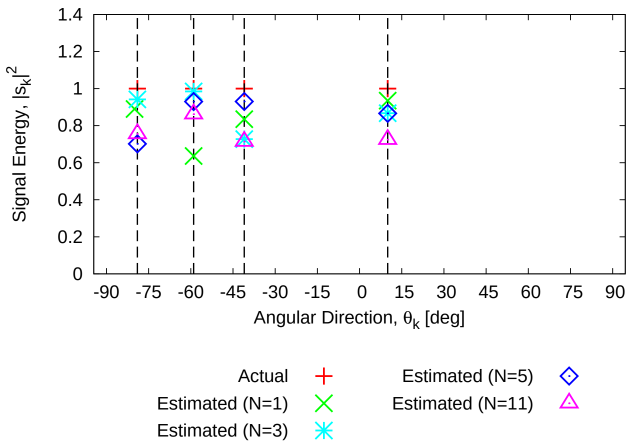

(a)

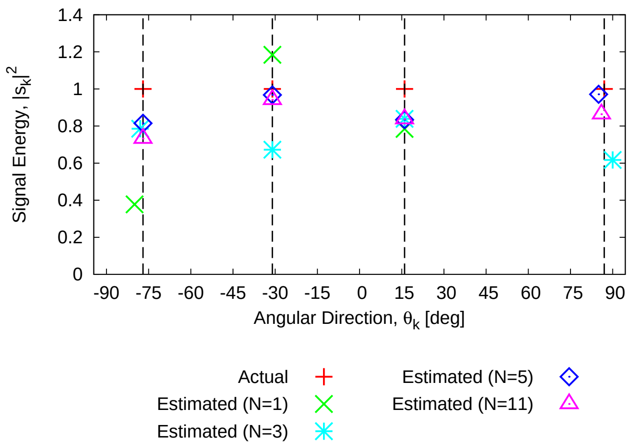

(b)

Figure 5.4: *Method Validation* ($N = \{1, 3, 5, 11\}$; $M = 20$, $d = 0.5\lambda_0$; $L = 4$, $BW = 0.5$ $[GHz]$, $SNR = 10\,dB$; $K = 181$, $T = 10$, and $W = 1$) - Best average DoAs estimation for [78] (Fig. 5) : (a) DoAs, $\boldsymbol{\theta} = \{-79, -59, -41, 10\}$ $[deg]$ and (b) DoAs, $\boldsymbol{\theta} = \{-77, -31, 16, 87\}$ $[deg]$.

Figure 5.4 shows the best (among $T = 100$ noise realizations) average estimation over $N = \{1, 3, 5, 11\}$ frequency samples for $DoAs$ $\boldsymbol{\theta} = \{-79, -59, -41, 10\}$ $[deg]$ [Fig. 5.4(a)] and for $DoAs$ $\boldsymbol{\theta} = \{-77, -31, 16, 87\}$ $[deg]$ [Fig. 5.4(b)]. Clearly, the performance of estimation is increased with the increase of N. In details, all signals are correctly estimated for all N except $N = 1$ as shown in

Fig. 5.4(a), where $RMSE$ is 0.5 [deg] as one signal is incorrectly estimated. For $DoAs$ $\boldsymbol{\theta} = \{-77,\ -31,\ 16,\ 87\}$ $[deg]$, only three signals are estimated at $N = 1$ as shown in Fig. 5.4(b), among which one signal is incorrect ($-81\,[deg]$) which results $RMSE = 90.02$ [deg] .

Table 5.1: *Method Validation* ($N = \{1, 3, 5, 11\}$; $M = 20$, $d = 0.5\lambda_0$; $L = 4$, $BW = 0.5$ $[GHz]$, $SNR = 10\,dB$; $K = 181$, $T = 10$, and $W = 1$) - Estimated DoAs for $DoAs$, $\boldsymbol{\theta} = \{-79,\ -59,\ -41,\ 10\}$ $[deg]$ and $\boldsymbol{\theta} = \{-77,\ -31,\ 16,\ 87\}$ $[deg]$

$\boldsymbol{\theta} = \{-79,\ -59,\ -41,\ 10\}$ $[deg]$			$\boldsymbol{\theta} = \{-77,\ -31,\ 16,\ 87\}$ $[deg]$		
N	$\tilde{\boldsymbol{\theta}}\,[deg]$	$RMSE\,[deg]$	N	$\tilde{\boldsymbol{\theta}}\,[deg]$	$RMSE\,[deg]$
1	$\{-80,\ -59,\ -41,\ 10\}$	0.50	1	$\{-80,\ -31,\ 16\}$	90.01
3	$\{-79,\ -59,\ -41,\ 10\}$	0.00	3	$\{-78,\ -31,\ 16,\ 90\}$	1.58
5	$\{-79,\ -59,\ -41,\ 10\}$	0.00	5	$\{-77,\ -31,\ 16,\ 85\}$	1.00
11	$\{-79,\ -59,\ -41,\ 10\}$	0.00	11	$\{-77,\ -31,\ 16,\ 86\}$	0.50

Tab. 5.1 shows the estimated angles and associated $RMSE$ for each N. In the case of more than one frequency samples, all four signals are estimated among which three of them are equal to the actual $DoAs$. Although one signal is not exact, the performance in terms of $RMSE$ is significantly improved with the increase of number of incoming signals as reported in Tab. 5.1.

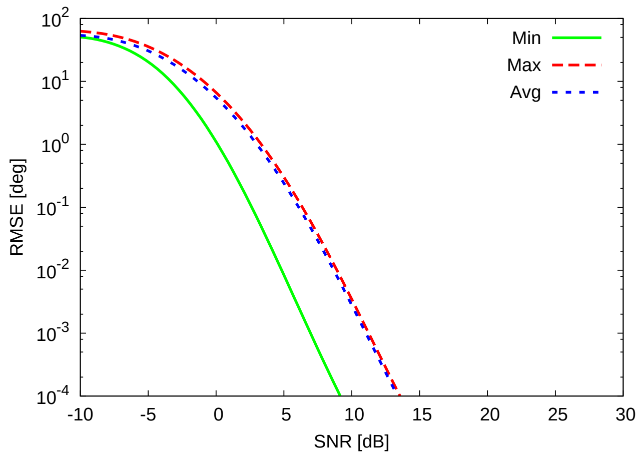

Figure 5.5: *Performance Analysis* ($L = 4$, $BW = 0.5$ $[GHz]$, $SNR = [-10 : 30]\,dB$; $N = 5$, f =[0.25 : 0.75] $[GHz]$, f_n =$\{0.3, 0.4, 0.5, 0.6, 0.7\}$ $[GHz]$; $M = 20$, $d = 0.5\lambda_0$; $K = 181$, and $W = 1$) - Minimum, maximum, and average $RMSE$ values among $T = 100$ simulations.

Table 5.2: *Performance Analysis* ($L = 4$, $BW = 0.5$ $[GHz]$, $SNR = [-10 : 30]\, dB$; $N = 5$, f =[0.25 : 0.75] $[GHz]$; $M = 20$, $d = 0.5\lambda_0$; $K = 181$, and $W = 1$) - Minimum, maximum, and average $RMSE$ values among $T = 100$ simulations

$SNR[dB]$	$Min[deg]$	$Max[deg]$	$Mean[deg]$
-10	50.59	62.63	53.69
-5	39.66	51.70	46.82
0	9.49	29.54	22.27
5	0.50	0.54	0.52
10	0.00	0.50	0.27
15	0.00	0.00	0.00
20	0.00	0.00	0.00
25	0.00	0.00	0.00
30	0.00	0.00	0.00

In order to analyze the behaviour of the $MF - BCS$ for different noisy conditions, the same test scenario for $DoAs$ $\boldsymbol{\theta} = \{-79, -59, -41, 10\}$ $[deg]$ has been considered to be analyzed with respect to different $SNRs$ for fixed number of frequency samples, $N = 5$. The outcome is graphically presented in Fig. 5.5, where it can be observed that the minimum required SNR is equal to $SNR = 15$ [dB] to estimates the exact $DoAs$ without any error. However, the $RMSE$ is the order of magnitude for heavy noisy conditions $SNR \leq 0$ [dB], although $RMSE < 1$ [deg] when $SNR = 5$ [dB] and $SNR = 10$ [dB] as reported in Tab. 5.2.

Since the performance depends on number of frequency samples (as in Fig. 5.4), $SNRs$ (as in Fig. 5.5), and also the number of incoming signals (as it affects the sparsity conditions), an analysis is done for $L = \{2, 3, 4\}$, $N = \{1, 3, 5, 7, 9, 11\}$, and $SNR = 0$ [dB] and the results are presented in Fig. 5.6. There is at-least one exact estimation among $T = 100$ noise realizations for $L = 2$ when $N = 3$ and for $L = 3$ when $N = 11$, although there is no correct estimation for $L = 4$ as shown in Fig 5.6. The curve for average estimation of $L = 2$ signals shows that only $N = 5$ frequency samples data is sufficient to estimate the exact $DoAs$ even at $SNR = 0$ [dB]. The RMSE of average estimation for $L > 2$ signals is high at $SNR = 0$ [dB].

More in details, example of best estimation of $DoAs$ is graphically plotted in Fig. 5.7 [Fig. 5.7(a) for $L = 2$ and Fig. 5.7(b) for $L = 3$] and the estimated $DoAs$ are reported in Tab. 5.3. As it can be shown that the estimated number of signals are higher than the actual number for $N = 1$ which results high $RMSE$ as reported in Tab. 5.3. Overall, the performance is significantly improved with the increase of number of frequency samples. It can be noticed in Tab. 5.3 that

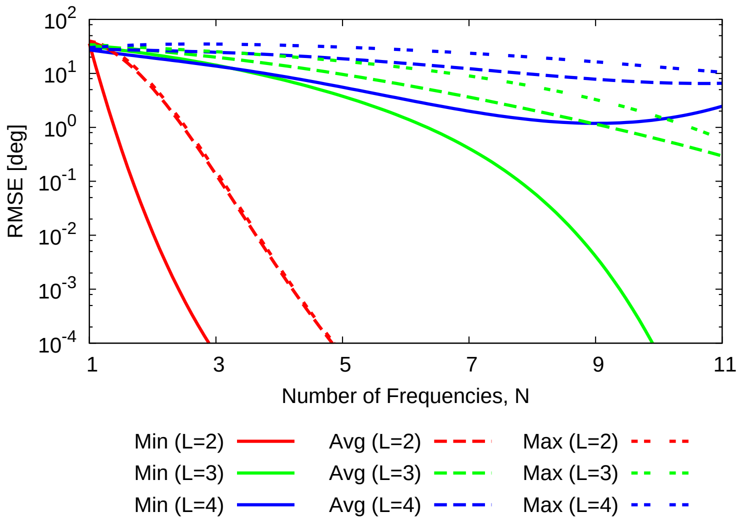

Figure 5.6: *Performance Analysis* ($L = \{2, 3, 4\}$, $BW = 0.5$ $[GHz]$, $SNR = 0\,dB$; $N = [1, :\ 11]$, f =[0.25 : 0.75] $[GHz]$; $M = 20$, $d = 0.5\lambda_0$; $K = 181$, and $W = 1$) - Minimum, maximum, and average $RMSE$ values among $T = 100$ simulations.

the $RMSE$ for $N = 5$ is 6.58 [deg] even though the average estimation is exact. This is because the estimated $DoAs$ are the averaged $DoAs$, but the $RMSE$ is computed including the estimation at different frequency samples as well. There are close but not exact estimation at f_3, f_4, and f_5 which makes the estimation with non-zero $RMSE$ even the average estimation of $DoAs$ are exact.

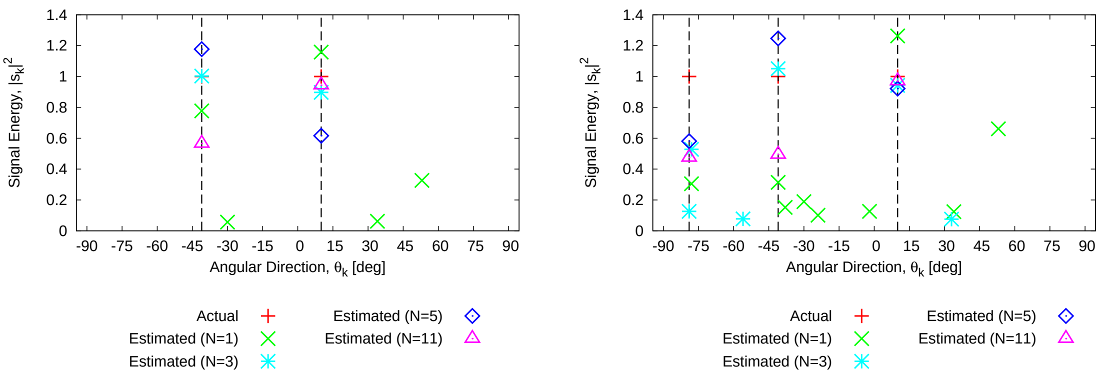

(a) (b)

Figure 5.7: *Performance Analysis* ($L = \{2, 3\}$, $BW = 0.5$ $[GHz]$, $SNR = 0\,dB$;$N = [1, :\ 11]$, f =[0.25 : 0.75] $[GHz]$; $M = 20$, $d = 0.5\lambda_0$; $K = 181$, $T = 100$, and $W = 1$) - Best average DoAs estimation for : (a) DoAs, $\boldsymbol{\theta} = \{-41, 10\}$ $[deg]$ and (b) DoAs, $\boldsymbol{\theta} = \{-79, -41, 10\}$ $[deg]$.

Table 5.3: *Performance Analysis* ($L = \{2, 3\}$, $BW = 0.5$ $[GHz]$, $SNR = 0\,dB$; $N = [1,:\ 11]$, f =[0.25 : 0.75] $[GHz]$; $M = 20$, $d = 0.5\lambda_0$; $K = 181$, $T = 100$, and $W = 1$) - Best average $DoAs$ estimation.

	$DoAs$, $\boldsymbol{\theta} = \{-41,\ 10\}$ $[deg]$		$DoAs$, $\boldsymbol{\theta} = \{-79,\ -41,\ 10\}$ $[deg]$	
N	$\tilde{\boldsymbol{\theta}}$ $[deg]$	$RMSE$ $[deg]$	$\tilde{\boldsymbol{\theta}}$ $[deg]$	$RMSE$ $[deg]$
1	$\{-41,\ -30$ $-10,\ 34,\ 53\}$	35.68	$\{-78,\ -41,\ -38,\ -30,$ $-24,\ -2,\ 10,\ 34,\ 53\}$	31.57
3	$\{-41,\ 10\}$	0.00	$\{-79,\ -78,\ -56,\ -41,\ 10,\ 33\}$	17.57
5	$\{-41,\ 10\}$	0.00	$\{-79,\ -41,\ 10\}$	6.58
11	$\{-41,\ 10\}$	0.00	$\{-79,\ -41,\ 10\}$	0.00

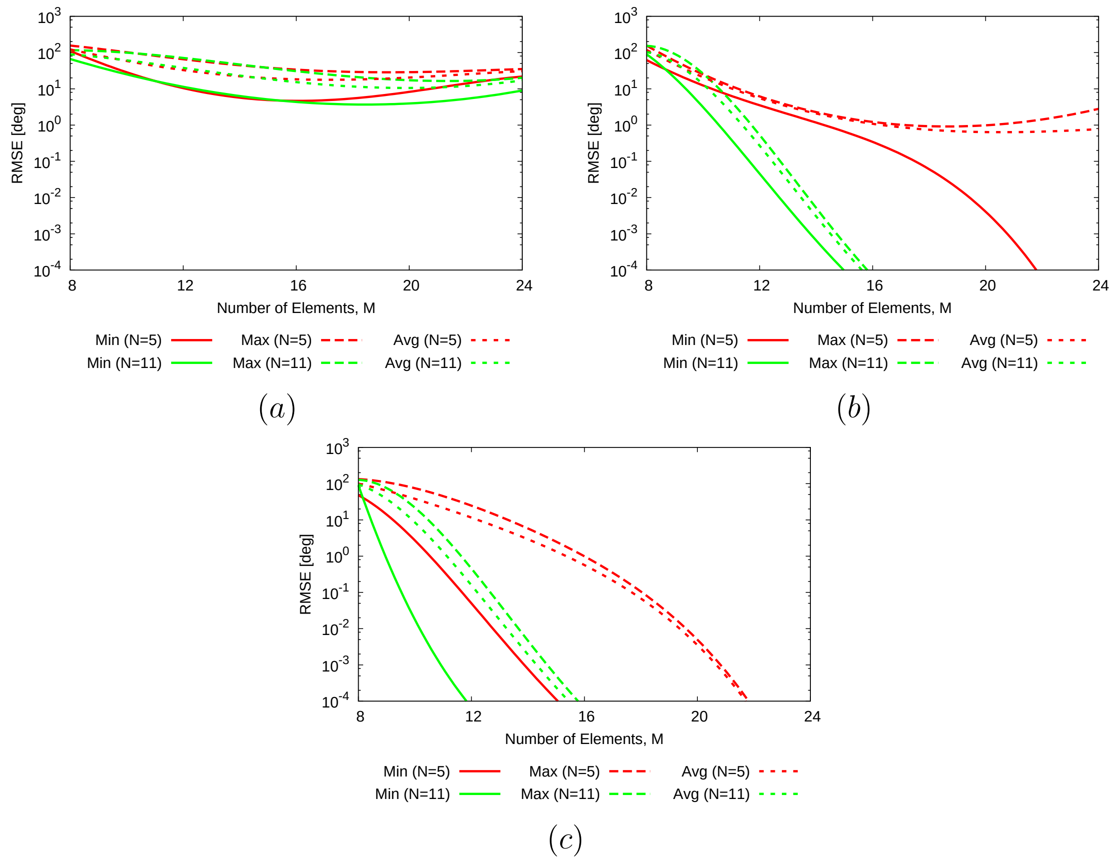

Figure 5.8: *Performance Analysis* ($M = [8\ :\ 24]$, $d = 0.5\lambda_0$; f =[0.25 : 0.75] $[GHz]$, $N = \{5,\ 11\}$; $L = 4$, $\boldsymbol{\theta} = \{-79,\ -59,\ -41,\ 10\}$ $[deg]$, $BW = 0.5$ $[GHz]$, $SNR = \{0,\ 5,\ 10\}$ dB; $K = 181$, and $W = 1$) - Best, worst, and average $RMSE$ values among $T = 100$ simulations: (a) $SNR = 0\,dB$, (b) $SNR = 5\,dB$, and (c) $SNR = 10\,dB$.

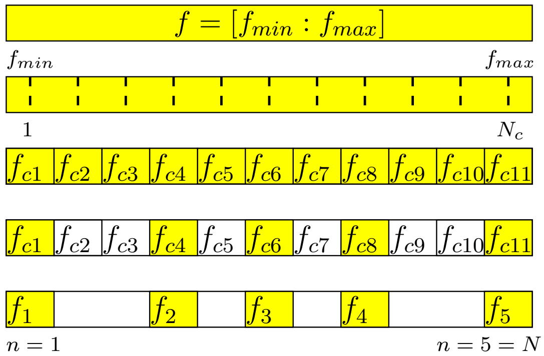

Figure 5.9: *Performance Analysis* - Non-uniform frequency sampling procedure.

To analyze the effect of number of elements, an analysis is done considering the same scenario for different $N = \{5, 11\}$ and different noisy conditions i.e., $SNR = \{0, 5, 10\}$ [dB] and the result is presented in Fig. 5.8 [Fig. 5.8(a) for $SNR = 0$ [dB], Fig. 5.8(b) for $SNR = 5$ [dB] and Fig. 5.8(c) for $SNR = 10$ [dB]]. Although there is no substantial improvement of performance for $SNR = 0$ [dB] [Fig. 5.8(a)], overall the $RMSE$ is decreased as number of elements are increased for $SNRs$ higher than 0[dB] as shown in Fig. 5.8(b) for $SNR = 5$ [dB] and Fig. 5.8(c) for $SNR = 10$ [dB]. This indicates that the performance of $MFSS - BCS$ is compromised in case of highly noisy conditions $SNR \leq 0$ [dB].

Unlike the uniform frequency sampling analyzed above, the next example deals with the analysis for non-uniform sampling. Figure 5.9 describes the procedure of non-uniform sampling. First of all, the available BW is discretized into N_c number of candidate uniform samples. Then the number of required samples N is randomly selected from candidate N_c samples.

The test scenario considered in Fig. 5.4(a) for uniform sampling has been considered in this example to show the performance in comparative fashion. Here the available BW is discretized into $N_c = 11$ candidate samples (e.g., $f_{cn} = \{f_{c1}, ..., f_{c11}\} = \{0.30, \ldots, 0.7\}$ [GHz]) and $N = 5$ samples is then selected $f_n = \{f_1, f_2, f_3, f_4, f_5\} = \{0.3, 0.42, 0.5, 0.58, 0.7\}$ [GHz]. Figure 5.10 shows the best estimation at individual frequencies among $T = 100$ noise realization for both uniform and non-uniform samples. The DoAs estimated by both sampling strategies are exactly equal to the actual DoAs, although signal's energy is higher in uniform frequency samples as shown in Fig. 5.10. Overall, the average performance of uniform sampling is higher (e.g., $RMSE_{mean} = 0.28$ [deg]) than the non-uniform sampling (e.g., $RMSE_{mean} = 0.42$ [deg]), although the minimum and maximum $RMSE$ is exactly same.

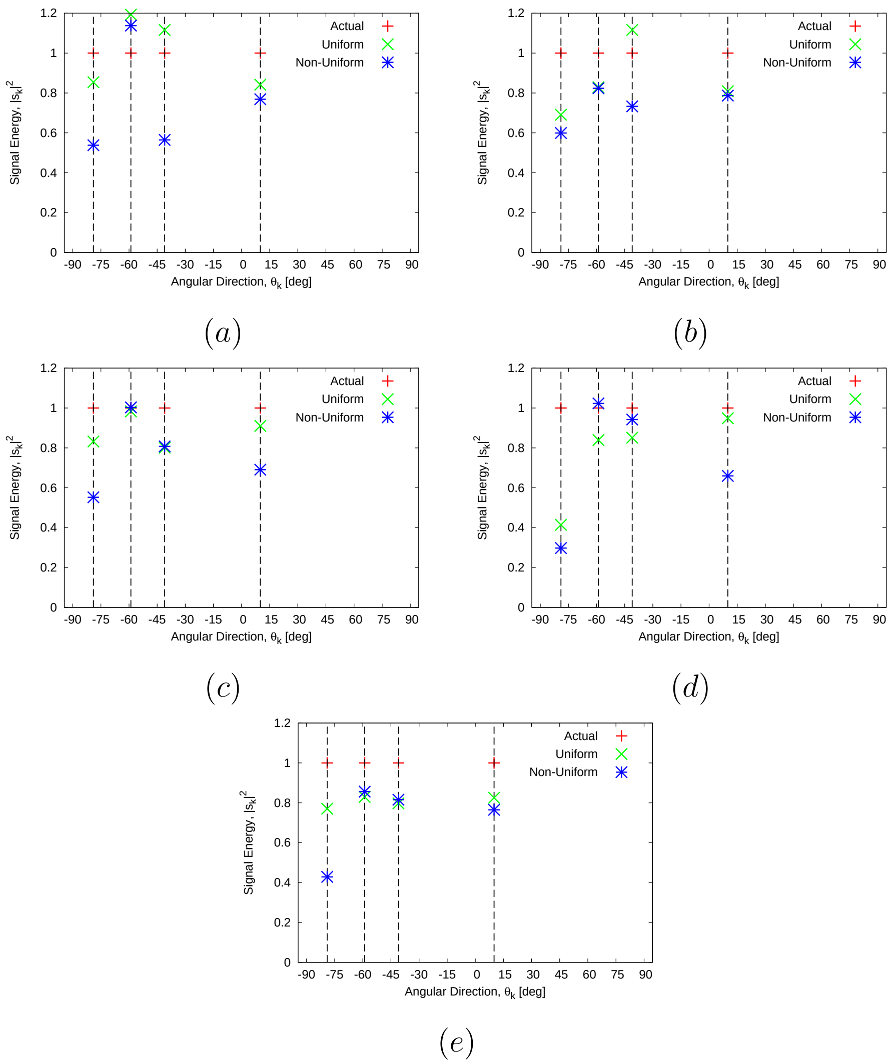

Figure 5.10: *Performance Analysis* ($N = 5$, $L = 4$, $SNR = 10\,dB$; $M = 20$, $d = 0.5\lambda_0$; $K = 181$, $W = 1$, $BW = 0.5$ $[GHz]$, $f_n^{Uniform}$ =$\{0.3, ..., 0.7\}$ $[GHz]$, $f_n^{Non-Uniform}$ =$\{0.30, 0.42, 0.50, 0.58, 0.70\}$ $[GHz]$;) - Best *DoA*s estimation among $T = 100$ simulations for different frequency samples: (a) f_1, (b) f_2, (c) f_3, (d) f_4, and (e) f_5.

In order to guarantee the reliability of the estimation, an analysis has been done with the more realistic data collected by the *EM* simulator. To do so, an array of $M = 20$ equally-spaced by half-wavelength ($d = \frac{\lambda}{2}$ at $f = 0.5$ [GHz]) $y-$oriented dipoles are placed along $x-$axis as shown in Fig. 5.11. Each of the dipoles are considered as a series load with series resistance $R_s = 72$ [ohm], capacitance $C_s = 0$ [F], and inductance $L_s = 0$ [H]. $L = 3$ wide band ($f = [0.25 : 0.75]$ [GHz]) plane waves with magnitude of 1 [V/m] are placed in $z-$axis in such a way that the directions from the array reference points are *DoA*s

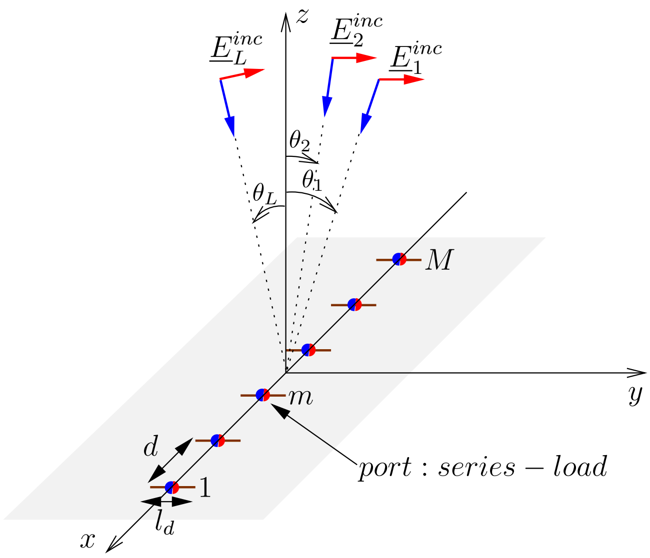

Figure 5.11: *Performance Analysis* - Sketch of the model implemented in EM simulator

$\boldsymbol{\theta} = \{-45, -21, 10\}$ $[deg]$. The simulated data (measured voltages) collected at each $N = 5$ frequency samples are normalized with respect to the maximum of the absolute value and then amplified in order to have the sufficient signal energy so that the useful signals are not affected by energy thresholding strategy. These amplified voltages are then directly fed to the $MFSS - BCS$ solver

The performance of the proposed approach for $K = 181$ angular directions is presented in Fig. 5.12, where the DoAs estimated at each individual frequencies and also average estimated DoAs are plotted with respect to angular directions. The $MFSS - BCS$ correctly estimates all DoAs without any error as shown in Fig. 5.12. As expected, although the estimated signals energy are different for each frequency, the average estimated energy is close to the actual considered energy. The over estimated signal's energy is due to the effects of mutual coupling among antennas.

Moreover, the performance of the $MFSS - BCS$ has been compared with [107] (i.e., deterministic CS, subspace-based estimators like MUSIC and its different versions). With referring to [107], $L = 2$ acoustic signals from $DoAs$ $\boldsymbol{\theta} = \{-60, 30\}$ $[deg]$ directions are impinging on a linear array of $M = 6$ elements separated by $d = \frac{\lambda}{2}$ at 550 [Hz]. The voltages measured at the terminal of each elements at each frequencies $f_n = \{f_1, f_2, f_3, f_4\} = \{300, 500, 600, 800\}$[Hz] are subject to the noise level of $SNR = 0$ [dB] and the number of snapshots considered in $MFSS - BCS$ and [107] are 1 and 256 respectively. The voltages are collected with and without polarization loss for $MF - BCS$ only to show the behaviour of $MFSS - BCS$ for different values of polarization mismatch as well. Figure 5.13 plots the actual and estimated $DoAs$ for proposed approach

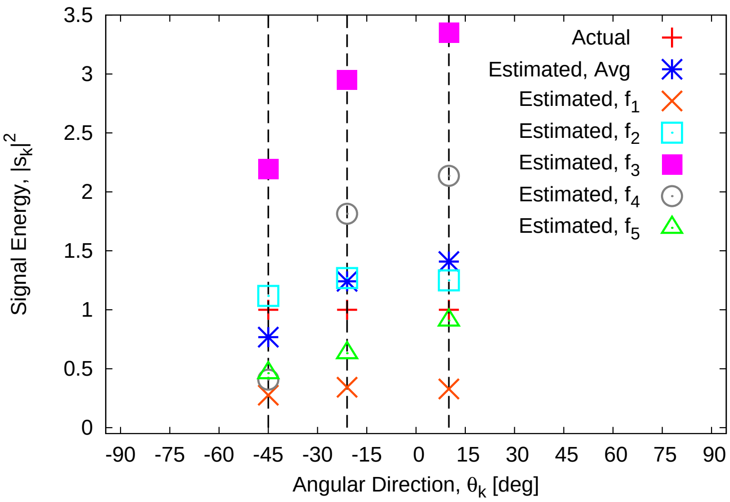

Figure 5.12: *Performance Analysis* ($L = 3$, $BW = 0.5$ $[GHz]$, DoAs, $\boldsymbol{\theta} = \{-45, -21, 10\}$ $[deg]$; $N = 5$, $f = [0.25 : 0.75]$ $[GHz]$, $f_n = \{0.3, ..., 0.7\}$ $[GHz]$; $M = 20$, $d = 0.5\lambda_0$; $K = 181$, and $W = 1$) - DoAs estimation from EM data.

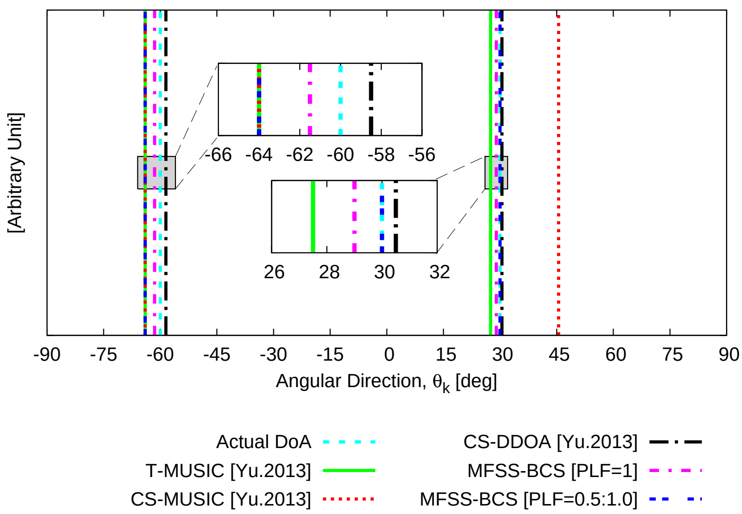

Figure 5.13: *Performance Comparison* ($M = 6$, $d = 0.5\lambda_0$; $f = [300 : 800]$ $[Hz]$, $N = 4$, $f_n = \{300, 500, 600, 800\}$ $[Hz]$; $L = 2$, $\boldsymbol{\theta} = \{-60, 30\}$ $[deg]$, $SNR = 0\,dB$; $K = 181$, $T = 30$) - Best average DoAs estimation.

Table 5.4: *Performance Comparison* ($M=6$, $d=0.5\lambda_0$; $f=$[300 : 800] $[Hz]$, $N=4$, $f_n=${300, 500, 600, 800} $[Hz]$; $L=2$, $\boldsymbol{\theta}=\{-60,30\}$ $[deg]$, $SNR=0\,dB$; $K=181$, $T=30$) - Best average DoAs estimation

$Algorithm$	$\boldsymbol{\theta}\,[deg]$	$\tilde{\boldsymbol{\theta}}\,[deg]$	$RMSE[deg]$
$T-MUSIC$	$\{-60,30\}$	$\{-64,27.5\}$	3.34
$CS-MUSIC$	$\{-60,30\}$	$\{-64,45.5\}$	11.32
$CS-DDoA$	$\{-60,30\}$	$\{-58.5,30.5\}$	1.18
$MFSS-BCS\,[PLF=1.0]$	$\{-60,30\}$	$\{-61.5,29\}$	1.27
$MFSS-BCS\,[PLF=0.5:1.0]$	$\{-60,30\}$	$\{-64,30\}$	2.82

(e.g., without the loss of polarization where $PLF=1.0$ and with the loss of polarization where $PLF=[0.5:1.0]$), deterministic CS [107] (e.g.,CS-DDoA), and MSUIC reported in [107] (e.g., T-MUSIC, CS-MUSIC). The actual and estimated $DoAs$ for the mentioned approaches have also been reported in Tab. 5.4. Overall, the performance of compressive sensing based method is higher than the subspace-based estimator like T-MUSIC and/or CS-MUSIC. Although the performance of CS-DDoA and $MFSS-BCS$ are approximately equal in terms of $RMSE$, the $MFSS-BCS$ considered only single-snapshot data while $W=256$ snapshots considered in [107].

In addition, the performance of $MFSS-BCS$ has also been compared with [77], where $L=2$ wide band signals having bandwidth of $BW=40$ [Hz] (in the range $f=[80:120]$ [Hz]) coming from directions $DoAs$ $\boldsymbol{\theta}=\{-10,20\}$ $[deg]$ are impinging on a linear array of $M=16$ elements separated by $d=\frac{\lambda}{2}$ at 120 [Hz]. The measured signals at each element are subject to different noise level of $SNR=[-15:15]$ [dB]. Figure 5.14 shows the estimated average $RMSE$ for $T=100$ noise realizations as a comparative fashion. Although, the performance of WP and WOP [77] is slightly higher in extremely noisy conditions (e.g., $SNR=[-15:-5]$ [dB]), the $MFSS-BCS$ (without polarization loss) outperforms when $SNR=[-5:15]$ [dB].

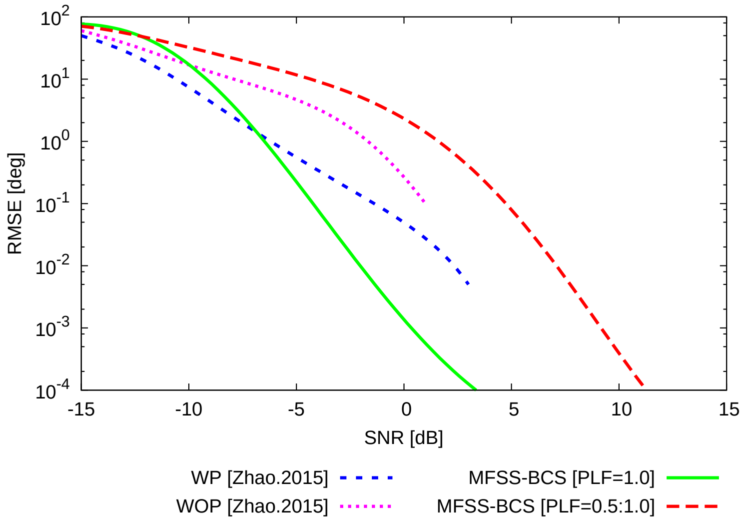

Figure 5.14: *Performance Comparison* ($M = 16$, $d = 0.5\lambda_0$; f =[80 : 120] $[Hz]$, $N = 5$, f_n ={80, 90, 100, 110, 120} $[Hz]$; $L = 2$, $\boldsymbol{\theta} = \{-10, 20\}$ $[deg]$, $SNR = [-15 : 15]\, dB$; $K = 37$, $T = 100$) - Best average DoAs estimation.

5.5 Performance of $MFMS - BCS$

Let us consider $L = 2$ binary phase-shift keying ($BPSK$) signals ($E_l^{inc} = \pm 1$) with equal bandwidth set to $BW_1 = BW_2 = 0.5$ [GHz] in the range $f = [0.25 : 0.75]$ [GHz] that are impinging on a linear array of $M = 20$ equally-spaced ($d = \frac{\lambda_0}{2}$, where $\lambda_0 = 0.5$ [GHz]) isotropic sensors (i.e., $\boldsymbol{\mathcal{H}} = 1$) where the measured voltages are corrupted by a noise level equal to $SNR = 0\,dB$. The voltages are collected for $W = [1 : 15]$ snapshots and for each snapshot the data are considered over $N = \{1, 5\}$ frequency samples. More precisely, the selected frequencies for $N = 5$ are $f_1 = 0.3$ [GHz], $f_2 = 0.4$ [GHz], $f_3 = f_0 = 0.5$ [GHz], $f_4 = 0.6$ [GHz], and $f_5 = 0.7$ [GHz]. When applying the *MFMS-BCS*, the angular range $\theta \in [-90; 90]$ $[deg]$ has been partitioned with $K = 181$ samples to obtain a uniform grid of step $\delta\theta = 1\,[deg]$. For validation purposes, two different scenarios with $L = 2$ signals having closely spaced and widely spaced DoAs have been considered. The closely spaced DoAs have been set to $\boldsymbol{\theta} = \{-70, -64\}$ $[deg]$ and the widely spaced DoAs to $\boldsymbol{\theta} = \{-75, 30\}$ $[deg]$.

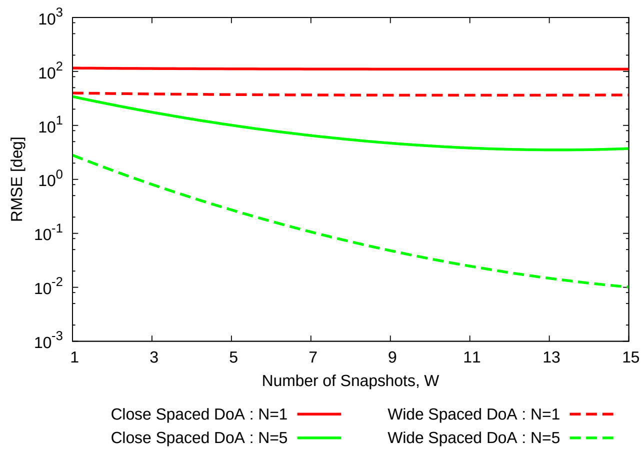

Figure 5.15: *Method Validation* ($W = [1 : 15]$; $M = 20$, $d = 0.5\lambda_0$; $f =[0.25 : 0.75]$ $[GHz]$, $N = \{1, 5\}$, $L = 2$, close spaced DoAs, $\boldsymbol{\theta} = \{-70, -64\}$ $[deg]$, wide spaced DoAs, $\boldsymbol{\theta} = \{-75, 30\}$ $[deg]$, $SNR = 0\,dB$; $K = 181$) - Average $RMSE$s values among $T = 100$ simulations

Figure 5.15 represents the statistics of the RMSE values in order to show the effectiveness of exploiting both time and frequency data. As expected, the performance is higher for the widely spaced DoAs, although adding only time domain data (for $N = 1$) is not enough when $SNR = 0\,dB$ as shown in Fig. 5.15 (red curves). However, the addition of frequency sampled ($N = 5$) data significantly improves the performance and the estimation errors are monotonically decreased with the increase of number of time domain data as in Fig. 5.15 for both close and wide spaced DoAs.

In order to extensively analyze the effectiveness and the reliability of the proposed approach, $I = 100$ sets of $L = 2$ random DoAs have been generated. Two constraints have been considered in the generation of random DoAs that are the angular range set equal to $\theta \in [-80; 80]$ $[deg]$ and the minimum angular separation between the DoAs chosen as $\Delta\theta_{min} = 5\,[deg]$. All other parameters are kept the same of the previous example. The minimum, maximum, and average $RMSE$ values among $T = 50$ noise realizations for each configuration of the $L = 2$ random DoAs have been graphically presented in Fig. 5.16 ([Fig. 5.16(a)] for $W = 1$, [Fig. 5.16(b)] for $W = 5$, and [Fig. 5.16(c)] for $W = 15$). As it is evident that the average $RMSE$ with $W = 15$ snapshot is zero for higher number of random DoA sets than $W = 1$. Therefore, the time and frequency processing is robust even in the extremely noisy condition $SNR = 0$ [dB].

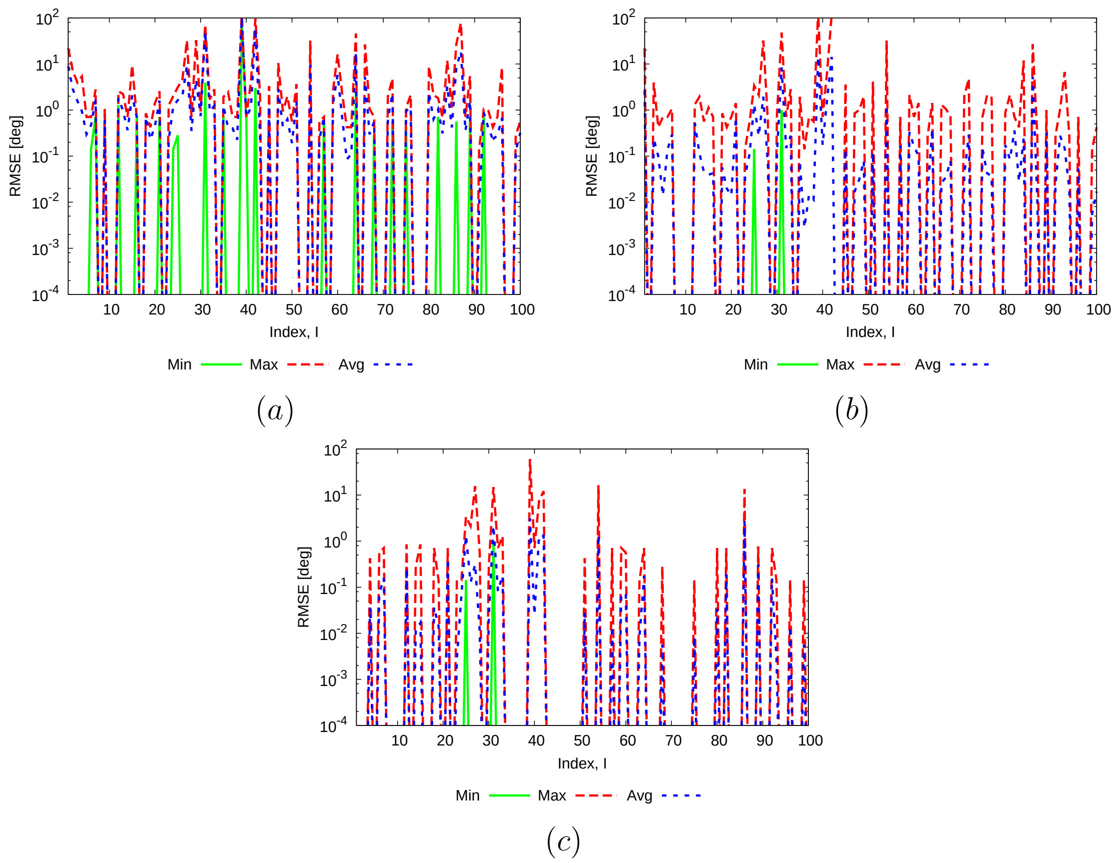

Figure 5.16: *Performance Analysis* ($W = \{1, 5, 15\}$; $M = 20$, $d = 0.5\lambda_0$; f =[0.25 : 0.75] $[GHz]$, $N = 5$; $L = 2$, $BW = 0.5$ $[GHz]$, $SNR = 0\,dB$; $K = 181$, $T = 100$) - Best, worst, and average $RMSE$ values among $T = 100$ simulations for $I = 100$ random sets of DoAs: (a) $W = 1$, (b) $W = 5$, and (c) $W = 15$ snapshots.

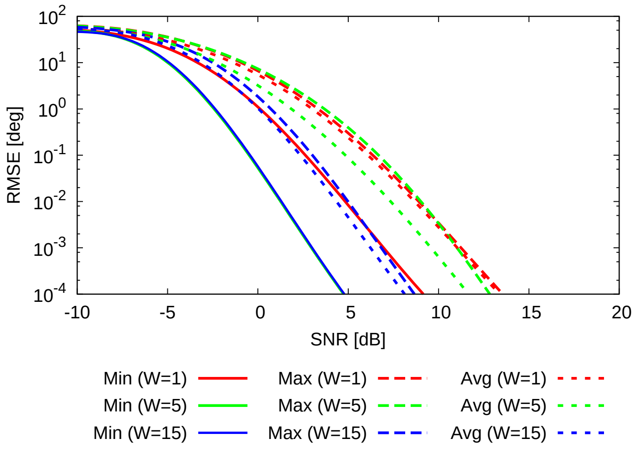

Figure 5.17: *Performance Analysis* ($W = \{1, 5, 15\}$; $M = 20$, $d = 0.5\lambda_0$; f =[0.25 : 0.75] $[GHz]$, $N = 5$; $L = 4$, $\boldsymbol{\theta} = \{-79, -59, -41, 10\}$ $[deg]$, $BW = 0.5$ $[GHz]$, $SNR = [-10 : 20]\,dB$; $K = 181$) - Best, worst, and average $RMSE$ values among $T = 100$ simulations.

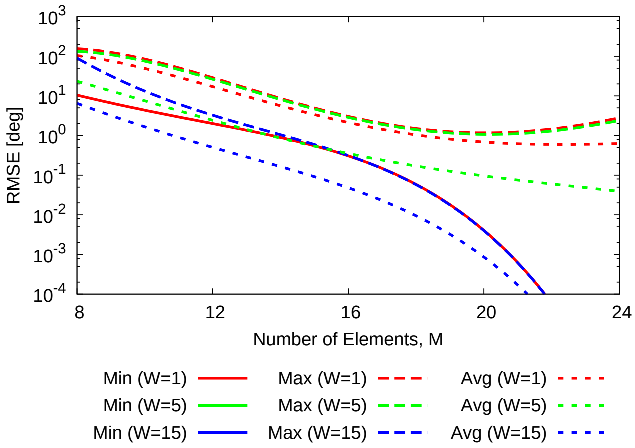

Figure 5.18: *Performance Analysis* ($W = \{1, 5, 15\}$; $M = \{8, 12, 16, 20, 24\}$, $d = 0.5\lambda_0$; f =[0.25 : 0.75] $[GHz]$, $N = 5$; $L = 4$, $\boldsymbol{\theta} = \{-79, -59, -41, 10\}$ $[deg]$, $BW = 0.5$ $[GHz]$, $SNR = 5\,dB$; $K = 181$) - Best, worst, and average $RMSE$ values among $T = 100$ simulations.

To investigate the effect of the noise level, an analysis for a set of $L = 4$ fixed DoAs equal to $\boldsymbol{\theta} = \{-79, -59, -41, 10\}$ $[deg]$ has been carried out by varying the signal-to-noise ratio in the range $SNR = [-10 : 20]\,dB$. The obtained results are plotted in Fig. 5.17. By observing the behavior of the minimum $RMSE$ curves, it is evident that low $RMSE$ values are achieved with $W = 5$

and $W = 15$ snapshots even for $SNR = 5$ dB while about $SNR = 10$ dB are needed to achieve similar estimation performance with $W = 1$. Overall, the statistical performance improve, whatever W, with the increment of the SNR as shown in Fig. 5.17. As for the average $RMSE$ values, it becomes equal to zero at $SNR = 8$ dB for $W = 15$ while at least $SNR = 13$ dB are required for $W = 1$ and $W = 5$.

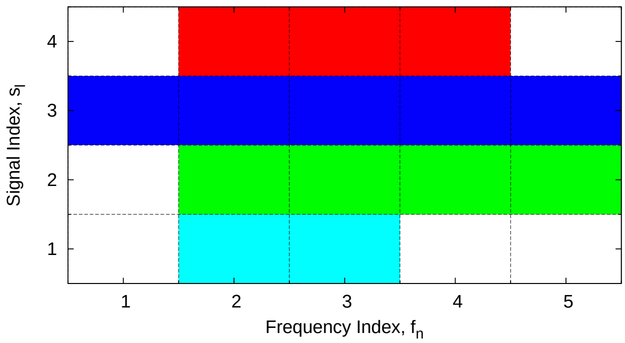

Figure 5.19: *Performance Analysis* -Signals and bandwidth configurations for the estimation of signals having different bandwidth.

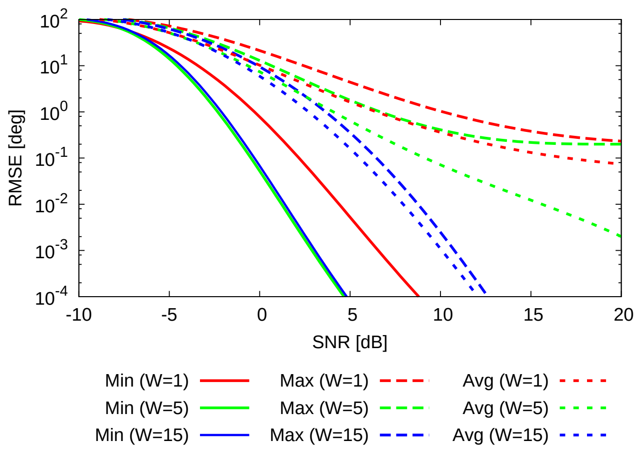

Figure 5.20: *Performance Analysis* ($W = [1, 5, 10, 15]$; $M = 20$, $d = 0.5\lambda_0$; f =[0.25 : 0.75] $[GHz]$, $N = 5$; $L = 4$, $\boldsymbol{\theta} = \{-79, -59, -41, 10\}$ $[deg]$, $SNR = [-10 : 20]\, dB$; $K = 181$) - Best, worst, and average $RMSE$ values among $T = 100$ simulations..

The analysis versus the number of elements M for $SNR = 5$ dB has been also carried out and the obtained results are represented in Fig. 5.18. It is possible to observe that the capacity of exact estimation improves for higher values of M. In addition, the condition $RMSE = 0$ [deg] is achieved for all M when $W = 5$ and $W = 15$ (indeed the minimum $RMSE$ curves are not appearing in the graph) while more than $M = 22$ elements are required in case of single snapshot data.

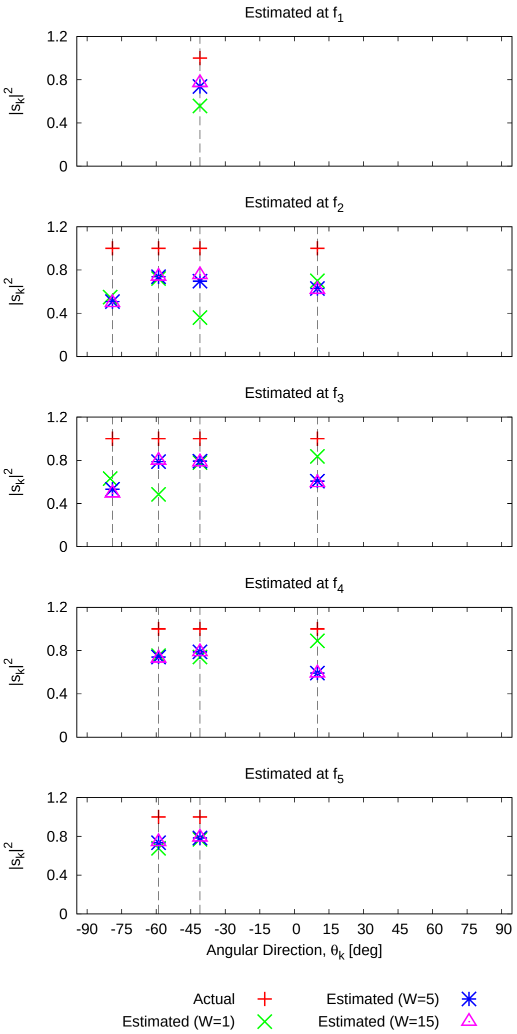

Figure 5.21: *Performance Analysis* ($W = \{1, 5, 15\}$; $M = 20$, $d = 0.5\lambda_0$; f =[0.25 : 0.75] $[GHz]$, $N = 5$, f_n ={0.3, 0.4, 0.5, 0.6, 0.7} $[GHz]$; $L = 4$, $\boldsymbol{\theta} = \{-79, -59, -41, 10\}$ $[deg]$, $SNR = 5\,dB$; $K = 181$, $T = 100$) - *DoAs* estimation at individual frequencies.

In order to consider a scenario characterized by signals having different bandwidth, the actual signals and frequency configuration shown in Fig. 5.19 have been taken into account. In details, the first signal $\boldsymbol{\theta}_1 = -79\,[deg]$ exists only at

f_2 and f_3, the second signal $\boldsymbol{\theta}_2 = -59\,[deg]$ at f_2, f_3, f_4, and f_5, the third signal $\boldsymbol{\theta}_3 = -41\,[deg]$ at all frequencies, and the fourth signal $\boldsymbol{\theta}_4 = 10\,[deg]$ only at f_2, f_3, and f_4. In order to investigate the potentialities of the proposed *MFMS-BCS* method for the joint *DoA*s and *BW* estimation of signals having different bandwidths of Fig. 5.19, the results of the analysis when varying the SNR (Fig. 5.20) for different number of snapshots W have been reported.
Similar to the case of signals having equal bandwidth (Fig. 5.17), the condition $RMSE = 0$ [deg] is achieved for $SNR = 5$ [dB] for all W except $W = 1$ as shown in Fig. 5.20. Although the average $RMSE$ values for $W = 1$ and for $W = 5$ are not zero, the performance improve with the SNR.
Finally, in order to show the correct estimation of both the signals bearing and bandwidth, Fig. 5.21 reports the actual and the best estimated *DoA*s at each frequency sample for different number of snapshots when considering the same test case with $SNR = 5\,dB$. It is clearly evident that the actual *DoA*s are correctly estimated (i.e., with $RMSE = 0\,[deg]$) for all frequencies when $W = 5$ and $W = 15$, which in turns means a perfect signal *BW* estimation. On the other hand, the *DoA*s are not correct for $W = 1$ at f_2 and f_3, where the estimation is $\tilde{\boldsymbol{\theta}} = \{-80, -59, -41, 10\}$ $[deg]$.

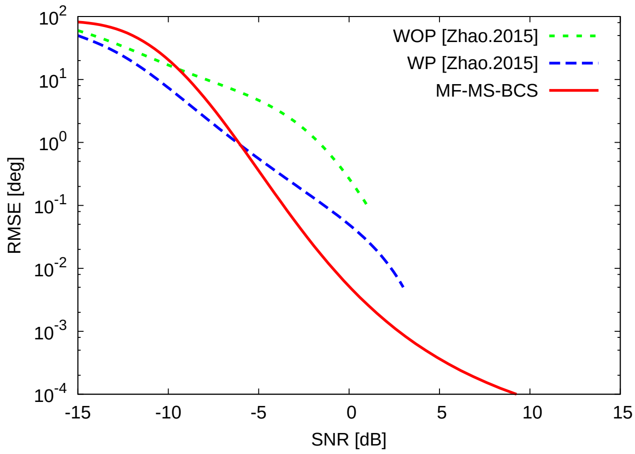

Figure 5.22: *Comparison* ($W = 64$; $M = 16$, $d = 0.5\lambda_0$; $f =[80 : 120]$ $[Hz]$, $N = 5$, $f_n =\{80, 90, 100, 110, 120\}$ $[Hz]$; $L = 2$, $\boldsymbol{\theta} = \{-10, 20\}$ $[deg]$, $SNR = [-15 : 15]\,dB$; $K = 181$, $T = 100$) - RMSE at different SNRs.

Moreover, the $MFMS - BCS$ has also been compared with [77], where two wideband signals ($\boldsymbol{\theta} = \{-10, 20\}$ $[deg]$) having equal bandwidth of 40 Hz ($f = [80 : 120]$ Hz) are impinging on a linear array of 16 elements spaced by half wavelength with respect to the maximum frequency of f_{max} =120 $[Hz]$. Each element collects 64 time domain samples with the noise level of $SNR = [-15 : 15]\,dB$. The estimated average $RMSE$ for 100 noise realizations are plotted as comparative fashion in Fig. 5.22. The $MFMS - BCS$ outperforms when

$SNR = [-5 : 15]\,dB$, although the estimated RMSE by WOP and WP [77] are slightly less in extreme noise level (e.g., $SNR = [-15 : -5]\,dB$).

Chapter 6

DoA Estimation in Cost Effective System

In this chapter, the DoA estimation problem for different sub-arrayed array is addressed with the state-of-the-art BCS approach. More specifically, $ST-BCS$ is applied for linear array in order to find out a optimum sub-array configurations in which the performance of estimation is comparable with fully populated array. For planar case, both $ST-BCS$ and $MT-BCS$ is applied. In addition, the main outcome of this work is published in [84].

6.1 Introduction

Direction-of-arrival (DoA) estimation is a part and parcel of modern radar and communication applications. Nowadays, antenna arrays often adopt a sub-arrayed architecture [120] in order to reduce the complexity and cost of the feeding network. However, the sub-arrayed architecture brings additional challenges as the array features are greatly compromised with respect to the fully populated arrays. Therefore, it is essential to analyze the performance of the DoA estimation in sub-arrayed architecture, but only few works have previously addressed this problem. For example, approaches exploiting nested arrays [121] and co-prime arrays [122] have been proposed in which the DoAs estimation has been carried out by means of the classical subspace-based estimators $MUSIC$ and $ESPRIT$. However, these techniques have their own theoretical limitations. For instance, they need (i) to a-priory know the number of incoming signals, (ii) to compute the complex co-variance matrix which is computationally demanding, and (iii) to acquire the data over multiple snapshots in order to provide a reliable estimation, not suitable for real time application.

Sparse processing [56]-[62] for signal reconstructions has received great attention since last two decades. In this framework, strategies based on the compressive sensing (CS) theory [59]-[61] have recently been introduces thanks to their effectiveness, flexibility, and computational efficiency to deal with complex engineering problems in electromagnetic [63]-[68] including antenna array synthesis [69]-[70] and imaging [71]-[75].

The BCS-based strategies have been effectively applied for $DoAs$ estimation for different purposes [78]-[84]. In this framework, strategies based on the BCS are introduced in which the data measured at the output of the sub-array ports and at a single or multiple time instant/snapshot are directly processed to estimate the signal $DoAs$. The impact on the estimation performance for different uniform and non-uniform sub-array configurations of linear and planar array are analyzed in a comparative fashion.

6.2 Mathematical Formulations

Let us consider a set of L electromagnetic plane waves arriving from unknown directions θ_l, $l = 1, ..., L$, on a linear array of M elements placed along x-axis at positions x_m, $M = 1, ..., M$, with uniform inter-element spacing d. The M array elements are grouped into Q sub-arrays, each containing N_q, $q = 1, ..., Q$ elements (Fig. 6.1). The membership of each array element to a sub-array is identified by C_m, $m = 1, ..., M$ where $C_m \in [1 : Q]$. The data collected at the output terminal of the $q-$th sub-array are mathematically expressed as:

$$Y_q = \sum_{m=1}^{M} V_m \delta_{C_m q} \quad ; \quad \delta_{C_m q} = \begin{cases} 1; & C_m = q \\ 0; & otherwise \end{cases} \tag{6.1}$$

where V_m are the OCV equivalent to fully populated array (5.2). Substituting V_m of (5.2) into (6.1) turns out to be:

$$Y_q = \sum_{m=1}^{M} \left(\sum_{l=1}^{L} s_l \hat{\mathbf{y}} \cdot \boldsymbol{\mathcal{H}} e^{j\beta x_m \sin\theta_l} + \eta_m \right) \delta_{C_m q}, \; q = 1, ..., Q. \tag{6.2}$$

Equation (6.2) can be written in matrix form as:

$$[\mathbf{Y}] = [\boldsymbol{\delta}] [\mathbf{A}(\boldsymbol{\theta})] [\mathbf{s}] + [\boldsymbol{\delta}] [\boldsymbol{\eta}] \tag{6.3}$$

where $[\mathbf{Y}] = [Y_1, Y_2, ..., Y_Q]^T \in \mathbb{C}^{Q\times 1}$ is the vector of sub-array data; $[\mathbf{s}] = [s_1, s_2, ..., s_L]^T \in \mathbb{C}^{L\times 1}$ is the signal vector; $[\boldsymbol{\eta}] = [\eta_1, \eta_2, ..., \eta_M]^T \in \mathbb{C}^{M\times 1}$ is the noise vector, $[\mathbf{A}(\boldsymbol{\theta})] = [\mathbf{a}(\theta_1), \mathbf{a}(\theta_2), ..., \mathbf{a}(\theta_L)] \in \mathbb{C}^{M\times L}$ is the steering matrix of fully populated array, and $[\boldsymbol{\delta}] =\in \mathbb{R}^{Q\times M}$ is the sub-array transformation matrix defined as

$$[\boldsymbol{\delta}] = \begin{bmatrix} \delta_{C_1 1} & \cdots & \delta_{C_M 1} \\ \vdots & \ddots & \vdots \\ \delta_{C_1 Q} & \cdots & \delta_{C_1 Q} \end{bmatrix}. \tag{6.4}$$

Equation (6.3) can be further simplified as:

$$[\mathbf{Y}] = \left[\mathbf{A}^{sub}(\boldsymbol{\theta})\right] [\mathbf{s}] + \left[\boldsymbol{\eta}^{\boldsymbol{sub}}\right] \tag{6.5}$$

where $\left[\mathbf{A}^{sub}(\boldsymbol{\theta})\right] = [\boldsymbol{\delta}] [\mathbf{A}(\boldsymbol{\theta})] \in \mathbb{C}^{Q\times L}$ is the transformed sub-arrayed steering matrix. Then the procedures described in Sect. 3.3 (sub. 3.4.1) are employed in order to apply $ST - BCS$ strategies.

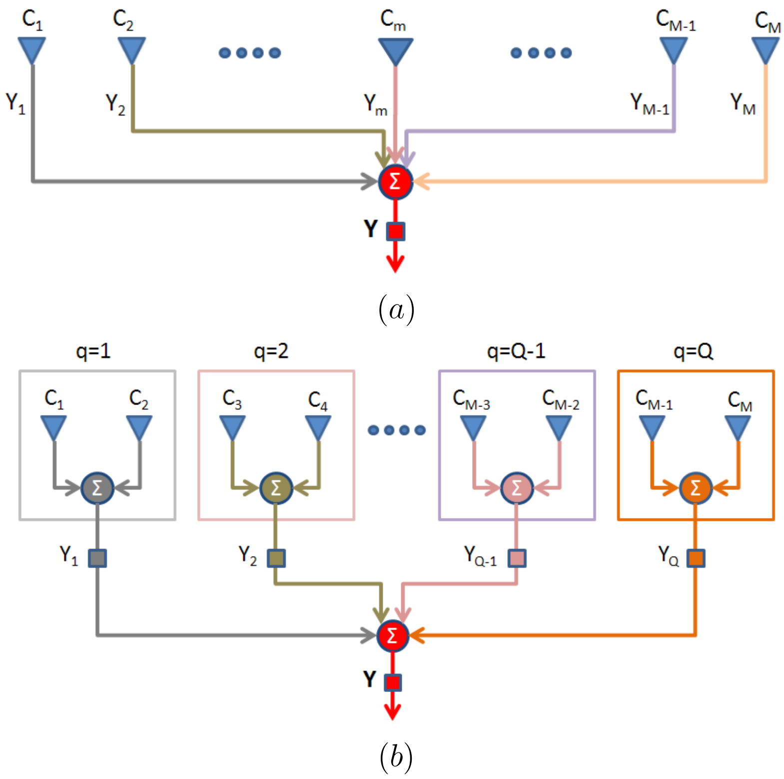

Figure 6.1: *Sketch of the array geometries - (a)* without sub-array and *(b)* with contiguous uniform sub-array of $N = 2$ elements per cluster.

Then according to the guideline of single-task BCS describe in Sect. 3.4.1, the sparse signal vector is determined by maximizing the following a-posteriori probability:

$$[\widehat{\mathbf{s}}]_{ST-BCS} = \arg\left\{\max\left[\mathcal{P}r\left(\widehat{\mathbf{s}},\, \boldsymbol{\sigma}^2,\, \mathbf{p}\,|\,\mathbf{Y}\right)\right]\right\} \tag{6.6}$$

where $\boldsymbol{\sigma}^2$ and $\mathbf{p}$ is the variance of the Gaussian noise and the BCS hyper-parameter respectively. For multi-snapshots data, the 6.5 can be written as

$$[\mathbf{V_w}] = \left[\mathbf{A}^{sub}(\boldsymbol{\theta})\right][\mathbf{s}_w] + [\boldsymbol{\eta}_w]\,,\;\; w = 1, ..., W \tag{6.7}$$

where W is the number of snapshots. Similarly the procedures described in Sect. 3.3 (sub. 3.4.2) are employed in order to apply $MT - BCS$ strategies. Then according to the guideline of single-task BCS described in Sect. 3.4.2, the sparse signal vector is determined by maximizing the following a-posteriori probability:

$$\widehat{\mathbf{s}}_{MT-BCS} = \frac{1}{W}\sum_{w=1}^{W}\left\{\arg\left[\max_{\widehat{\mathbf{s}}_w}\mathcal{P}r\left([\widehat{\mathbf{s}}_w,\, \mathbf{p}]|\,\mathbf{Y}_w\right)\right]\right\} \tag{6.8}$$

where $\widehat{\mathbf{s}}_w$, $w = 1, ..., W$, are statistically-correlated through a hyperparameter vector $\mathbf{p}$ which correlates the different snapshots.

6.3 $ST - BCS$ for Linear Sub-Arrayed Array

In order to analyze the performance of $BCS - based$ estimator, the error metric defined in [78] is considered. The first test case is devoted to analyze the performance of the estimator for signals without and with modulations. Let us consider $L = 2$ electromagnetic plane waves are impinging from directions $\theta = \{30\,, 60\}$ [deg] on a linear array of $M = \{8,\ 16,\ 24\}$ elements elements with spacing equal to half of wavelength. As for the preliminary analysis, two sub-array configurations shown in Fig. 6.1 [Fig. 6.1(a) for without sub array and Fig. 6.1(b) for with sub array of $N_q = 2$] are considered to be analyzed.

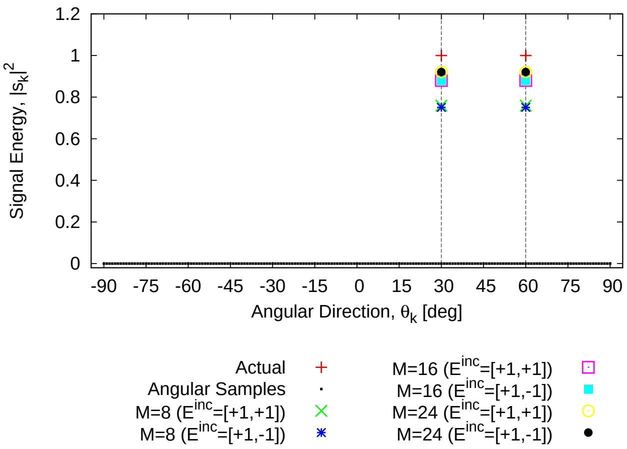

(a)

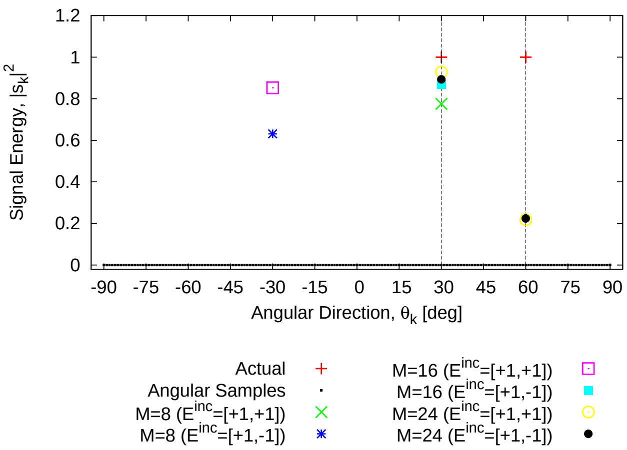

(b)

Figure 6.2: *DoAs Estimation* - Impacts of signal modulation on the estimation ($M = \{8,\ 16,\ 24\}$, $N = \{1,\ 2\}$, $d = 0.5\lambda$, $L = 2$, $E^{inc} = \{(+1,\ +1)\,,\ (+1,\ -1)\}$[V], $SNR = Noiseless$ [dB], and $K = 181$) - for *(a)* without sub-array (i.e., $N = 1$ elements) and *(b)* with contiguous uniform sub-array of $N = 2$ elements.

Table 6.1: *DoAs Estimation* - Impacts of signal modulation on the estimation ($M = \{8, 16, 24\}$, $N = \{1, 2\}$, $d = 0.5\lambda$, $L = 2$, $E^{inc} = \{(+1, +1), (+1, -1)\}$[V], $SNR = Noiseless$ [dB], and $K = 181$).

		$E^{inc} = \{+1, +1\}$		$E^{inc} = \{+1, -1\}$	
M	$\boldsymbol{\theta}\,[deg]$	$\tilde{\boldsymbol{\theta}}\,[deg]$	$RMSE\ [deg]$	$\tilde{\boldsymbol{\theta}}\,[deg]$	$RMSE\ [deg]$
8	{30, 60}	{30}	127.28	{−30}	134.16
16	{30, 60}	{−30}	134.16	{30}	127.28
24	{30, 60}	{30, 60}	0.00	{30, 60}	0.00

First of all, the impacts of modulation are analyzed. For two different sets of signal magnitude (i.e., without modulation $E^{inc} = \{+1, +1\}$[V] and with BPSK modulation $E^{inc} = \{+1, -1\}$[V]), the estimated *DoAs* for *Noiseless* scenario are shown in Fig. 6.2. In particular, Fig. 6.2 (a) plots the estimated DoAs for the fully populated array [Fig. 6.1(a)] and Fig. 6.2 (b) plots the estimated *DoAs* for the sub-array of $N_q = 2$ [Fig. 6.1(b)]. It is evident that the signal modulation has an impact on sub-array *DoA* estimation. For example, in fully populated case [Fig. 6.1(a)], the estimator perfectly retrieved the *DoAs* for all M while it is unable to estimate all *DoAs* for $M = 8$ and $M = 16$ with the sub-array geometry. However, it perfectly estimates the unknown *DoAs* with the sub-arrayed array geometry for $M = 24$ as shown in Fig. 6.2 (b) also in Tab. 6.1.

In order to extensively analyze the performance of the proposed estimator, 100 randomly generated *DoA* sets with random *BPSK* modulations are analyzed for noiseless case. In this case, the results are plotted in order to show that the percentage of number of *DoA* set belongs to any of the five *RMSE* ranges. The ranges of *RMSE* is defined as follows:

- Excellent - $RMSE = [0 : 0]$ [deg];
- Very Good - $RMSE = [0 : 1]$ [deg];
- Good - $RMSE = [1 : 10]$ [deg];
- Bad - $RMSE = [10 : 100]$ [deg];
- Worse - $RMSE = [100 : 1000]$ [deg].

Figure 6.3 shows the percentage of number *DoA* sets belonging to each of the defined category of *RMSE* ranges among 100 Monte-Carlo simulations (i.e., 100 randomly generated *BPSK* signals). It is evident that the average *RMSE* among 100 simulations belonging to the “Excellent” category (exact estimation) is estimated for 90 percent and 50 percent of the random *DoA* sets for $N = 1$

Table 6.2: *Performance Analysis* - Percentage of random DoA sets belonging to each range of RMSEs ($M = 24$, $N = \{1, 2\}$, $d = 0.5\lambda$, $L = 2$, $SNR = Noiseless$ [dB], $K = 181$, and $S = 100$ random DoA Sets) - for $T = 100$ random $BPSK$ signals.

RMSE [deg]	Minimum		Average		Maximum	
	$N = 1$	$N = 2$	$N = 1$	$N = 2$	$N = 1$	$N = 2$
0	97	66	87	46	87	46
$0-1$	0	1	4	0	0	0
$1-10$	1	4	6	8	10	2
$10-100$	0	1	1	16	0	14
$100-180$	2	28	2	30	3	38
Total	100	100	100	100	100	100

(no sub-arraying) and for $N = 2$ (with sub-arraying) respectively as shown in Fig. 6.3. The details of results for different categories are also tabulated in Tab. 6.1.

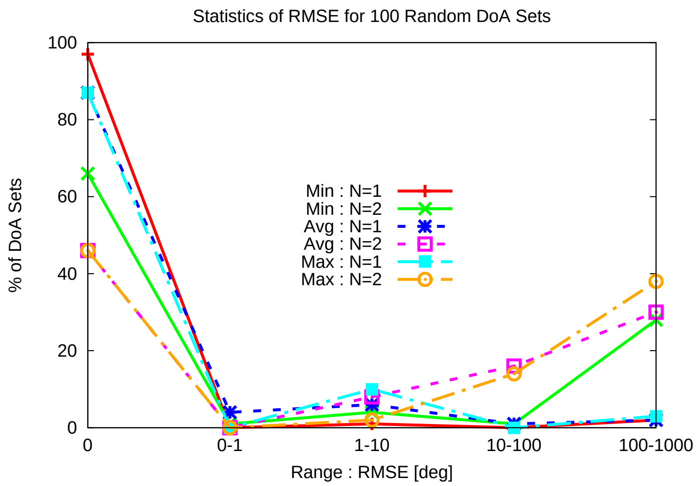

Figure 6.3: *Performance Analysis* - Percentage of random DoA sets belonging to each range of RMSEs ($M = 24$, $N = \{1, 2\}$, $d = 0.5\lambda$, $L = 2$, $SNR = Noiseless$ [dB], $K = 181$, and $S = 100$ random DoA Sets) - for $T = 100$ random $BPSK$ signals.

This is worth pointing out that the sub-arraying degrades the performance of the *DoAs* estimation. In order to further verify the impacts of contiguous uniform sub-arraying for noiseless case, an analysis is done for different number of elements in each sub-array i.e., $N = [1 : 4]$ and 100 random DoA sets of $L = 3$

signals. The percentage of the number of DoA sets belonging to each category is plotted in Fig. 6.4 [Fig. 6.4(b) for minimum, Fig. 6.4(b) for average, and Fig. 6.4(c) for maximum $RMSE$ among 100 Monte-Carlo simulations]. From Fig. 6.4, it is evident that the performance of the estimation decreases as the number of elements for each sub-array increases. From the analysis of minimum $RMSE$ of Fig. 6.4 (a), there are two DoA sets for which the minimum $RMSE$ is zero for all N. The two DoA sets are identified and they are named as "DoA Set 1" ($\theta = \{-10, 5, 13\}$ [deg]) and "DoA Set 2" ($\theta = \{-61, 34, 47\}$ [deg]).

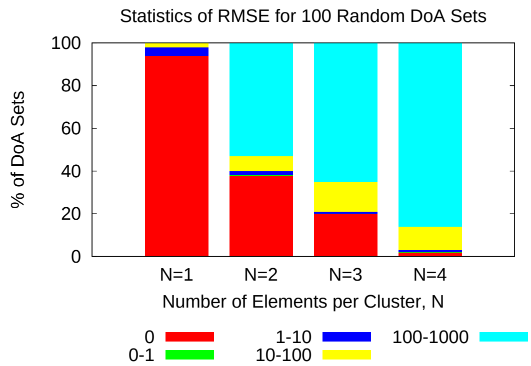

(a)

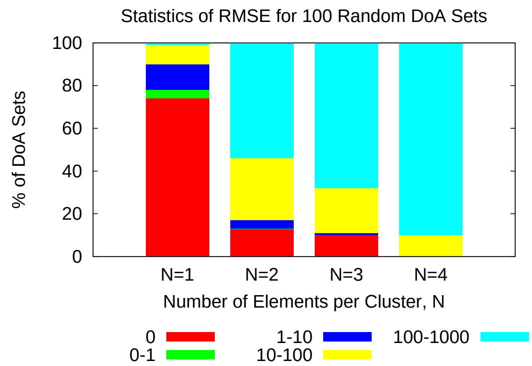

(b)

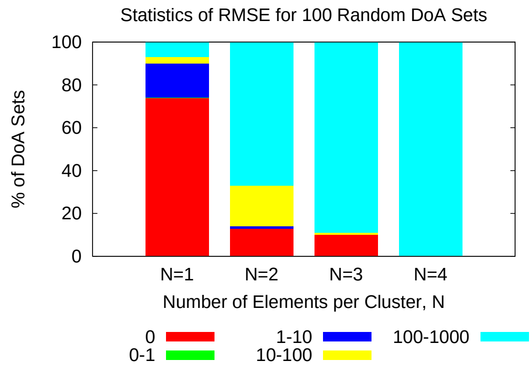

(c)

Figure 6.4: *Performance Analysis* - Percentage of random DoA sets belonging to each range of RMSEs - ($M = 24$, $N = \{1, 2, 3, 4\}$, $d = 0.5\lambda$, $L = 3$, $SNR = Noiseless$ [dB], $K = 181$ and $S = 100$ random DoA Sets) - for *(a)* minimum, *(b)* average, and *(c)* maximum RMSEs among $T = 100$ random $BPSK$ signals.

In order to verify the impacts of sub-arraying for different noisy conditions, the following analysis are done for "DoA Set 1" ($\theta = \{-10, 5, 13\}$ [deg]) and "DoA Set 2" ($\theta = \{-61, 34, 47\}$ [deg]). The performance of the estimation in terms of minimum, average, and maximum $RMSE$ for different noisy cases are shown in Fig. 6.5. It is evident that the results for two DoA sets vary with respect to different N and also $SNRs$. It is worth pointing out that the performance of the estimation for $N = 3$ is better than both $N = 2$ and $N = 4$. This is an interesting result since it is indicating that the performance of the estimation could be improved by analyzing different sub-array configurations.

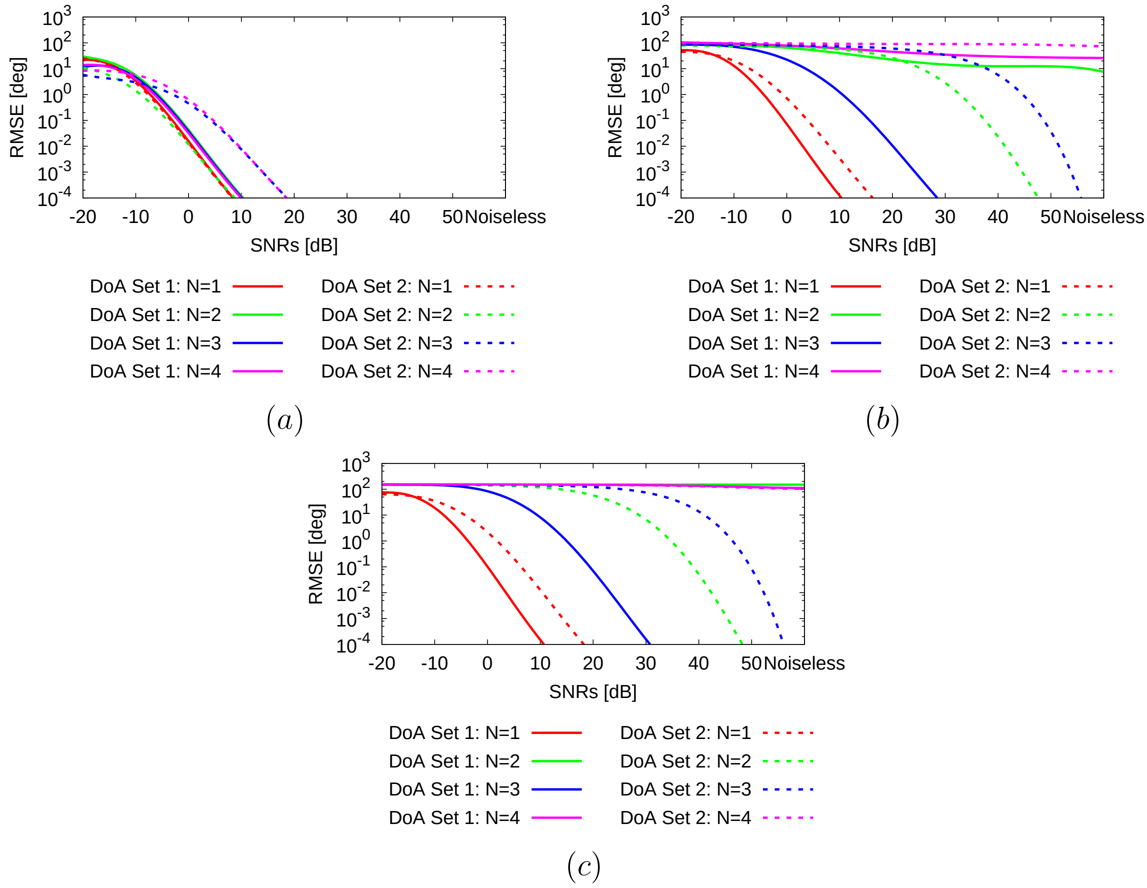

Figure 6.5: *Performance Analysis* - *SNRs* versus *RMSEs* - ($M = 24$, $N = \{1, 2, 3, 4\}$, $d = 0.5\lambda$, $L = 3$, $SNR = \{-20, ..., Noiseless\}$ [dB], $K = 181$ and $S = 2$ selected DoA Sets) - for (a) minimum, (b) average, and (c) maximum RMSEs among $T = 100$ random $BPSK$ signals.

So far, the analysis is done with the contiguous uniform sub-array. In order to analyze the performance for different sub-array configurations, the non-contiguous sub-array of Fig. 6.6 (an example is shown for $N = 2$) is considered to be analyzed for $N = \{2, 3, 4\}$. The results in terms of average $RMSE$ among 100 trials is shown in Fig. 6.7 and compared with contiguous sub-array. The non-contiguous sub-array of $N = 2$ outperforms as shown in Fig. 6.7.

Up to now, the analysis have been done for uniform contiguous and uniform non-contiguous sub-arrays. The next analysis is devoted to analyze the performance of the proposed method with non-uniform sub arrays. In order to do this, 6 non-uniform contiguous (NUC) sub-arrays as shown in Fig. 6.8 are analyzed.

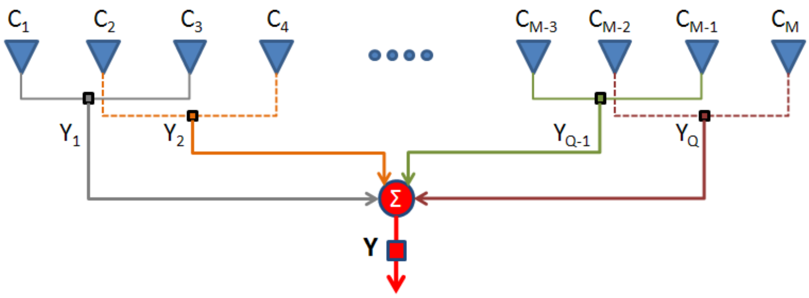

Figure 6.6: *Performance Analysis* - Sketch of the non-contiguous uniform sub-array of $N = 2$ elements per cluster.

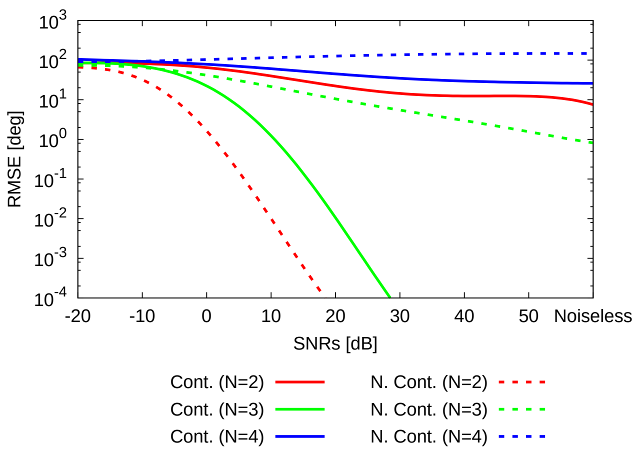

Figure 6.7: *Performance Analysis* - Contiguous versus Non-contiguous sub-array - ($M = 24$, $N = \{2, 3, 4\}$, $d = 0.5\lambda$, $L = 3$, $SNR = \{-20, ..., Noiseless\}$ [dB], and $K = 181$) - average $RMSEs$ among $T = 100$ random $BPSK$ signals.

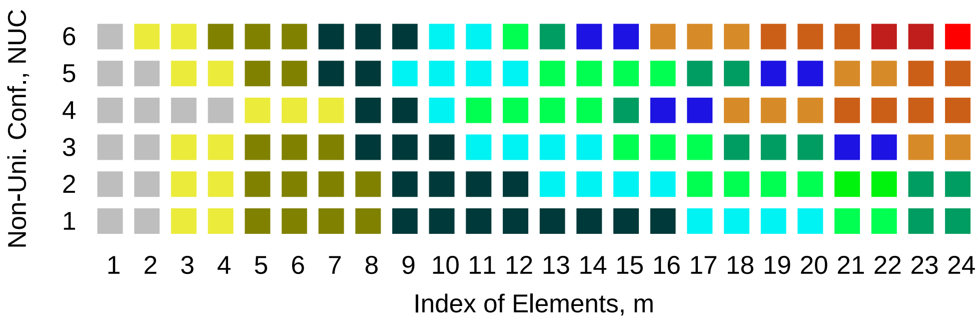

Figure 6.8: *Performance Analysis* - Manually defined six contiguous non-uniform sub-array configurations ($M = 24$, $N = \{1, 2, 3, 4\}$, and $NUC = [1 : 6]$).

The performance of the different non-uniform contiguous sub-arrays shown in Fig. 6.8 are analyzed in Fig. 6.9 for different noisy conditions and compared with the uniform contiguous sub-arrays of $N = \{1, 2, 3\}$. It is worth pointing out that the non-uniform contiguous sub-array of $NUC = 3$ outperforms than all other considered sub-array configurations. Moreover, the performance of $NUC = 3$ sub-array configuration has the similar performance as the fully populated array in Fig. 6.8 for different noisy conditions.

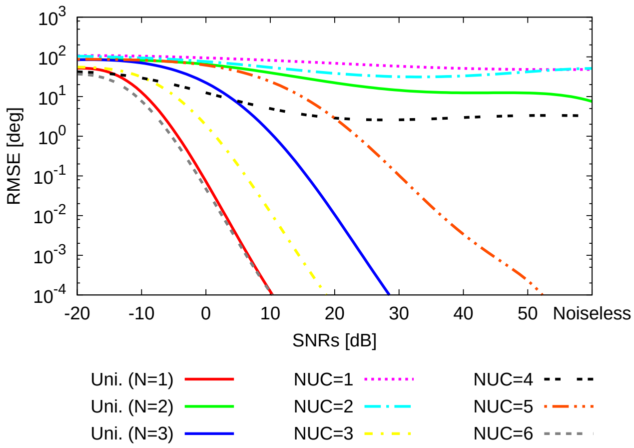

Figure 6.9: *Performance Analysis* - Contiguous uniform versus contiguous non-uniform sub-array - ($M = 24$, $N = \{1, 2, 3, 4\}$, $d = 0.5\lambda$, $L = 3$, $SNR = \{-20, ..., Noiseless\}$ [dB], and $K = 181$) - average $RMSEs$ among $T = 100$ random $BPSK$ signals.

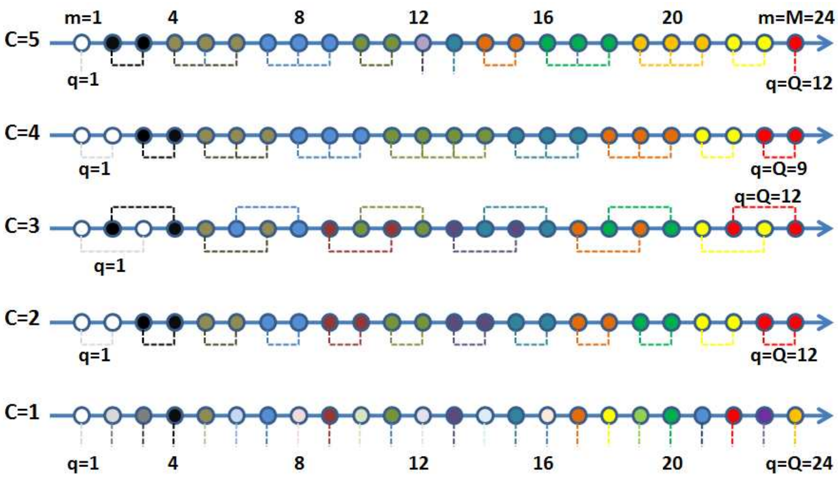

Figure 6.10: *Performance Analysis* - Sketch of the selected five configurations.

From the above analysis, it is evident that the estimation performance depends on different sub array configurations. Therefore, in order to have an extensive analysis for 100 sets of random $DoAs$, the best 5 sub-array configurations are selected based on the performance reported so far. The selected configurations are sketched in Fig. 6.11, where the configurations are indicated by the indexes of **C**. It includes fully populated array (C=1), contiguous uniform array of $N = 2$ (C=2), non-contiguous uniform array of $N = 3$ (C=3), contiguous non-uniform array of $Q = 9$ (C=4), and finally contiguous non-uniform array of $Q = 12$ (C=5).

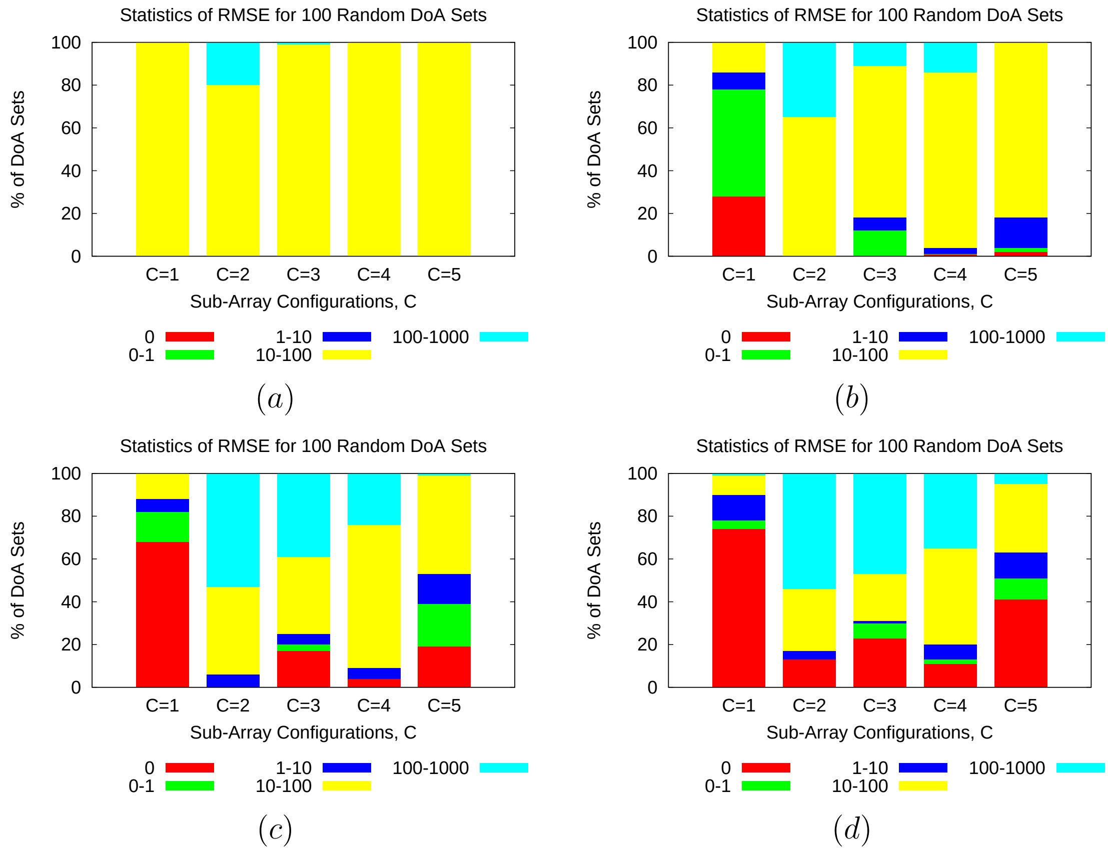

Figure 6.11: *Performance Analysis* - Percentage of random DoA sets belonging to each range of RMSEs - ($M = 24$, $N = \{1, 2, 3, 4\}$, $d = 0.5\lambda$, $L = 3$, $K = 181$ and $S = 100$ random DoA Sets) - average RMSEs among $T = 100$ random $BPSK$ signals for (a) $SNR = 0$ [dB], (b) $SNR = 10$ [dB], (c) $SNR = 20$ [dB], and (d) $SNR = Noiseless$ [dB].

Figure 6.11 shows the percentage of number DoA sets belonging to each of defined category of $RMSE$ range among 100 Monte-Carlo simulations (i.e., 100 randomly generated $BPSK$ signals) for different SNRs, $SNR = \{0,\ 10,\ 20,\ Noiseless\}$ [dB]. It is clearly evident that the estimation for all the configurations are "Bad"

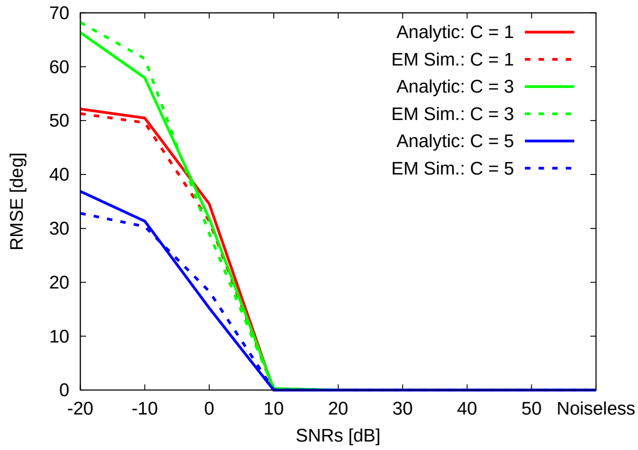

Figure 6.12: *Performance Analysis* - Performance analysis with analytic and simulated data for 3 best selected configurations - ($M = 24$, $N = \{1, 2, 3\}$, $d = 0.5\lambda$, $L = 3$, $\theta = \{-10, 5, 13\}$ [deg] $SNR = \{-20, .., 0, .., Noiseless\}$ [dB], and $K = 181$) - average RMSEs among $W = 100$ Noise realizations.

(in the range, $RMSE = [10 - 100]$ [deg]) when $SNR = 0$ [dB] as shown in Fig. 6.11 (a). It is worth pointing out that the exact estimation for the number of percentage of DoA sets are increased with the increase of $SNRs$ as shown in Fig. 6.11 (b)-(d). Although, the performance of fully populated array is higher for all the $SNRs$, the configurations C=3 and C=5 are promising.

Finally, the performance of the proposed method for the promising configurations found in previous analysis namely C=1, C=3, and C=5 are analyzed with the data collected from a commercially available EM simulator and compared with the numerically generated data. Figure 6.12 shows the average $RMSE$ among 100 Monte-Carlo simulations for different $SNRs$. It is worth pointing out that the results with the analytic and EM simulators data are approximately equal for each configuration. Another important observation is that the configuration C=5 outperforms for $\theta = \{-10, 5, 13\}$ [deg].

6.4 Analysis With Planar Sub-Arrayed Array

As for the preliminary analysis, both $ST-BCS$ and $MT-BCS$ are applied in planar sub-arrayed array. In order to analyze the performance of $BCS-based$ estimator, the error metric defined in [79] is considered. Let us assume a planar array consists of $M \times N = 36$ elements with $d = d_x = d_y = 0.5\lambda$ as shown in Fig. 6.13. For the purpose of sub-arraying, let the $M \times N$ elements are grouped into Q subarrays where the number of elements P_q for each sub-array is the same in the case of uniform sub-arraying and P_q is not equal for non-uniform case.

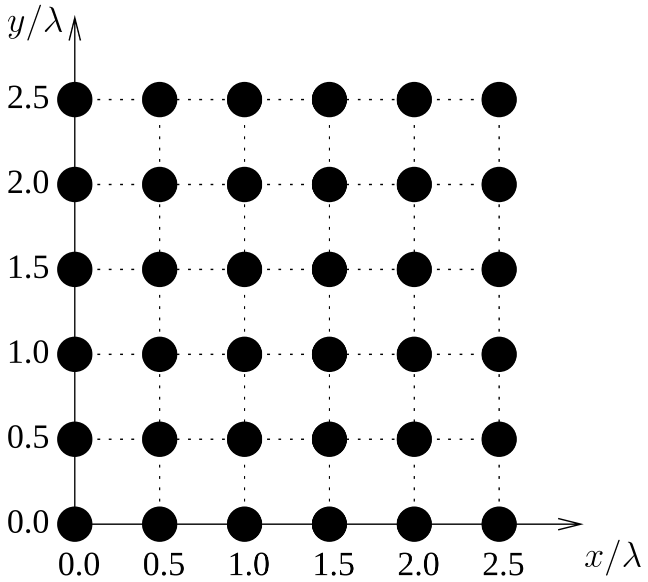

Figure 6.13: *Sketch Planar Array* - Sketch of the planar sub-arrayed array with $N = 1$.

In order to estimate the performance of BCS based methods, let us consider $L = \{1, 2, 3\}$ signals are impinging on a planar array of different sub-array configurations as shown in Fig. 6.14 from the directions $(\theta_l, \phi_l) = \{(20, 40)\}$ [deg] when $L = 1$, $(\theta_l, \phi_l) = \{(20, 40), (45, 150)\}$ [deg] when $L = 2$, and $(\theta_l, \phi_l) = \{(20, 40), (45, 150), (60, 240)\}$ [deg] when $L = 3$. The sub-array configurations in Fig. 6.14 are created manually in order to analyze the behaviour of the proposed methods. The impinging signals are randomly generated $BPSK$ signals and characterized by $SNR = \{0, 10, ..., Noiseless\}$ [dB].

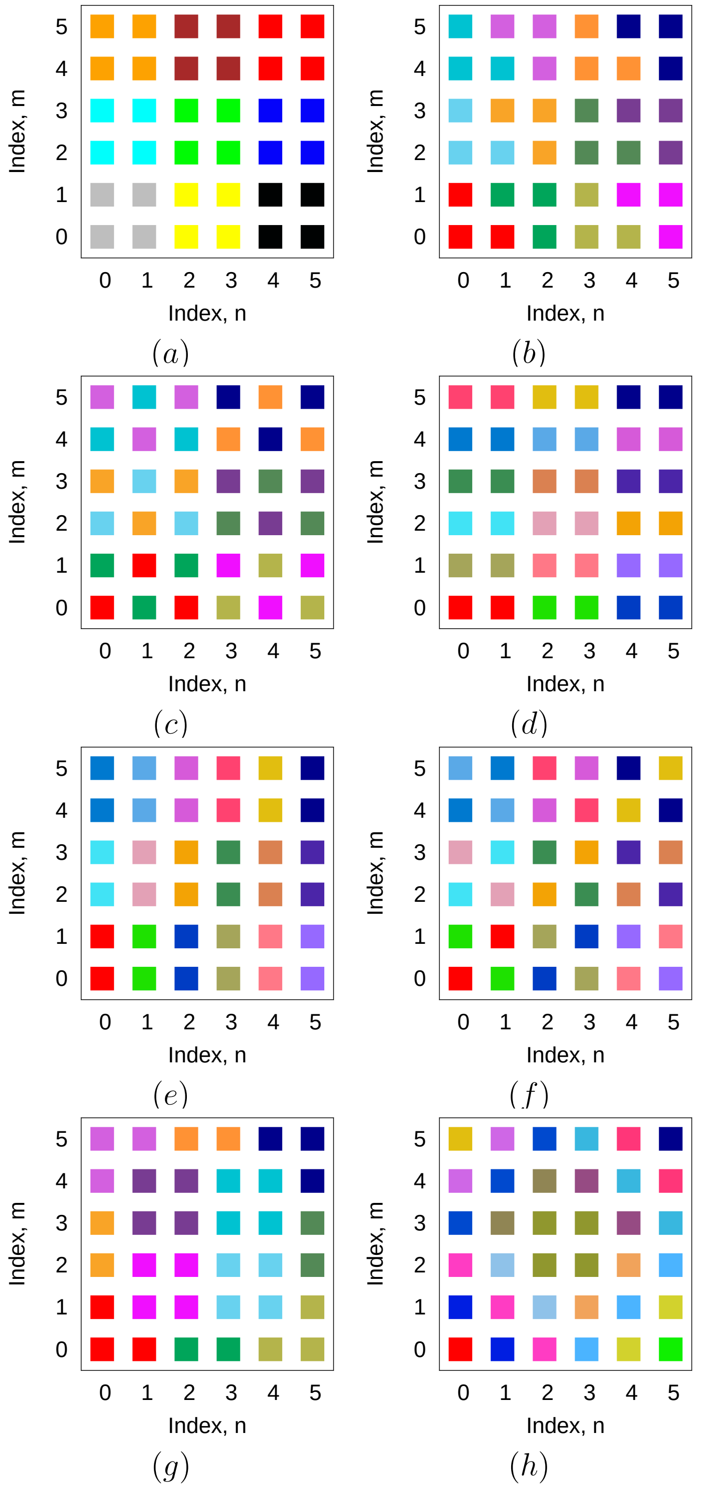

Figure 6.14: *Sub-Array Configurations* - Considered planar sub-arrayed array configurations.

The average $RMSE$ among 100 Monte-Carlo simulations for different noisy scenarios are plotted in Fig. 6.15.

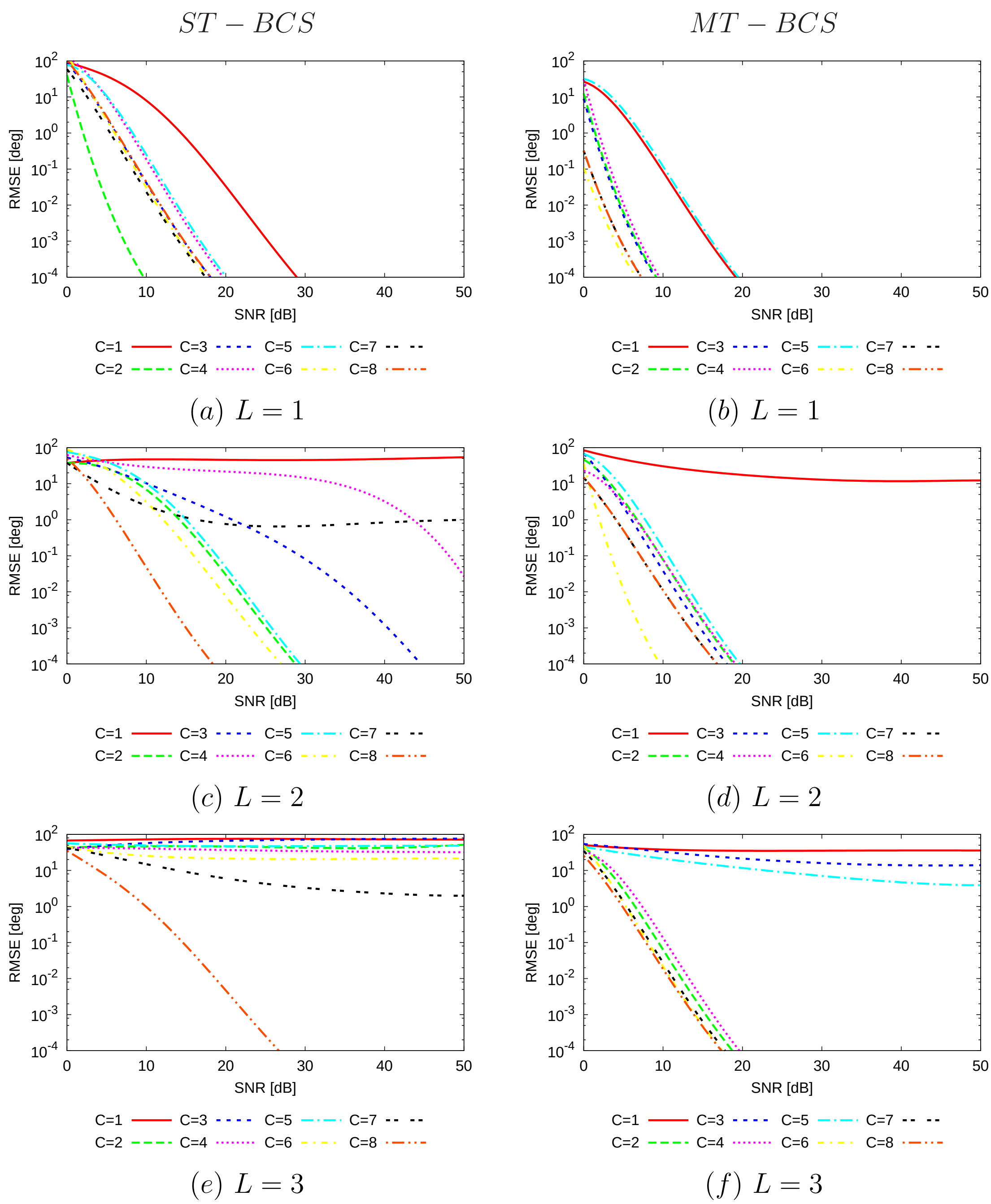

Figure 6.15: *Performance Analysis* - Performance analysis of $ST - BCS$ (left collumn) and $MT - BCS$ (left collumn) - ($M \times N = 36$, $SNR = \{0, 10, ..., Noiseless\}$ [dB] $L = \{1, 2, 3\}$, $W = 1$ ($ST - BCS$) and $W = 10$ ($MT - BCS$)) - Average $RMSE$ among $T = 100$ Monte-Carlo simulations.

The performance in-terms of average $RMSE$ for different sub-arrays are concluded as follows:

- as expected, $MT - BCS$ outperforms $ST - BCS$;
- overall, the configuration $C = 8$ outperforms irrespective of methods, number of signals, and $SNRs$;
- when $L = 2$, the configuration $C = 6$ seems promising;
- the performance of BCS for all the non-uniform cases are better than all contiguous uniform cases.

Since the configurations $C = 6$ and $C = 8$ are promising, the performance of $C = 6$ and $C = 8$ is compared with the fully populated array in Fig. 6.16.

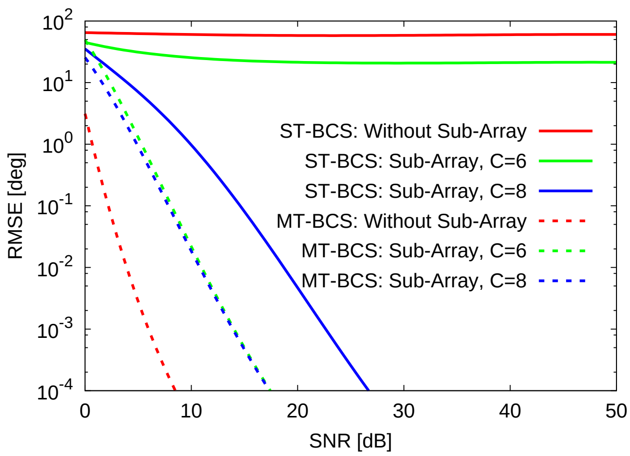

Figure 6.16: *Performance Comparison* - Fully populated versus sub-arrayed array of $C = 6$ and $C = 8$ ($M \times N = 36$, $SNR = \{0, 10, ..., Noiseless\}$ [dB] $L = 3$, $W = 1$ ($ST - BCS$) and $W = 10$ ($MT - BCS$)) - Average $RMSE$ among $T = 100$ Monte-Carlo simulations.

Chapter 7

TVCS in DoA Estimation

In this chapter, an innovative applications of $DoAs$ estimation is addressed in the CS framework. More specifically, the estimation of closely-spaced $DoAs$ or clutter is addressed using the deterministic version CS named total-variation CS ($TV - CS$), where the sparsity of the unknown is exploited in the gradient domain.

7.1 Introduction

The knowledge of the directions of the incoming signals or clutters is always advantageous for many applications as it allows the system to focus towards the directions of interest in order to enhance the system's sensitivity and to suppress the interference. In many classical and modern radars, the characterization of the clutter including its direction and size is a major functional requirement [111]. In communication, identification of clutter is necessary to suppress multi-path propagation and it is also sometimes used to mitigate the impacts of clutter itself [112, 113].

In general, the estimation of direction of clutter (DoC) is often associated as an estimation of closely spaced direction of arrivals ($DoAs$) in the sense that the clutter itself is the combination of many closely spaced sources. This point of reasoning is often adopted in order to estimate the clutter or closely separated $DoAs$ with the classical estimators. However, the resolution of the classical estimators for closely spaced $DoAs$ are limited by the physics of the problem: a massive number of antennas are required to have a very narrow beam width in order to separate the signals having narrower angular separation.

The estimation of closely spaced $DoAs$ is challenging and most of the traditional estimators failed miserably due to the physical constraint of the problem itself. Liu et al. [114] adopted a modified $MUSIC$-like subspace based estimator to address the problem in hand. The performances of other subspace-based estimators are compared in [115]. It is worth pointing out that the performance of subspace based estimators are generally limited as it is computationally demanding (i.e., required many snapshots data) and not suitable nowadays for many applications. In this context, the modern estimators based on the CS framework plays an important role: less computational burden yet robust [81, 117]. Because of its computational efficiency and the robustness in the accuracy, CS based methodologies have been successfully applied in many applied electromagnetic (EM) fields of engineering [67] including EM scattering [72], medical imaging [73], ground penetrating radar imaging [74], and antenna array synthesis [118].

In this context, Total-Variation (TV) approach is the most potential method [119]. However, [119] is based on L1-SVD and is still subject to the multiple snapshot data in order to have a reliable estimation. In this case, the clutter or closely spaced $DoAs$ can be considered as a piece-wise constant and the sparsity is exploited in the gradient domain. Finally, $TV - CS$ is adopted to efficiently estimates the closely spaced $DoAs$ with single snapshot data.

7.2 Mathematical Formulations

Let us consider a clutter occupied δ space and its center is located at ψ [deg] in the far-field of a linear array of M elements uniformly separated of spacing d along x-axis at positions x_m as shown in Fig. 7.1 (a). In order to simplify problem, assume that the clutter itself is a source of L closely spaced signals with inter-source spacing of $\Delta\theta$ [deg]. Since the clutter is in the far-field, the sources are impinging as a plane wave from θ_l, $l = 1, ..., L$ directions. Therefore, the open-circuit voltages measured at the terminal of each element is mathematically defined in (3.8). With referring to (3.8), the dimension of each parameter is therefore:

- data vector, $\mathbf{v} = [v_1, v_2, ..., v_M]^T \in \mathbb{C}^{M\times1}$;
- signal vector, $\mathbf{s} = [s_1, s_2, ..., s_L]^T \in \mathbb{C}^{L\times1}$;
- steering vector, $\mathbf{a}(\theta_l) = \left[e^{j\beta x_1 sin\theta_l}, e^{j\beta x_2 sin\theta_l}, ..., e^{j\beta x_M sin\theta_l}\right]^T \in \mathbb{C}^{M\times1}$;
- steering matrix, $A(\boldsymbol{\theta}) = [\mathbf{a}(\theta_1), \mathbf{a}(\theta_2), ..., \mathbf{a}(\theta_L)] \in \mathbb{C}^{M\times L}$;
- noise vector, $\boldsymbol{\eta} = [\eta_1, \eta_2, ..., \eta_M]^T \in \mathbb{C}^{M\times1}$.

To apply the BCS approach, the visible angular range is discretized with $K \gg L$ samples as shown in Fig. 7.1 (b) such that $A\left(\widetilde{\boldsymbol{\theta}}\right) \in \mathbb{C}^{M\times K}$ in and the DoAs of the incoming signals are assumed to belong to the set of the K directions $\widetilde{\theta}_k$, $k = 1, ..., K$. Now, the estimation problem turns out to be that of recovering the sparse signal vector $\tilde{\mathbf{s}} \in \mathbb{C}^{K\times1}$ in correspondence with the user-defined K-sampling of the angular range, $\widetilde{\boldsymbol{\theta}} = \left[\widetilde{\theta}_1, .., \widetilde{\theta}_K\right]$. The dimension of of each parameter is therefore:

- data vector, $\mathbf{v} = [v_1, v_2, ..., v_M]^T \in \mathbb{C}^{M\times1}$;
- signal vector, $\mathbf{s} = [s_1, s_2, ..., s_L]^T \in \mathbb{C}^{L\times1}$;
- steering vector, $\mathbf{a}\left(\widetilde{\theta}_l\right) = \left[e^{j\beta x_1 sin\widetilde{\theta}_l}, e^{j\beta x_2 sin\widetilde{\theta}_l}, ..., e^{j\beta x_M sin\widetilde{\theta}_l}\right]^T \in \mathbb{C}^{M\times1}$;
- steering matrix, $A\left(\widetilde{\boldsymbol{\theta}}\right) = \left[\mathbf{a}\left(\widetilde{\theta}_1\right), \mathbf{a}\left(\widetilde{\theta}_2\right), ..., \mathbf{a}\left(\widetilde{\theta}_K\right)\right] \in \mathbb{C}^{M\times K}$
- noise vector, $\boldsymbol{\eta} = [\eta_1, \eta_2, ..., \eta_M]^T \in \mathbb{C}^{M\times1}$.

However, because of the nature of the problem, the reference problem [Fig. 7.1 (a)] itself is not sparse. It is worth pointing out that, the unknown signal vector $\tilde{\mathbf{s}} \in \mathbb{C}^{K\times1}$ is a piece-wise constant function in the gradient domain and the gradient of the $\tilde{\mathbf{s}}$ is defined as:

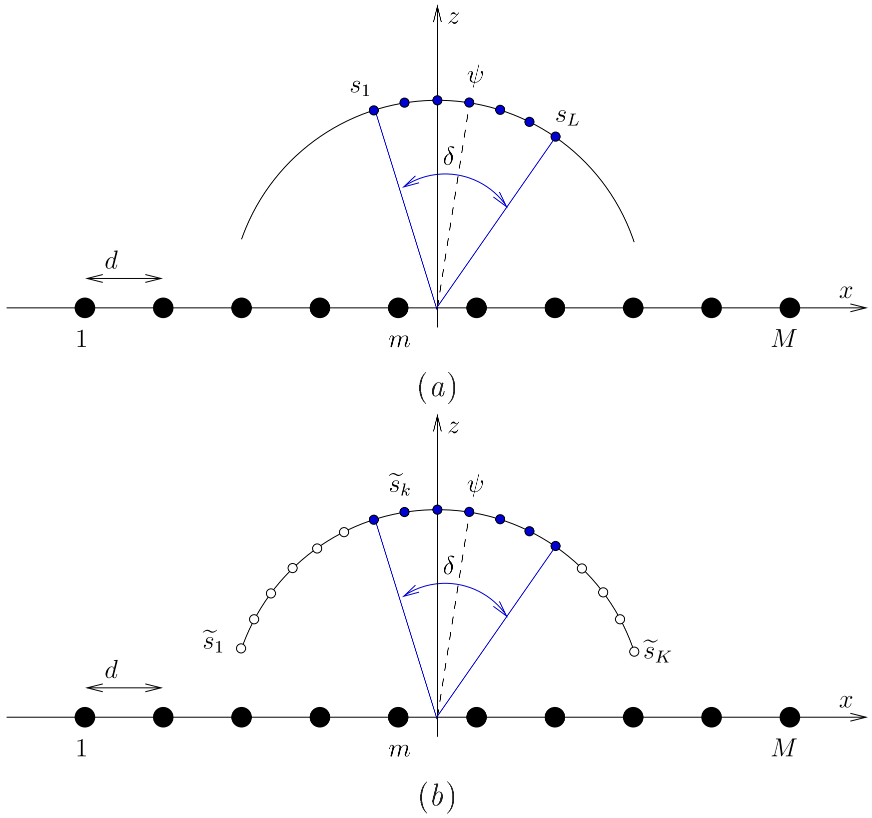

Figure 7.1: *Sketch of the Scenario* - Clutter as many closely spaced *DoAs* and linear array arrangement.

$$\nabla\tilde{\mathbf{s}} = \{\nabla\tilde{\mathbf{s}}_k = \tilde{s}_{k-1} - \tilde{s}_k;\ k = 1, \ldots, K\} \tag{7.1}$$

turns out to be non-zero only for the indexes k that belongs to the actual sources occupying the clutter. The vector $\nabla\tilde{\mathbf{s}}$ is thus a sparse vector which enables the use of $TV - CS$ strategy for finding the problem solution.

Therefore, the estimation problem of (3.8) can be reformulated in $TV - CS$ framework as

$$\mathbf{s}^{TV-CS} = arg\left[\min_{\tilde{s}}\left(\|\nabla\tilde{\mathbf{s}}\|_p + \frac{\mu}{2}\|A\tilde{\mathbf{s}} - \mathbf{V}\|_2\right)\right]\ s.t.\ \tilde{\mathbf{s}} \geq 0 \tag{7.2}$$

where $|\ .\ |_p$ is the ℓ^2-norm ($p = 2$) operator. The first term of (7.2) is the $TV - CS$ regularization term and in our case, it is isotropic. The isotropic regularization is often adopted for the signals which have sharp discontinuity (e.g., fewer zig-zag object boundaries in the case of image). In addition, the second term is commonly referred to as the fidelity term where $\mu > 0$ is the penalty parameter.

In order to solve (7.2), guidelines given in [72, 118] are adopted. First, (7.1) is written in equivalent problem with the auxiliary variable χ as follows:

$$\tilde{\boldsymbol{\chi}} = \min_{\chi} \|\nabla \boldsymbol{\chi}\|_p \quad \textit{subject to } \boldsymbol{\chi} = \nabla \tilde{\mathbf{s}} \ \textit{and } \mathbf{V} = A\tilde{\mathbf{s}} \tag{7.3}$$

where $\boldsymbol{\chi} = \{\chi_k,\, k = 1, \ldots, K\}$. Then the following augmented Lagrangian function is minimized with respect to $\tilde{\mathbf{s}}$, $\tilde{\boldsymbol{\chi}}$, $\boldsymbol{\rho}$, $\boldsymbol{\gamma}$

$$\|\tilde{\boldsymbol{\chi}}\|_p - \boldsymbol{\rho}^T (\nabla \tilde{\mathbf{s}} - \tilde{\boldsymbol{\chi}}) - \boldsymbol{\gamma}^T (A\tilde{\mathbf{s}} - \mathbf{V}) + \frac{\beta}{2}\|\nabla \tilde{\mathbf{s}} - \tilde{\boldsymbol{\chi}}\|_p^2 + \frac{\mu}{2}\|A\tilde{\mathbf{s}} - \mathbf{V}\|_p^2 \tag{7.4}$$

where $\boldsymbol{\rho}$ and $\boldsymbol{\gamma}$ are the Lagrangian multiplier vectors and β and μ are the penalty terms. The two penalty terms must be calibrated carefully in order to have reliable estimation.

7.3 Calibration of Penalty Parameters

The calibration of these two parameters must be done including all possible scenarios of a particular problem. For the problem in hand, these two parameters are optimized for the following scenarios:

- varying the number of sectors, $S = \{1, 2, 3\}$;
- varying the sectors width, $\delta = \{11, 21, 31, 41, 51\}$ [deg];
- varying the SNRs, $SNR = \{Noiseless, 20, 10, 5\}$ [dB].

For each of the above scenario, the following parameters are fixed:

Fixed Parameters Value			
Variable	Symbol	Value	Unit
Number of elements	M	20	
Inter-element spacing	d	0.5λ	[m]
Inter-source spacing	$\Delta\theta$	1	[deg]
Number of angular samples	K	181	
Number of snapshots	W	1	
Number of Trials	T	100	

The root mean square errors $RMSEs$ of all test scenarios are then averaged for each combination of β and μ. The computed average $RMSE$ for each combination of β and μ are shown in Fig. 7.2. The minimum "Average $RMSE$" is computed for $\eta = 2$ $(x = 1)$ and $\beta = 64$ $(y = 6)$ as shown in Fig 7.2 (indicated by the black square box).

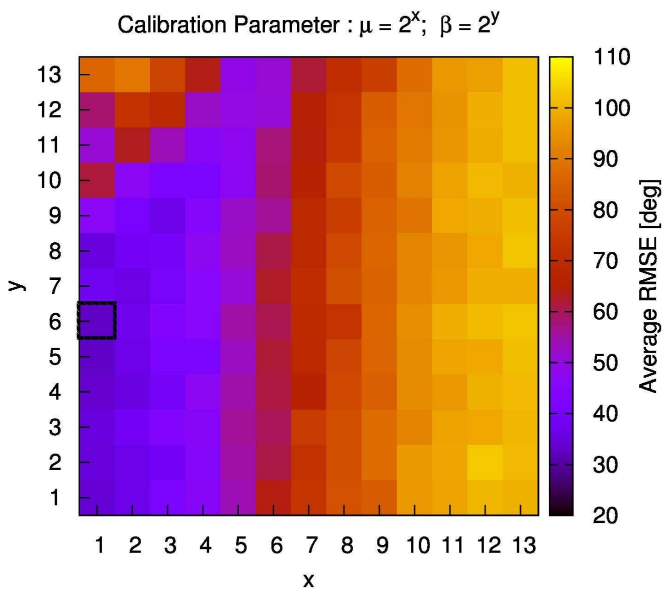

Figure 7.2: *TV-CS Calibration* - Calibration of penalty parameters η and β.

In order to show the impacts of η and β on the performance of estimation, the average $RMSE$ over all the test cases are shown in Fig. 7.3 (a) for different η and Fig. 7.3 (b) for different β. It is evident that the $RMSE$ for $SNR = 10$ [dB] dominates in the minimum "Average $RMSE$".

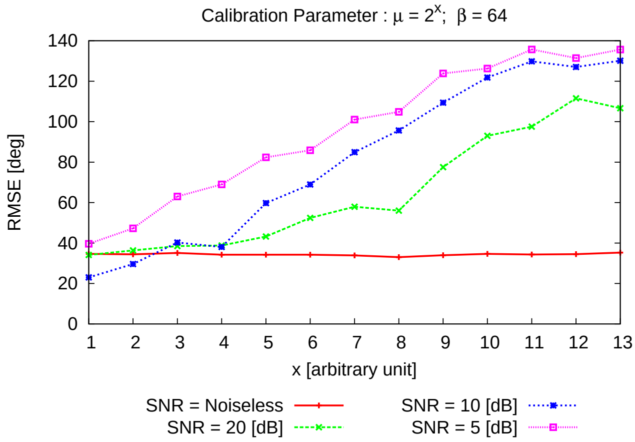

(a)

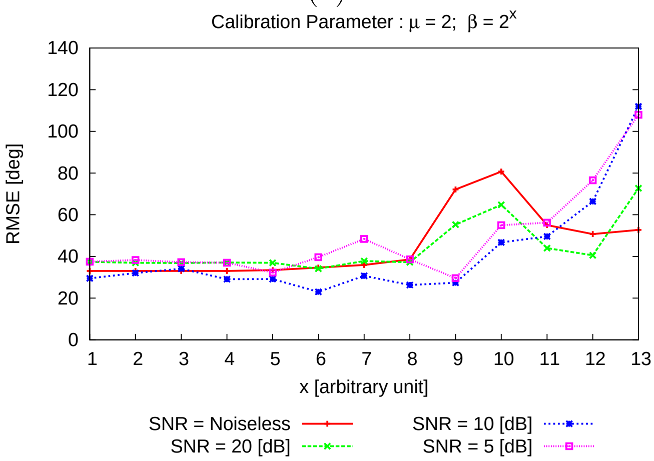

(b)

Figure 7.3: *Performance Analysis* - Impacts of penalty parameters on the estimation of *DoA* - *(a)* impacts of η for fixed β and *(b)* impacts of β for fixed η.

7.4 Numerical Validation

In order to validate the performance of $TV-CS$, three different types off clutters have been considered for analysis with $ST-BCS$ and $TV-CS$. The first case considers $S=1$ clutter which consists of $\delta=11$ [deg] clutter width with $\Delta\theta=1$ [deg] (i.e., $L=11$) and is coming from $\Psi=15$ [deg]. The second case considers $S=1$ clutter which consists of $\delta=41$ [deg] clutter width with $\Delta\theta=1$ [deg] (i.e., $L=41$) and is coming from $\Psi=0$ [deg]. The third case considers $S=2$ clutters which consists of $\delta=11$ [deg] clutter width with $\Delta\theta=1$ [deg] for each clutter (i.e., $L=22$) and is coming from $\Psi=\{27, 35\}$ [deg].

Figure 7.4 shows the best estimated $DoAs$ among $T=100$ Monte-Carlo simulations for $M=20$, $d=0.5\lambda$, $SNR=Noiseless$ [dB]), and $K=181$. It is evident that the $TV-CS$ outperforms $ST-BCS$ for all the three cases. However, as expected, $ST-BCS$ is unable to estimate the closely spaced $DoAs$. The estimated $DoAs$ are and the average $RMSE$ for each of the test case are reported in Tab. 7.1. The statistics of the performance of $TV-CS$ for closely spaced $DoAs$ among $T=100$ Monte-Carlo simulations verify that the $TV-CS$ is the promising method.

Table 7.1: *Numerical Validation* - Best estimated direction of clutter ($M=20$, $d=0.5\lambda$, $SNR=Noiseless$ [dB], and $K=181$) among $T=100$ trials.

Fig. 7.4	θ [deg]	$\tilde{\theta}^{ST-BCS}$ [deg]	$RMSE$ [deg]
*(*a*)*	$[10 : 20]$	$\{12, 15, 18, 22\}$	157.99
*(*b*)*	$[10 : 20]$	$[10 : 20]$	0.00
*(*c*)*	$[-20 : 20]$	$\{-19, -12, -11, -6, 1, 7, 18\}$	167.95
*(*d*)*	$[-20 : 20]$	$[-21 : 20]$	0.618
(e)	$[-32 : -22] \cup [30 : 40]$	$\{-28, -26, -19\} \cup \{26, 31, 36\}$	162.74
(f)	$[-32 : -22] \cup [30 : 40]$	$[-32 : -22] \cup [30 : 40]$	0.00

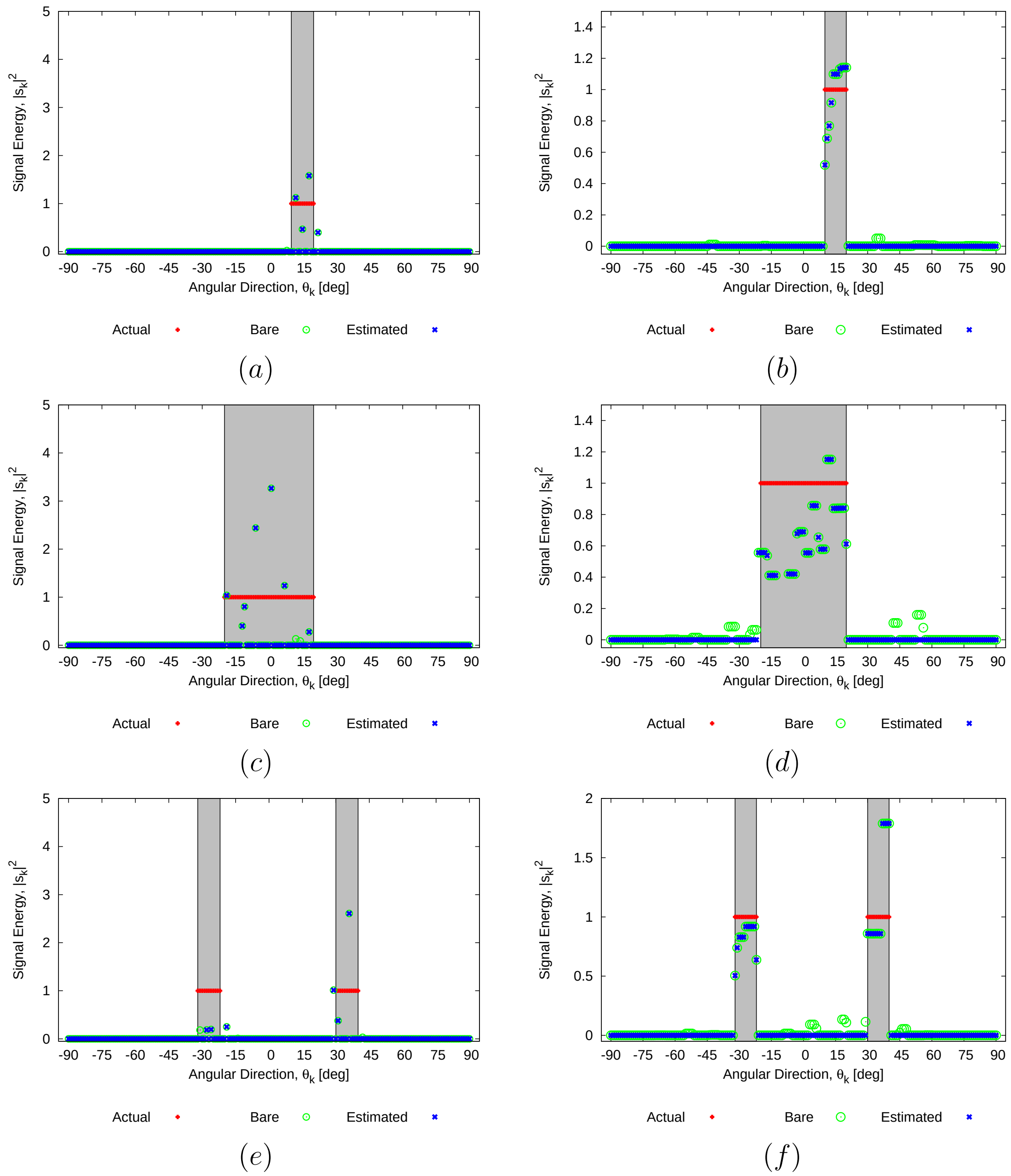

Figure 7.4: *Numerical Validation* - Best estimated direction of clutter ($M = 20$, $d = 0.5\lambda$, $SNR = Noiseless$ [dB], and $K = 181$) among $T = 100$ trials - $(a)(c)(e) ST-BCS$ $(b)(d)(f)$ versus $TV-CS$.

7.5 Performance Analysis

An extensive analysis is done in order to further verify the potentialities of the $TV - CS$ method for estimating closely spaced $DoAs$ or clutter. First of all, the impact of the positions of the clutter (fixed width of $\delta = 11$ [deg]) is analyzed where the clutters are coming from Broadside (e.g., $\Psi = 0$ [deg]), Intermediate (e.g., $\Psi = 45$ [deg]), and End-fire (e.g., $\Psi = 85$[deg]) directions. The data received at $M = 20$ elements with equal spacing of $d = 0.5\lambda$ are characterized by $SNR = [10 : Noiseless]$ [dB].

The statistics of the performance in-terms of minimum, maximum, and average $RMSE$ among $T = 100$ trials are shown in Fig. 7.5. It is evident that the performance of $TV - CS$ for any positions except end-fire is approximately equal. In addition, the $DoAs$ are perfectly reconstructed (average $RMSE = 0$ [deg]) for the broadside and the intermediate case when $SNR = 20$ [dB].

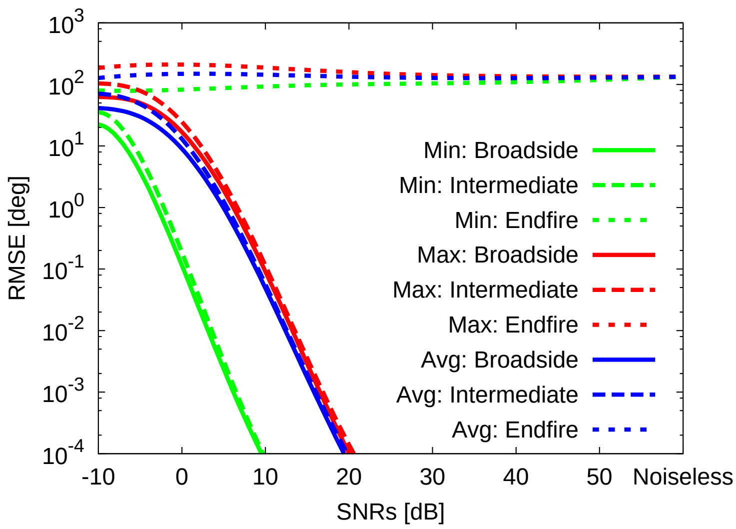

Figure 7.5: *Performance analysis* - Impacts of position of the clutter for different noisy conditions ($M = 20$, $d = 0.5\lambda$, $S = 1$, $\delta = 11$ [deg], $\Psi = \{0, 45, 85\}$[deg] ,$SNR = [10 : Noiseless]$ [dB], $K = 181$, and $T = 100$). ,

The impacts of clutter width is analyzed next for fixed clutter position $\Psi = 45$ [deg] and noise characteristics $SNR = 10$ [dB]. The statistics of the performance clearly indicate that the minimum, maximum, and average $RMSE$ are increased as the width of the clutter increased as shown in Fig. 7.6.

The impacts of the number of clutters for fixed $\delta = 11$ [deg] and $SNR = 10$ [dB] is shown in Fig. 7.7. The statistics of the performance clearly indicate that the minimum, maximum, and average $RMSE$ are increased as the width of the clutter increased as shown in Fig. 7.7. By analyzing Fig. 7.6 and Fig. 7.7, the impacts of the number of clutters are relatively higher than the width of the clutter. This is expected because the number sparsity level is decreased when number of clutters increased.

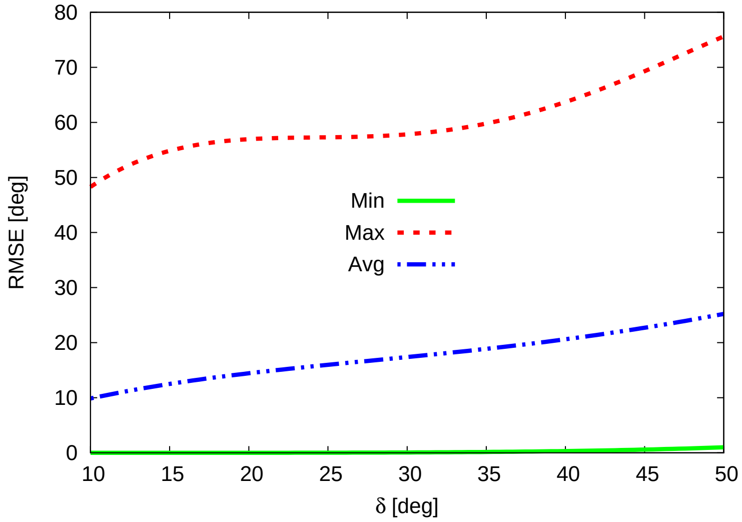

Figure 7.6: *Performance analysis* - Impacts of the clutter widths ($M = 20$, $d = 0.5\lambda$, $S = 1$, $\delta = [10 : 50]$ [deg], $\Psi = 45$ [deg] ,$SNR = 10$ [dB], $K = 181$, and $T = 100$).

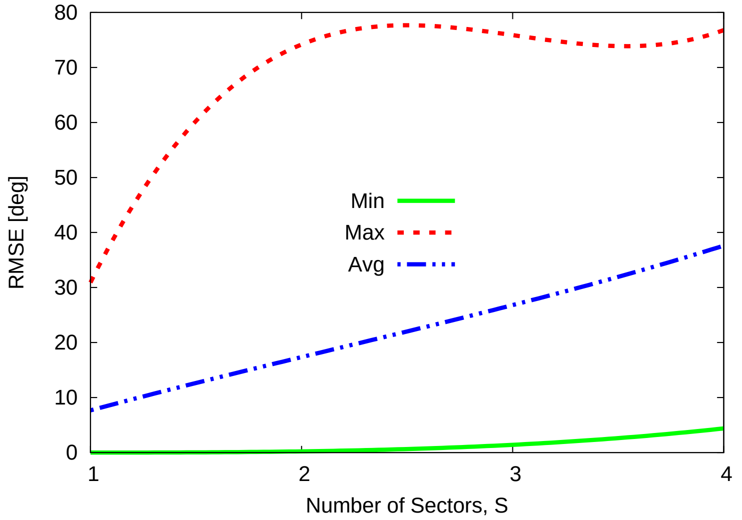

Figure 7.7: *Performance analysis* - Impacts of the number of clutters ($M = 20$, $d = 0.5\lambda$, $S = [1 ,: 4]$, $\delta = 11$ [deg], $\Psi = \{-45, -20, 30, 55\}$ [deg] ,$SNR = 10$ [dB], $K = 181$, and $T = 100$).

Finally, the impacts of the number of elements for different noisy conditions are analyzed. It is worth pointing out that the performance of the estimations are improved as the number of elements increased as shown in Fig. 7.8.

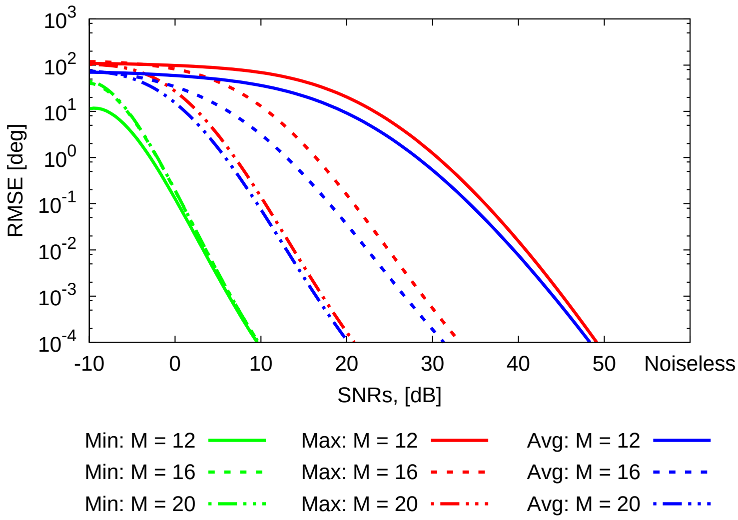

Figure 7.8: *Performance analysis* - Impacts of the number of elements ($M = \{12, 16, 20\}$, $d = 0.5\lambda$, $S = 1$, $\delta = 11$ [deg], $\Psi = 45$ [deg] ,$SNR = 10$ [dB], $K = 181$, and $T = 100$).

Chapter 8

Conclusions and Final Remarks

In this chapter, the important observations about the proposed methods and their performances for various applications have been concluded. In addition of concluding remarks, a scope of future research has been listed.

In this thesis, sparse processing of signals for $DoAs$ estimation has extensively analyzed in the framework of Compressive Sensing (CS). In particular, DoA estimation problem for different sources, systems, and applications have been formulated in the CS paradigm. In addition, the fundamental conditions related to the "Sparsity" and "Linearity" have been carefully exploited in order to apply confidently the $CS-$based methodologies. Moreover, innovative strategies based on the CS estimator for various systems and applications have been developed, validated numerically, and analyzed extensively for different scenarios considered in the literature of DoA estimation problem including signal to noise ratio, mutual coupling, polarization loss and so on. In order to analyze the performance of the proposed estimators, a standard metric called root-mean-square error ($RMSE$) has been defined. The more realistic data from EM simulators have also been considered to validate the potentialities of the proposed approaches. In order to guarantee the reliability of the estimators, the performance in terms of $RMSE$ have been analyzed with respect to different degrees-of-freedom ($DoFs$) of DoA estimation problem including number of elements, number of signals, and randomly generated signals. In nutshell, the contribution of this thesis is the development of computationally efficient, reliable, and robust $CS-$based estimators. Therefore, the proposed methods can be applied in systems having different geometries, in real time applications, and for narrow-band or wideband signals. The outcomes of this thesis are concluded as follows:

- *Chapter 2* - the state-of-the-art $DoAs$ estimation problem has been reviewed;
- *Chapter 3* - the general $DoAs$ estimation problem is formulated including electromagnetic properties like mutual coupling and polarization loss. Then the state-of-the-art CS formulation for solving $DoAs$ estimation problem have been described;
- *Chapter 4* - the performance of state-of-the-art $ST-BCS$ method has been improved significantly with the proposed $IMSA-BCS$ strategy, where the inherent parameter of BCS related to noise variances have been smartly exploited in order to refine the $ARoI$ and then iterative estimates the $DoAs$. The method has been validated with the data collected from EM simulator and also compared with the SoA methods. It has been shown that the $IMSA-BCS$ outperformed the classical estimator even with a single snapshot data and thus appropriate for real time applications;
- *Chapter 5* - the performance of state-of-the-art $MT-BCS$ method has been improved significantly with the proposed $MF-BCS$ strategy, where the signal's inherent properties (e.g., frequencies) have been exploited in order to correlate the BCS solutions over different frequency samples. Based on the time-frequency configurations, two $MF-BCS$ methods named

$MFSS - BCS$ and $MFMS - BCS$ have been proposed. It has been shown that these methods are able to estimate also the bandwidth of the incoming signals thus appropriate for cognitive radar;

- *Chapter 6* - the state-of-the-art $ST - BCS$ and $MT - BCS$ methods have been analyzed for different linear and planar sub-array geometries. It has been shown that some sub-array geometries performed same as the fully populated array. This interesting outcome opened a scope for future research in the cost effective system design for $DoAs$ estimation;

- *Chapter 7* - the state-of-the-art $TV - CS$ approach has been adapted for an innovative application. The $TVCS$ penalty parameters are optimized for different EM scenarios. It has been shown that the proposed approach is able to correctly estimate the considered clutters when for a reasonable $SNRs$.

The future research can be listed as follows:

- analysis of the performance of the proposed methods for unconventional arrays like con-formal array;

- analysis of the performance of the proposed methods for sparse arrays like random array and co-prime array;

- research on optimizing the best sub-array configurations for maximizing the performance of estimation;

- research on differential DoA estimation method.

Bibliography

[1] H. L. Van Trees, *Detection, estimation, and modulation theory, optimum array processing.* New York, USA: John Wiley & Sons, 2004.

[2] S. Chandran, *Advances in direction-of-arrival estimation.* Norwood, MA: Artech House, 2006.

[3] J. Foutz, *Narrowband direction of arrival estimation for antenna arrays.* Morgan and Claypool Publishers, 2008.

[4] T. E. Tuncer and B. Friedlander, *Classical and modern direction-of-arrival estimation.* MA, USA: Academic Press, 2009.

[5] Z. Chen, G. Gokeda, and Y. Yu, *Introduction to direction-of-arrival estimation.* Artech House, 2010.

[6] Z. Yang, J. Li, P. Stoica and L. Xie, *Sparse methods for direction-of-arrival estimation.* arXiv preprint arXiv:1609.09596, 2016.

[7] N. Dey and A. S. Ashour, *Direction of arrival estimation and localization of multi-speech sources.* Springer Publishing Company, Incorporated, 2017.

[8] Y.S. Yoon, "Direction-of-arrival estimation of wideband sources using sensor arrays," Ph.D. dissertation, Georgia Institute of Technology, 2004.

[9] N. A. H. Tayem, "Direction of arrivalangle estimation schemes for wireless communication systems," Ph.D. dissertation, Wichita State University, 2005.

[10] M. Rubsamen, "Advanced direction-of-arrival estimation and beamforming techniques for multiple antenna systems," Ph.D. dissertation, Technische Universitat Darmstadt, 2011.

[11] H. Xiong, "Antenna array geometries and algorithms for direction of arrival estimation," Ph.D. dissertation, University of Nottingham, 2013.

[12] J. F. Gu, "Direction of arrival estimation and tracking with sparse arrays," Ph.D. dissertation, Concordia University, 2013.

[13] M. Carlin, “An innovative methodological approach based on Compressive Sensing for the synthesis and control of antenna arrays," Ph.D. dissertation, University of Trento, 2013.

[14] A. A. S. Afsa, “Compressive Sensing-based estimation of direction of arrival in antenna arrays,” Ph.D. dissertation, Concordia University, 2017.

[15] J. Li, “Investigation on near-field source localization and the corresponding applications,” Ph.D. dissertation, Universite de Nantes, 2017.

[16] Marinho, “Array processing techniques for direction of arrival estimation, communication, and localization in vehicular and wireless sensor networks,” Ph.D. dissertation, Halmstad University, 2018.

[17] H. Krim and M. Viberg, “Two decades of array signal processing research: the parametric approach," *IEEE Signal Process. Mag.*, vol. 13, no. 4, pp. 67-94, July 1996.

[18] L. C. Godara, “Limitations and capabilities of directions-of-arrival estimation techniques using an array of antennas: a mobile communications perspective," *Proc. of International Symposium on Phased Array Systems and Technology*, Boston, MA, USA, pp. 327-333, 1996.

[19] B. Li, Y. Zou and Y. Zhu, “Direction estimation under compressive sensing framework: A review and experimental results," *2011 IEEE International Conference on Information and Automation*, Shenzhen, pp. 63-68, 2011.

[20] B. Liao and S. C. Chan, “A review on direction finding in partly calibrated arrays," *2014 19th International Conference on Digital Signal Processing*, Hong Kong, pp. 812-816, 2014.

[21] Q. Shen, W. Liu, W. Cui, and S. Wu, “Underdetermined DOA estimation under the compressive sensing framework: A Review,” *IEEE Access*, vol. 4, pp. 8865-8878, 2016.

[22] N. Dey, A. S. Ashour, F. Shi and R. S. Sherratt, “Wireless capsule gastrointestinal endoscopy: direction-of-arrival estimation based localization survey," *IEEE Reviews in Biomedical Engineering*, vol. 10, pp. 2-11, 2017.

[23] C. Rascon, I. Meza, “Localization of sound sources in robotics: A review" *Robot. Auton. Syst.*, vol. 96, pp. 184-210, 2017.

[24] E. Aboutanios, A. Hassanien, A. El-Keyi, Y. Nasser, and S. A. Vorobyov, “Advances in DOA estimation and source localization,” *International Journal of Antennas and Propagation*, vol. 2017, Article ID 1352598, 3 pages, 2017.

[25] F. Wang, L. Xin and X. Mao, "Multidimensional parameter estimation for electromagnetic sources with diversely polarized sensor array - A review," *8th IEEE Annual Information Technology, Electronics and Mobile Communication Conference (IEMCON)*, Vancouver, BC, pp. 343-347, 2017.

[26] A. Massa, M. Bertolli, G. Gottardi, A. Hannan, D. Marcantonio, G. Oliveri, A. Polo, F. Robol, P. Rocca, and F. Viani, "Compressive sensing as applied to antenna arrays: synthesis, diagnosis, and processing," *2018 IEEE International Symposium on Circuits & Systems (ISCAS 2018)*, Firenze, Italy, pp. 1-5, May 27-30, 2018.

[27] K. Wu, W. Ni, T. Su, R. P. Liu and Y. J. Guo, "Recent breakthroughs on angle-of-arrival estimation for millimeter-wave high-speed railway communication," *IEEE Commun. Mag.*, vol. 57, no. 9, pp. 57-63, Sep. 2019.

[28] Z. Chen, "Review of direction of arrival estimation algorithms for partial discharge localisation in transformers," *IET Sci. Meas. Technol.*, vol. 13, no. 4, pp. 529-535, 6 2019.

[29] P. Rocca, M. A. Hannan, and G. Oliveri, "Advanced real-time strategies for direction finding in rapidly changing scenario," *2019 IEEE International Conference on Microwaves, Communications, Antennas and Electronic Systems (COMCAS)*, Tel-Aviv, 2019.

[30] R. O. Schmidt, "Multiple emitter location and signal parameter estimation," *IEEE Trans. Antennas Propag.*, vol. 34, no. 3, pp. 276-280, Mar. 1986.

[31] B. D. Rao, and K. V. S. Hari, "Performance analysis of Root-Music," *IEEE Trans. Acoust., Speech, Signal Process.*, vol. 37, no. 12, pp. 1939-1949, Dec. 1989.

[32] P. Stoica, A. Nehorai, "MUSIC maximum likelihood and Cramer-Rao bound", *IEEE Trans. Acoust., Speech, Signal Process.*, vol. 37, no. 5, pp. 720-741, May 1989.

[33] A. Swindlehurst and T. Kailath, "A performance analysis of subspace-based methods in the presence of model errors. I. The MUSIC algorithm," *IEEE Trans. Signal Process.*, vol. 40, no. 7, pp. 1578-1774, Jul. 1992.

[34] Y. Zhang and B. P. Ng, "MUSIC-Like DOA Estimation without estimating the number of sources," *IEEE Trans. Signal Process.*, vol. 58, no. 3, pp. 1668-1676, March 2010.

[35] K. V. Rangarao and S. Venkatanarasimhan, "gold-MUSIC: A variation on MUSIC to accurately determine peaks of the spectrum," *IEEE Trans. Antennas Propag.*, vol. 61, no. 4, pp. 2263-2268, April 2013.

[36] X. Huang and B. Liao, "One-Bit MUSIC," *IEEE Signal Process. Lett.*, vol. 26, no. 7, pp. 961-965, July 2019.

[37] F.Yan, X. Li, C.Chen, and M.Jin, "Sector unitary MUSIC," *Signal Process.*, vol. 168, 2020.

[38] R. Roy and T. Kailath, "ESPRIT-Estimation of signal parameters via rotational invariance techniques," *IEEE Trans. Acoust., Speech, Signal Process.*, vol. 37, no. 7, pp. 984-995, Jul. 1989.

[39] B. Otterstern, M. Viberg and T. Kailath, "Performances analysis of the total least squares ESPRIT algorithm," *IEEE Trans. Signal Process.*, vol. 39, no. 5, pp. 1122-1135, May 1991.

[40] M. D. Zoltowski, M. Haardt, and C. P. Mathews, "Closed-form 2-D angle estimation with rectangular arrays in element space or beamspace via unitary ESPRIT," *IEEE Trans. Signal Process.*, vol. 44, no. 2, pp. 316-328, Feb. 1996.

[41] F. Han and X. Zhang, "An ESPRIT-like algorithm for coherent DOA estimation," *IEEE Antennas Wirel. Propag. Lett.*, vol. 4, pp. 443-446, 2005.

[42] F. Gao and B. Gershman, "A generalized ESPRIT approach to direction-of-arrival estimator," *IEEE Signal Process. Lett.*, vol. 12, no. 3, pp. 254-257, Mar. 2005.

[43] A. Kuchar, M. Tangemann and E. Bonek, "A real-time DOA-based smart antenna processor," *IEEE Trans. Veh. Technol.*,vol. 51, no. 6, pp. 1279-1293, Nov. 2002.

[44] I. Ziskind, M. Wax, "Maximum likelihood localization of multiple sources by alternating projection", *IEEE Trans. Acoust., Speech, Signal Process.*, vol. 36, pp. 1553-1560, Oct. 1988.

[45] P. Stoica, K. C. Sharman, "Maximum likelihood methods for direction-of-arrival estimation", *IEEE Trans. Acoust., Speech, Signal Process.*, vol. 38, pp. 1132-1143, July 1990.

[46] P. Stoica and A. B. Gershman, "Maximum-likelihood DOA estimation by data-supported grid search," *IEEE Signal Process. Lett.*, vol. 6, no. 10, pp. 273-275, Oct. 1999.

[47] A.Olfat, S. N. Esfahani, "A new signal subspace processing for DOA estimation," *Signal Process.*, vol. 84, issue. 4, pp. 721-728, 2004.

[48] J. Kim, S. Moon, D. S. Han and M. Cho, "Fast DOA estimation algorithm using pseudocovariance matrix," *IEEE Trans. Antennas Propag*, vol. 53, no. 4, pp. 1346-1351, April 2005.

[49] C. J. Huang, "Fast DOA estimation algorithm based on acombination of an orthogonal projection and noise pseudo-eigenvector approach," *ISRN Signal Processing*, vol. 2011, Article ID 751670, 8 pages, 2011.

[50] Y. Lin and W. Liao, "A real-time/low-cost DOA estimation system based on Rotman lens array antenna," *IEEE 5th Asia-Pacific Conference on Antennas and Propagation (APCAP)*, Kaohsiung, 2016, pp. 81-82.

[51] A. H. El Zooghby, C. G. Christodoulou, and M. Georgiopulos, "Perfomance of radial-basis function networks for direction of arrival estimation with antenna arrays," *IEEE Trans. Antennas Propag.*, vol. 45, no. 11, pp. 1611-1617, Nov. 1997.

[52] A. H. El Zooghby, C. G. Christodoulou, and M. Georgiopulos, "A neural network-based smart antenna for multiple source tracking," *IEEE Trans. Antennas Propag.*, vol. 48, no. 5, pp. 768-776, May 2000.

[53] M. Pastorino and A. Randazzo, "The SVM-based smart antenna for estimation of the directions of arrival of electromagnetic waves," *IEEE Trans. Antennas Propag.*, Vol 55, no. 6, pp. 1918-1925, Dec. 2006.

[54] A. Randazzo, M. A. Abou-Khousa, M. Pastorino, and R. Zoughi, "Direction of arrival estimation based on support vector regression: Experimental validation and comparison with MUSIC," *IEEE Antennas Wireless Propag. Lett.*, vol. 6, pp. 379-382, 2007.

[55] M. Donelli, F. Viani, P. Rocca, and A. Massa, "An innovative multiresolution approach for DOA estimation based on a support vector classification," *IEEE Trans. Antennas Propag.*, vol. 57, no. 8, pp. 2279-2292, Aug. 2009.

[56] S. M. E. Tipping, "Sparse Bayesian learning and the relevance vector machine," *J. Machine Learning Res.*, vol. 1, pp. 211-244, 2001.

[57] D. Malioutov, M. Cetin, and A. S. Willsky, "A sparse signal reconstruction perspective for source localization with sensor arrays," *IEEE Trans. Signal Process.*, vol. 53, no. 8, pp. 3010-3022, Aug. 2005.

[58] D. Model and M. Zibulevsky, "Signal reconstruction in sensor arrays using sparse representations," *Signal Proc.*, vol. 86, no. 3 , pp. 624-638, Mar. 2006.

[59] R. G. Baraniuk, "Compressive sampling," *IEEE Signal Process. Mag.*, vol. 24, no. 4, pp. 118-124, Jul. 2007.

[60] E. J. Candes and M. B. Wakin, "An introduction to compressive sampling," *IEEE Signal Process. Mag.*, vol. 25, no. 2, pp. 21-30, Mar. 2008.

[61] S. Ji, Y. Xue, and L. Carin, “Bayesian compressive sensing,” *IEEE Trans. Signal Process.*, vol. 56, no. 6, pp. 2346-2356, Jun. 2008.

[62] Z. Zhang and B. D. Rao, “Sparse signal recovery with temporally correlated source vectors using sparse Bayesian learning,” *IEEE J. Selected Topics Signal Proc.*, vol. 5, no. 5, pp. 912-926, Sep. 2011.

[63] M. D. Migliore and D. Pinchera, “Compressed sensing in electromagnetics: Theory, applications and perspectives," Proc. 5th European Conf. Antennas Propag. (EUCAP), Rome, 2011, pp. 1969-1973.

[64] G. Oliveri, P. Rocca and A. Massa, "Compressive sensing as applied to Electromagnetics: Advances, comparisons, and applications," 2013 7th European Conference on Antennas and Propagation (EuCAP), Gothenburg, 2013, pp. 1523-1526.

[65] G. Oliveri and A. Massa, "Compressive Sensing in electromagnetics: Theoretical foundations, recent advances, and applicative guidelines," *The 8th European Conference on Antennas and Propagation (EuCAP 2014)*, The Hague, 2014, pp. 1243-1246.

[66] A. Massa, "Compressive sensing - basics, state-of-the-art, and advances in Electromagnetic engineering," 2015 9th European Conference on Antennas and Propagation (EuCAP), Lisbon, 2015, pp. 1-4.

[67] A. Massa, P. Rocca, and G. Oliveri, “Compressive Sensing in electromagnetics - A review,” *IEEE Antennas Propag. Mag.*, vol. 57, no. 1, pp. 224-238, 2015.

[68] A. Massa, G. Oliveri, N. Anselmi and L. Poli, "Compressive Sensing as applied to Electromagnetics - challenges, solutions, and future trends," *2016 10th European Conference on Antennas and Propagation (EuCAP)*, Davos, 2016, pp. 1-4.

[69] G. Oliveri, and A. Massa, “Bayesian compressive sampling for pattern synthesis with maximaly sparse non-uniform linear arrays,” *IEEE Trans. Antennas Propag.*, vol. 59, no. 2, pp. 467-481, Feb. 2011.

[70] G. Oliveri, P. Rocca, and A. Massa, “Reliable diagnosis of large linear arrays - A Bayesian compressive sensing approach,” *IEEE Trans. Antennas Propag.*, vol. 60, no. 10, pp. 4627-4636, Oct. 2012.

[71] G. Oliveri, P. Rocca, and A. Massa, “A Bayesian compressive sampling-based inversion for imaging sparse scatterers,” *IEEE Trans Geosci. Remote Sens.*, vol. 49, no. 10, pp. 3993-4006, Oct. 2011.

[72] G. Oliveri, N. Anselmi, and A. Massa, “Compressive sensing imaging of non-sparse 2D scatterers by a total-variation approach within the Born approximation,” *IEEE Trans. Antennas Propag.*, vol. 62, no. 10, pp. 5157-5170, Oct. 2014.

[73] G. Oliveri, L. Poli, N. Anselmi, M. Salucci, and A. Massa, “Compressive sensing-based Born iterative method for tomographic imaging,” *IEEE Tran. Microw. Theory Techn.*, vol. 67, no. 5, pp. 1753-1765, May 2019.

[74] M. Salucci, A. Gelmini, L. Poli, G. Oliveri, and A. Massa, “Progressive compressive sensing for exploiting frequency-diversity in GPR imaging,” *Journal of Electromagnetic Waves and Applications*, vol. 32, no. 9, pp. 1164-1193, 2018.

[75] N. Anselmi, G. Oliveri, M. A. Hannan, M. Salucci, and A. Massa, "Color compressive sensing imaging of arbitrary-shaped scatterers," *IEEE Trans. Microw. Theory Techn.*, vol. 65, no. 6, pp. 1986-1999, June 2017.

[76] M. M. Hyder and K. Mahata, “Direction-of-arrival estimation using a mixed ℓ_{2-0} norm approximation,” *IEEE Trans Signal Process.*, vol. 58, no. 9, pp. 4647-4655, Sep. 2010.

[77] G. Zhao, G. Shi, F. Shen, X. Luo, and Y. Niu, “A sparse representation-based DOA estimation algorithm with separable observation model,” *IEEE Antennas Wireless Propag. Lett.*, vol. 14, pp. 1586-1589, 2015.

[78] M. Carlin, P. Rocca, G. Oliveri, F. Viani, and A. Massa, “Directions-of-arrival estimation through Bayesian Compressive Sensing strategies,” *IEEE Trans. Antennas Propag.*, vol. 61, no. 7, pp. 3828-3838, July 2013.

[79] M. Carlin, P. Rocca, G. Oliveri, and A. Massa, “Bayesian compressive sensing as applied to directions-of-arrival estimation in planar arrays,” *J. Electrical Comput. Eng.*, pp. 1-12, 2013 (Article ID 245867).

[80] M. Carlin, P. Rocca, F. Viani, G. Oliveri, and A. Massa, “Multi-resolution BCS-based approach for DoA estimation,” in *IEEE International Symposium Antennas Propagation and USNC/URSI National Radio Science Meeting*, Vancouver, BC, Canada, 2015, pp. 1074-1075.

[81] P. Rocca, M. A. Hannan, M. Salucci, and A. Massa, “Single-snapshot DoA estimation in array antennas with mutual coupling through a multi-scaling Bayesian Compressive Sensing strategy,” *IEEE Trans. Antennas Propag.*, vol. 65, no. 6, pp. 3203-3213, Jun. 2017.

[82] M. A. Hannan, N. Anselmi, G. Oliveri and P. Rocca, "Joint DoA and bandwidth estimation of unknown signals through single snapshot data and MT-BCS approach," *2017 IEEE AP-S International Symposium on*

Antennas and Propagation & USNC/URSI National Radio Science Meeting, San Diego, CA, July 9-14, 2017.

[83] M. A. Hannan, N. Anselmi, G. Oliveri and P. Rocca, "Robust BCS-based direction-of-arrival and bandwidth estimation of unknown signals for cognitive radar," *2018 IEEE AP-S International Symposium on Antennas and Propagation & USNC/URSI National Radio Science Meeting*, Boston, Massachusetts, 8-13 July 2018.

[84] M. A. Hannan and P. Rocca, "Directions-of-Arrival estimation in linear sub-arrayed array through Compressive Sensing," 2019 *IEEE AP-S International Symposium on Antennas and Propagation & USNC/URSI National Radio Science Meeting*, Atlanta, Georgia, 7-12 July 2019.

[85] G. Han, L. Wan, L. Shu, N. Feng, "Two novel DOA estimation approaches for real-time assistant calibration systems in future vehicle industrial," *IEEE Systems J.*, vol. 99, pp. 1-12, Jun. 2015.

[86] R. S. Elliott, *Antenna Theory and Design*. Hoboken, NJ: John Wiley & Sons, 2003.

[87] R. J. Mailloux, *Phased Array Antenna Handbook*. Norwood, MA: Artech House, 2005.

[88] R. S. Adve and T. K. Sarkar, "Compensation for the effects of mutual coupling on direct data domain adaptive algorithms", *IEEE Trans. Antennas Propag.*, vol. 48, no. 1, pp. 86-94, Jan. 2000.

[89] R. F. Harrington, *Field Computation by Moment Methods*. Piscataway, NJ: IEEE Press, 1993.

[90] C. A. Balanis, *Antenna Theory. Analysis and Design*. Hoboken, NJ: John Wiley & Sons, 2005.

[91] H. Duan, "MSM-FOCUSS for distributed compressive sensing and wideband DoA estimation," *19th International Conference on Digital Signal Processing*, Hong Kong, pp. 400-403, 2014.

[92] A. Chaturvedi and H. H. Fan, "Compressive wideband direction of arrival estimation," *38th International Conference on Telecommunications and Signal Processing (TSP)*, Prague, pp. 1-5, 2015.

[93] Q. Shen, W. Liu, W. Cui, S. Wu, Y. D. Zhang and M. G. Amin, "Focused compressive sensing for underdetermined wideband DoA estimation exploiting high-order difference coarrays," *IEEE Signal Processing Letters*, vol. 24, no. 1, pp. 86-90, Jan. 2017.

[94] Y. Wang, X. Duan, Daxin Tian, J. Zhou, Y. Lu, and G. Lu, "A Bayesian compressive sensing vehicular location method based on three-dimensional radio frequency," *Int. J. Distributed Sens. Netw.*, pp. 1-13, 2014 (Article ID 483613).

[95] G. Su and M. Morf, "The signal subspace approach for multiple wide-band emitter location," *IEEE Trans. Acoustic, Speech, and Sig. Process.*, vol. 31, no. 6, pp. 1502-1522, Dec. 1983.

[96] M. Wax, Tie-Jun Shan and T. Kailath, "Spatio-temporal spectral analysis by eigenstructure methods," *IEEE Trans. on Acoustics, Speech, and Signal Proces.,* vol. 32, no. 4, pp. 817-827, Aug. 1984.

[97] Y. Yoon, L. M. Kaplan, and J. H. McClellan, "TOPS: new DoA estimator for wideband signals," *IEEE Trans. Sig. Process.,* vol. 54, no. 6, Jun. 2006.

[98] H. Wang, and M. Kaveh, "Coherent signal-subspace processing for the detection and estimation of angle of multiple wide-band sources," *IEEE Trans. Acoustic, Speech, and Sig. Process.,* vol. 33, no. 4, Aug. 1985.

[99] H. Hung and M. Kaveh, "Focussing matrices for coherent signal- subspace processing," *IEEE Trans. Acoust., Speech, Signal Process.*, vol. 36, no. 8, pp. 1272-1281, Aug. 1988.

[100] M. A. Doron and A. J. Weiss, "On focusing matrices for wide-band array processing," *IEEE Trans. Sig. Process.,* vol. 40, no. 6, Jun. 1992.

[101] Fabrizio Sellone, "Robust auto-focusing wideband DOA estimation," *Signal Processing*, vol. 86, Iss. 1, pp. 17-37, 2006.

[102] B. Ottersten and T. Kailath, "Direction-of arrival estimation for wide-band signals using the ESPRIT Algorithm," *IEEE Trans. Acoust., Speech, Signal Process.,* vol. 38, no. 2, pp. 317-327, Feb. 1990.

[103] B. Friedlander and A. J. Weiss, "Direction finding for wide-band signals using an interpolated array," *IEEE Trans. Signal Process.,* vol. 41, no. 4, pp. 1618-1634, Apr. 1993.

[104] M. A. Doron, A. J. Weiss, and H. Messer, "Maximum-likelihood direction finding of wide-band sources," *IEEE Trans. Signal Process.,* vol. 41, pp. 411-414, Jan. 1993.

[105] E. D. Di Claudio and R. Parisi, "WAVES: weighted average of siganl subspaces for robust wideband direction finding," *IEEE Trans. Sig. Process.,* vol. 49, no. 10, Oct. 2001.

[106] Z. Tang, G. Blacquiere, and G. Leus, “Aliasing-free wideband beam- forming using sparse signal representation,” *IEEE Trans. Signal Process.,* vol. 59, no. 7, pp. 3464-3469, Jul. 2011.

[107] K. Yu, M. Yin, J. Luo, M. Bao, Y. H. Hu and Z. Wang, “A Direct wideband direction of arrival estimation under compressive sensing," *IEEE 10th International Conference on Mobile Ad-Hoc and Sensor Systems,* Hangzhou, pp. 603-608, 2013.

[108] S. Pejoski and V. Kafedjiski, “Sparse covariance fitting method for direction of arrival estimation of uncorrelated wideband signals,” *Teflor Journal*, vol. 6, no. 2, pp. 115-120, 2014.

[109] G. Zhao, Z. Liu, J. Lin, G. Shi and F. Shen, “Wideband DoA estimation based on sparse representation in 2-D frequency domain," *IEEE Sensors Journal*, vol. 15, no. 1, pp. 227-233, Jan. 2015.

[110] Y. Pan, N. Tai, N. Yaun. “Wideband DoA estimation via sparse bayesian learning over a Khatri-Rao dictionary,” *College of Electronic Science and Engineering , National University of Defence Technology Changsha, Hunan, 410073, China, 2015.*

[111] M. W. Long and M. S. Greco, “Sea and ground radar clutter modeling,” *IEEE Radar Conference*, Rome, 2008, pp. 1-1.

[112] B. Li and A. Petropulu, “MIMO radar and communication spectrum sharing with clutter mitigation,” *IEEE Radar Conference (RadarConf)*, Philadelphia, PA, 2016, pp. 1-6.

[113] U. Nielsen and J. Dall, “Direction-of-Arrival estimation for radar Ice sounding surface clutter suppression,” *IEEE Trans. on Geoscience and Remote Sensing*, vol. 53, no. 9, pp. 5170-5179, Sept. 2015.

[114] J. Liu, A. Song, F. Yang, X. Guo and J. Guan, “DOA estimation for closely spaced signals,” *IEEE International Conference on Signal Processing, Communication and Computing* (ICSPCC 2013), KunMing, 2013, pp. 1-4.

[115] G. Wang, T. Long, J. Xu, Y. Gao and Y. Jiang, “Research on DOA estimation for closely spaced strong and weak sources,” *IET International Radar Conference*, 2015, Hangzhou, 2015, pp. 1-6.

[116] G. Han, L. Wan, L. Shu and N. Feng, "Two novel DOA estimation approaches for real-time assistant calibration systems in future vehicle industria," *IEEE Syst. J.*, vol. 11, no. 3, pp. 1361-1372, Sept. 2017.

[117] W. Lei and B. Chen, "High-resolution DOA estimation for closely spaced correlated signals using unitary sparse Bayesian learning," Electronics Letters, vol. 51, no. 3, pp. 285-287, 5 2 2015.

[118] N. Anselmi, G. Gottardi, G. Oliveri, and A. Massa, “A total-variation sparseness-promoting method for the synthesis of contiguously clustered linear architectures” *IEEE Trans. Antennas Propag.*, vol. 67, no. 7, pp. 4589-4601, Jul. 2019.

[119] K. Mahata and M. M. Hyder, “Grid-less TV minimization for DOA estimation”, *Signal Processing*, vol. 132, pp. 155-164, 2017.

[120] P. Rocca, G. Oliveri, R. J. Mailloux, and A. Massa, “Unconventional phased array architectures and design methodologies - A review,” *IEEE Proc.*, vol. 104, no. 3, pp. 544-560, Mar. 2016.

[121] X. Lin, X. Zhang, and M. Zhou, “Nested planar array: configuration design, optimal array and DOA estimation,” *Int. J. Electron.*, vol. 106, no. 12, pp. 1885-1903, 2019.

[122] Z. Meng and W. Zhou, “Direction-of-arrival estimation in coprime array using the ESPRIT-based method,” *Sensors*, vol. 19, no. 3, pp. 1-14, Feb. 2019.

[123] F. Boccardi, R. W. Heath, A. Lozano, T. L. Marzetta, and P. Popovski, “Five disruptive technology directions for 5G,” *IEEE Commun. Mag.*, vol. 52, no. 2, pp.74-80, Feb. 2014.

[124] R. A. Mozingo, R. L. Haupt, and T. W. Miller, *Introduction to Adaptive Arrays.* Raleigh, NC: SciTech Publishing, 2011.

[125] Y. Huang and M. Barkat, “Near-field multiple source localization by passive sensor array”, *IEEE Trans. Antennas Propag.*, vol. 49, no. 7, pp. 968-975, Jul. 1991.

[126] K. Hu, S. P. Chepuri and G. Leus, “Near-field source localization: Sparse recovery techniques and grid matching," *2014 IEEE 8th Sensor Array and Multichannel Signal Processing Workshop (SAM)*, A Coruna, 2014, pp. 369-372, doi: 10.1109/SAM.2014.6882418.

[127] F. Frezza, *Properties of Plane Electromagnetic Waves. In: A Primer on Electromagnetic Fields.* Springer, Cham 2015. https://doi.org/10.1007/978-3-319-16574-5_2.